THE STRUCTURE AND STABILITY OF ROTATING RELATIVISTIC STARS

By

Nikolaos Stergioulas

A Dissertation Submitted in
Partial Fulfillment of the
Requirements for the degree of

Doctor of Philosophy

in

Physics

at

The University of Wisconsin-Milwaukee

May 1996

THE STRUCTURE AND STABILITY OF ROTATING RELATIVISTIC STARS

By

Nikolaos Stergioulas

A Dissertation Submitted in
Partial Fulfillment of the
Requirements for the degree of

Doctor of Philosophy

in

Physics

at

The University of Wisconsin-Milwaukee

May 1996

John L. Friedman Date

Graduate School Approval Date

THE STRUCTURE AND STABILITY OF ROTATING RELATIVISTIC STARS

By

Nikolaos Stergioulas

The University of Wisconsin-Milwaukee, 1996

Under the Supervision of Professor John L. Friedman

ABSTRACT

We conduct the first direct comparison of codes based on two different numerical methods for constructing rapidly rotating relativistic stars and find good agreement between corresponding models. For representative equations of state we construct 2-dimensional surfaces of equilibrium configurations in the 3-dimensional space of angular momentum, mass and central density. The maximum mass, baryon mass, angular momentum and angular velocity configurations are shown to be, generically, different, while for some equations of state all four maximum *stable* configurations coincide.

We investigate the upper limit on rotation of relativistic stars set by causality and compute the minimum period as a function of the maximum observed mass. No gravitationally bound star can rotate faster than $0.29(M_{max}/1.442\mathrm{M}_\odot)$ ms. The equation of state yielding the minimum period set by causality consists of a high-density region at the causal limit, which is matched to the known low density equation of state by an intermediate constant pressure region. This results in stars with stiff enough cores to sustain a certain mass and the softest possible exterior to allow for the fastest rotation.

Finally, we study nonaxisymmetric perturbations of rotating relativistic stars. The neutral (zero-frequency), fundamental $l = m$ modes are computed for several polytropic equations of state in the context of general relativity. These modes participate in setting the upper limit on the rotation of rapidly rotating neutron stars (created by the accretion-induced collapse of white dwarfs) by making the stars unstable to the emission of gravitational waves. We find that general relativity causes the nonaxisymmetric instability to set in at a significantly lower rotation rate than Newtonian theory suggests. Most strikingly, the m=2 bar mode can become unstable even for soft polytropes of index $N \leq 1.3$, while in Newtonian theory it becomes unstable only for stiff polytropes of index $N \leq 0.808$. Thus, the classical result for the critical adiabatic index $\Gamma_{\mathrm{crit}} = 2.237$ for the onset of the $m = 2$ instability in Newtonian theory, becomes $\Gamma_{\mathrm{crit}} \leq 1.77$ in the context of general relativity.

John L. Friedman Date

Preface

Chapter 1 originally appeared as Stergioulas, N. & Friedman, J. L. 1995, Astrophysical Journal, **444**, 306. Chapter 2 will be submitted to Physical Review D as Koranda, S., Stergioulas, N. & Friedman J. L. Chapter 3 will be submitted to Astrophysical Journal as Stergioulas, N. & Friedman, J. L. While at UWM, N. Stergioulas and S. Koranda were partially supported by NSF Grants PHY-9105935 and PHY-9507740. At Case Western Reserve University S. Koranda was partially supported by the DOE.

Acknowledgements

I am indebted to my advisor, John Friedman, for all his valuable help and advice. It was a pleasure working with him. For my education in physics and astrophysics, I would also like to thank Bruce Allen and Leonard Parker at UWM and Sotiris Persides, Nikolaos Spyrou, Dimitris Papadopoulos and Yiannis Seiradakis at the University of Thessaloniki. I appreciated very helpful conversations with Lee Lindblom, Jim Ipser, Yoshiharu Eriguchi and Ed Seidel. I thank Scott Koranda for his collaboration on part of this work.

Special thanks to Sukanta Bose, Paul Casper, Phil Carinhas and Gerry Graef. Many thanks to my parents and sisters for their support. Finally I thank, with all my heart, my wife Rena, for her invaluable support and persistent encouragement during the past five years.

Contents

List of Tables

List of Figures

Chapter 1

Comparing Models of Rapidly Rotating Stars Constructed by Two Numerical Methods

1.1 Introduction

Models of rapidly rotating relativistic stars have been constructed by a number of different groups, using a few somewhat different numerical methods (see Friedman [1] for a bibliography). Recent work has been based on the Butterworth & Ipser (hereafter BI) code [2] (Friedman *et al.* [3] (FIP), [4]; Lattimer *et al.* [5], on the Komatsu, Eriguchi & Hachisu (hereafter KEH) code (Komatsu *et al.* [6, 7]; Cook *et al.* [8, 9, 10]; Eriguchi *et al.* [11]; Nishida *et al.* [12, 13]; Hashimoto *et al.* [14]), and on a code using a finite element method (Neugebauer & Herlt [15]; Wu *et al.* [16]; Neugebauer & Herold [17]). No group has used more than one code and, as we will see, discrepancies in reported results reflect differences in versions of the same equation of state (EOS) and in the number of stellar models used to compute sequences, as well as numerical error intrinsic to the codes.[1] The present paper reports a direct comparison of models of rotating neutron stars constructed with two different codes. Models are computed using the FIP implementation of the BI method and corresponding models are constructed using a code written independently by Stergioulas, based on the

[1]After this paper was written, we received a copy of a preprint by Salgado *et al.* [18] reporting results from a new code based on a method different from those listed here.

Cook *et al.* implementation of the KEH method. We find good agreement between corresponding models. Sensitive quantities, such as the radius and quantities that depend on it, agree to better than 2%, despite the fact that the BI code used only 6 spokes (for one quadrant) and 60 radial grid points, because of limited computer speed at the time it was implemented. We used three EOSs, G (excessively soft), C and L (excessively stiff), to span a range of compressibility larger than that allowed by current knowledge of neutron-star matter. Error bars in the published numbers for maximum frequencies based on BI are dominated not by the code inaccuracy but by the number of models used to approximate a continuous sequence of stars. The BI code is faster per iteration and it converges more rapidly at low density, while KEH converges more rapidly at high density; KEH also converges in regions where BI does not, allowing one to compute some models unstable against collapse that are inaccessible to the BI code.

Models based on two other EOSs, FP and A, were also computed to compare them with results given in Eriguchi *et al.* [11].A relatively large discrepancy recently reported [11] for models based on the Friedman-Pandharipande equation of state is found to arise from the use of two different versions of the equation of state.

Our implementation of the KEH method is used to construct the two-dimensional family of equilibrium models for EOSs C, L and FP. The surface of equilibria is ruled by sequences of constant baryon mass and angular momentum, from which one obtains the boundary of the region of configurations stable to axisymmetric perturbations. We find, for a given equation of state, that equilibrium models with maximum values of mass, baryon mass or angular momentum are (generically) either all unstable to collapse or are all stable. In the first case, the *stable* model with maximum angular velocity is also the model with maximum mass, baryon mass and angular momentum. In the second case, the stable models with maximum values of these quantities are all distinct.

Our KEH code has been automated to construct various sequences of neutron star models and is available as a public domain program. Documentation for its use and availability is included in Appendix A.

1.2 Outline of the Numerical Methods.

The BI and KEH methods are described in detail in Butterworth & Ipser [2] and in Komatsu *et al.* [6] and Cook *et al.* [8], but an outline of their similarities and differences may be helpful (for a review of stellar structure prior to 1992, see Friedman & Ipser [19]). Following Bardeen & Wagoner [20], both methods use the same chart, describing the geometry of a stationary, axisymmetric rotating star by a metric of the form

$$ds^2 = -e^{2\nu}\, dt^2 + e^{2\psi}(d\phi - \omega dt)^2 + e^{2\alpha}(dr^2 + r^2 d\theta^2), \qquad (1)$$

where ν, ψ, α and ω are *metric potentials* independent of t and ϕ (∂_t and ∂_ϕ are Killing vectors) and we have set the velocity of light $c = 1$. Each method solves, equation-by-equation, the same set of four field equations and the integrated equation of hydrostatic equilibrium.

Although the gauge and the set of equations used are identical, the iterative procedure differs in two ways. To go from the kth to the (k+1)st approximation to a star, both methods solve one equation at a time for one potential at a time. In BI this is done to reduce the matrix one inverts to a manageable size. (With present computers, handling one potential at a time is less essential, but it may still be the most efficient method). KEH is designed for a one-potential approach and does not seem to allow a variant in which one solves simultaneously for the set of perturbed potentials. The BI iteration differs from a Newton-Raphson iteration only in this truncation. Komatsu *et al.* [6] observe that one can write the exact second-derivative terms as flat-space derivative operators acting on redefined potentials. This allows them to invert the (truncated) linearized operators by using explicit flat-space Green functions. One can view their iteration as departing from Newton-Raphson by omitting the linearized part of the operator that is not flat. This relation between the KEH method and Newton Raphson can be seen as follows: First, for simplicity, consider a single nonlinear equation for a single field ϕ,

$$L\phi = S(\phi), \qquad (2)$$

where L is a linear operator and S is nonlinear. Given ϕ_k, one obtains $\phi_{k+1} = \phi_k + \delta\phi$ via Newton-Raphson by writing

$$L\delta\phi - S'(\phi_k)\delta\phi = -L\phi_k + S(\phi_k). \tag{3}$$

This is identical to solving

$$L\phi_{k+1} - S'(\phi_k)\delta\phi = S(\phi_k). \tag{4}$$

where $S' = \delta S/\delta\phi$. In the KEH method, one solves the equation,

$$L\phi_{k+1} = S(\phi_k), \tag{5}$$

which can be regarded as the result of replacing the linearized operator $L - S'(\phi_k)$ occurring in the Newton-Raphson scheme by the truncated version L. [2]

For each of the three metric potentials that satisfy an elliptic equation, the KEH iteration conforms to the above description. In particular, consider Eq. (4) of KEH, for the redefined potential $f \equiv \rho e^{\gamma/2}$, where $e^\gamma = e^{\psi+2\nu}/(r\sin\theta)$ and $e^\rho = r\sin\theta e^{-\psi}$. If one were to follow BI, one would obtain the $(k+1)st$ value of the potential from the kth value of f and from the set Q_k of other potentials by solving

$$\nabla^2\delta f - \frac{\delta S_\rho}{\delta f}(f_k, Q_k)\delta f = -\nabla^2 f_k + S_\rho(f_k, Q_k), \tag{6}$$

to find

$$f_{k+1} = f_k + \delta f. \tag{7}$$

If one omits the term $\frac{\delta S_\rho}{\delta f}(f_k, Q_k)\delta f$, the resulting equation

$$\nabla^2\delta f = -\nabla^2 f_k + S_\rho(f_k, Q_k), \tag{8}$$

is identical to KEH,

$$\nabla^2 f_{k+1} = S_\rho(f_k, Q_k). \tag{9}$$

The other elliptic equations for the potentials are handled by KEH in essentially the same way.

[2]Our discussion clarifies the relation between KEH and Newton-Raphson; but the KEH iteration converges to a solution not because of that relation, but because Eq. (5) is an example of the method of successive substitution (see, e.g., Nakamura [21]). That is, when ϕ_k given by (5) converges, it converges to an exact solution, because Eq. (2) is exact.

The second key difference in the methods is in the quantities held fixed at each iteration: BI fix the polar redshift and angular velocity, while KEH fix the ratio r_p/r_e of values of the coordinate r at the pole and equator and the central energy density. In our implementation of KEH, the first order derivatives are approximated by a standard three-point formula. For the second order derivative, however, we found that, if one uses a standard three-point formula (as in Eriguchi *et al.* [11]) the metric potential α oscillates in most of the interior of the star along a radial spoke. We overcame the problem by using twice the grid spacing to evaluate the second order derivatives, which resulted in all metric potentials being smooth functions of radius and angle. If one does not follow the above procedure to assure the smoothness of the potentials, the errors introduced in the physical quantities can range from $\sim 0.5\%$ in the mass and radius to $\sim 2\%$ in other quantities, such as the angular velocity, angular momentum and redshifts for maximum mass models. The original KEH code (Komatsu *et al.* [6]) was subject to this error (Eriguchi [22]), which seems to arise because of the choice of angular coordinate ($\mu \equiv \cos\theta$). A more detailed explanation will be given in Eriguchi *et al.* [23].

1.3 Internal Checks and the Nonrotating Limit of the KEH Code

The accuracy of the physical quantities in a computed model depends on the grid-size and the domain of integration. BI and Eriguchi *et al.* [11] integrate over a spherical region of radius equal to about twice the equatorial radius of the star. We integrate over all space using the coordinate transformation introduced by Cook *et al.* [9]. The size of the grid that we use is 129×65 (radial $\times$ angular), which is similar to the one used by Cook *et al.* [9, 10] and Eriguchi *et al.* [11]. Doubling the number of grid-points in both directions did not change any physical quantity by more than 0.1 %.

Our code was checked in the nonrotating limit, by constructing sequences of spherical models and comparing them to models published in Arnett & Bowers [24]. Along a sequence of nonrotating models, the maximum differences between the two codes in the mass and radius are $\lesssim 0.3\%$ and become consistently smaller as one increases the number of grid points.

1.4 Comparison of Rotating Neutron Star Models.

The two codes were first compared for slowly rotating models. A typical model is shown in Table 1. The quantities compared are the central energy density ϵ_c, gravitational mass M, equatorial circumferential radius R, angular velocity Ω, angular momentum J, injection energy β, ratio of rotational kinetic energy T to gravitational binding W and the four metric potentials ν_c, B_c, α_c and ω_c evaluated at the center of the star. The redefined potential B is defined through

$$e^{\psi} = Br \sin\theta e^{-\nu}. \tag{10}$$

The agreement in the mass and angular velocity is $\sim 0.2\%$ while the metric potentials agree to within 0.01% to 0.4%. The two radii differ by 1.4%. Next, we compare rapidly rotating models, which are near the maximum mass (reported as the maximum mass models in FIP), for EOS C, L and G (Table 1). Here the agreement ranged from 0.1% to 0.6% for the masses and from 0.3% to 1.2% for the radii. The angular velocities agreed to $\sim 0.2\%$ and most other quantities to $\lesssim 0.5\%$, except for some quantities for EOS G and L which differed by a few per cent. Fig. 1 compares results of the BI and KEH codes for the metric potential ω as a function of coordinate radius in the equatorial plane for the two rapidly rotating, EOS C models in Table 1. The two curves almost coincide and the agreement in the other three metric potentials for the above two models was slightly better. FIP estimate the accuracy of their results to be $\sim 1\%$ in the mass, metric coefficients, density and pressure distributions while the accuracy of the radius and quantities that depend on it is estimated at $\sim 5\%$. The differences in the above comparisons were somewhat better than this, implying an accuracy in finding the location of the surface that is somewhat (but not dramatically) better than the grid spacing. The vast increase in computer speed since the BI code was written allows a much finer grid and correspondingly greater accuracy in surface finding.

To compare the convergence for the two codes, we used as input for each code a fixed initial model and required the code to converge to the same final model, for which the initial model served as an inaccurate guess. The number of iterations required increases considerably for both codes as one approaches the maximum mass. BI exploits the fact that stellar structure is dominated by the lowest-order multipoles $P_l(\cos\theta)$ and uses a grid of size 60×6, with 6 radial spokes in a quadrant. This means one truncates the multipole expansion above $l = 12$. Fig. 2 compares the number of iterations needed to obtain a given accuracy in $|\delta g^{tt}/g^{tt}|$ for a rapidly rotating, high density model (δg^{tt} here means the difference in g^{tt} from one iteration to another). For the same accuracy, KEH needs a larger grid and a longer time per iteration: On the DEC Alpha we used, BI required 0.2 s/iteration, compared to 0.7 s/iteration for KEH, for grids yielding comparable error. Because roughly the same number of iterations were required for the same accuracy for low-density models, BI was more than three times as fast, but KEH came into its own for the highest density models, near and above maximum mass. KEH requires fewer iterations near the maximum mass model and it has additional advantages: (i) except for the lowest density models, BI typically requires one to multiply the inhomogeneous terms by a parameter $C < 1$ to obtain a convergent iteration and time is spent adjusting C as central density or angular velocity increase along a sequence (KEH did not require any such parameter in order to converge, except for very high density, unstable models constructed with EOS FP). (ii) Although BI successfully computes the full range of equilibria for realistic EOSs, KEH is more robust, allowing one to compute a wider range of models unstable to collapse. (iii) The code can be easily written to allow the user to specify the grid size.

We compared models computed with the KEH code to corresponding models in Cook *et al.* [9, 10] and in Eriguchi *et al.* [11] and found them in good agreement (maximum 1-2 % differences in physical quantities).[3] Eriguchi *et al.* [11] compared their results to Friedman *et al.* [4] and found similarly good agreement except for EOS FP (Friedman & Pandharipande [26]). For this EOS, the two Ω_K vs. M curves substantially disagreed (where Ω_K is the angular velocity at the *mass-shed* or *Kepler* limit); there was a 5 % discrepancy in the maximum angular velocity and a larger (25 %) difference in the central energy densities of the maximum-mass configurations.

[3]This agreement is equivalent to that just reported by Salgado *et al.* [18, 25] with whom our KEH code also agrees to within 1-2%.

This seemed worrisome, but the difference between the computed models turns out to be almost entirely due to a difference in the version of the EOS used. Using our KEH code, we recomputed the Ω_K vs. M curve for EOS FP and found it to be close to the corresponding curve in Friedman *et al.* [4], (Fig. 3). A computation of the same curve using the version communicated to us by Eriguchi of the FP EOS gave a curve that is similarly close to that of Eriguchi *et al.* [11]. For the version of FP used in FIP, models with the same central density based on the KEH and BI codes agree in all quantities to within 3% (which includes the error in determining Ω_K). There is a larger difference in the value of ϵ_c at the maximum mass model, because the error in determining Ω_K is multiplied by a large value of $\partial\epsilon_c/\partial\Omega_K$ (where the derivative is evaluated along a sequence of models at the mass-shed limit).

The frequency Ω_s of a satellite in circular orbit at the star's equator decreases monotonically as Ω (and hence the radius of the star) increases, with $|d\Omega_s/d\Omega|_{\epsilon_c}$ and $|d\Omega_s/d\Omega|_{M_0}$ apparently diverging at $\Omega = \Omega_s \equiv \Omega_K$ (Fig. 4). Our code exploits the steep slope in order to compute Ω_K. By truncating the energy density at the equator, we are able to compute unphysical models that are above the mass-shed limit ($\Omega > \Omega_K$). By iterating between models above and below the mass-shed limit, we compute Ω_K with high accuracy. Because the apparent divergence in $|d\Omega_s/d\Omega|$ arises from a similar divergence in $|dR/d\Omega|$ (Fig. 5) one needs that high accuracy to determine R and quantities which depend on it.

1.5 Surfaces of Equilibria

The equilibrium models for a given EOS comprise a 2-dimensional surface. Our KEH code is automated to construct sequences of constant angular momentum and sequences of constant baryon mass, terminating at $\Omega = \Omega_K$. For a given EOS, we first construct the nonrotating sequence and the $\Omega = \Omega_K$ sequence. The code then uses this information to construct a specified number of constant J and constant M_0 (*baryon mass*) sequences, ruling the 2-dimensional surface of equilibria. The corresponding surfaces for EOSs C, L and FP are shown in Figs. 6 to 8. These equations of state are substantially different, leading to stars whose maximum values of J differ by more than a factor of two. But their ruled surfaces of equilibria are strikingly similar and the similarity seen in the figures persists for the other equations of state we have examined. On each surface, the ridge of maximum mass at fixed J (or minimum mass at fixed baryon mass M_0) marks the onset of axisymmetric instability (instability to collapse) (Friedman, Ipser & Sorkin [27], Cook *et al.* [8]). Stars stable against collapse lie on the low-density side of the dashed line on each surface. The surfaces fold over at the ridge, and the figures display a sharp contrast between an apparent cusp at the maximum mass configuration in the $J-M$ plane and the smooth unprojected boundary of the surface itself.

FIP noted that among all stable models, the model with maximum mass appeared also to have the maximum Ω, J and M_0 and this apparent coincidence can be seen in Figs. 6 to 8. As Cook *et al.* [8, 9, 10] have found, there is often a slight difference between the models of maximum M and Ω and a check of their claim for EOSs L and FP is shown in Figs. 9 and 10, which depict the region very near the maximum mass model. In addition, we find that models with maximum values of J and M_0 can also fail to coincide exactly with the maximum Ω model and this can be seen from the following argument: The models with maximum Ω and maximum M among all equilibria do not coincide. Thus either $\epsilon_c(\Omega_{\rm max}) < \epsilon_c(M_{\rm max})$ or $\epsilon_c(\Omega_{\rm max}) > \epsilon_c(M_{\rm max})$. In the first case, stable models with maximum M, Ω, J and M_0 coincide. In the second case, $(\partial M/\partial \epsilon_c)_J > 0$ for any $\epsilon_c < \epsilon_c(\Omega_{\rm max})$ and $J(M_{\rm max}) > J(\Omega_{\rm max})$. Furthermore, $\partial M/\partial \epsilon_c = 0$ at the maximum mass model. Hence, there exists $\epsilon_c < \epsilon_c(M_{\rm max})$ with $J > J(M_{\rm max})$. A similar argument, using $(\partial M/\partial \epsilon_c)_{M_0}$, yields $\epsilon_c(M_{0{\rm max}}) \neq \epsilon_c(M_{\rm max})$, (see Figs. 9 and 10).

Depending on the central density of the fastest rotating stable model we can distinguish two classes of equations of state: if the fastest rotating stable model is at a lower density than the maximum mass equilibrium model, the *equilibrium* models with maximum M, M_0 and J are all unstable (e.g. EOS FP, Fig. 10); otherwise they are all stable (e.g. EOS L, Fig. 9). We note that in the first case, the fastest rotating *stable* model is also the configuration with maximum M, M_0 and J, while in both cases the four different *equilibrium* models are all distinct. Even when the coincidence of stable models is not precise, the models with maximum M, Ω, J and M_0 are generally very close in central density. As a result, they *appear* to coincide with the sharp edge in the M-J plots (Figs. 6 to 7). There is , however, a class of equations of state, where the models with maximum Ω, M, M_0 and J can have substantially different central energy densities. These are the equations of state with a phase transition near the central energy of the maximum mass model and an example is EOS M in Cook *et al.* [9].

In chapter 2, our code for computing rapidly rotating relativistic stars is used to investigate the upper limit on their rotation set by causality.

Table 1: Comparison of rotating neutron star models obtained by the KEH (first line) and BI (second line) codes

$\epsilon_c\times$ 10^{15}gr $/\mathrm{cm}^3$	$M/$ $M_\odot$	$R/$ km	Ω $\times 10^4$ s^{-1}	$cJ/$ $GM_\odot^2$	β	$T/$ $\lvert W\rvert$	ν_c	B_c	α_c	ω_c $\times 10^4$ s^{-1}
EOS C (slow model)										
0.984	1.32	12.1	0.150	2.19	0.676	0.004	-0.424	0.949	0.371	0.639
0.984	1.32	12.3	0.150	2.17	0.676	0.004	-0.423	0.949	0.371	0.637
EOS C										
2.64	2.17	13.3	1.072	2.99	0.350	0.1091	-1.134	0.752	0.848	0.838
2.64	2.16	13.2	1.071	2.97	0.352	0.1095	-1.131	0.753	0.847	0.835
EOS G										
5.48	1.55	8.63	1.521	1.45	0.339	0.098	-1.23	0.711	0.891	1.223
5.48	1.55	8.60	1.524	1.49	0.340	0.101	-1.22	0.718	0.890	1.220
EOS L										
1.10	3.20	17.2	0.762	6.81	0.326	0.122	-1.09	0.769	0.830	0.588
1.11	3.18	17.3	0.764	6.88	0.340	0.122	-1.07	0.786	0.828	0.582

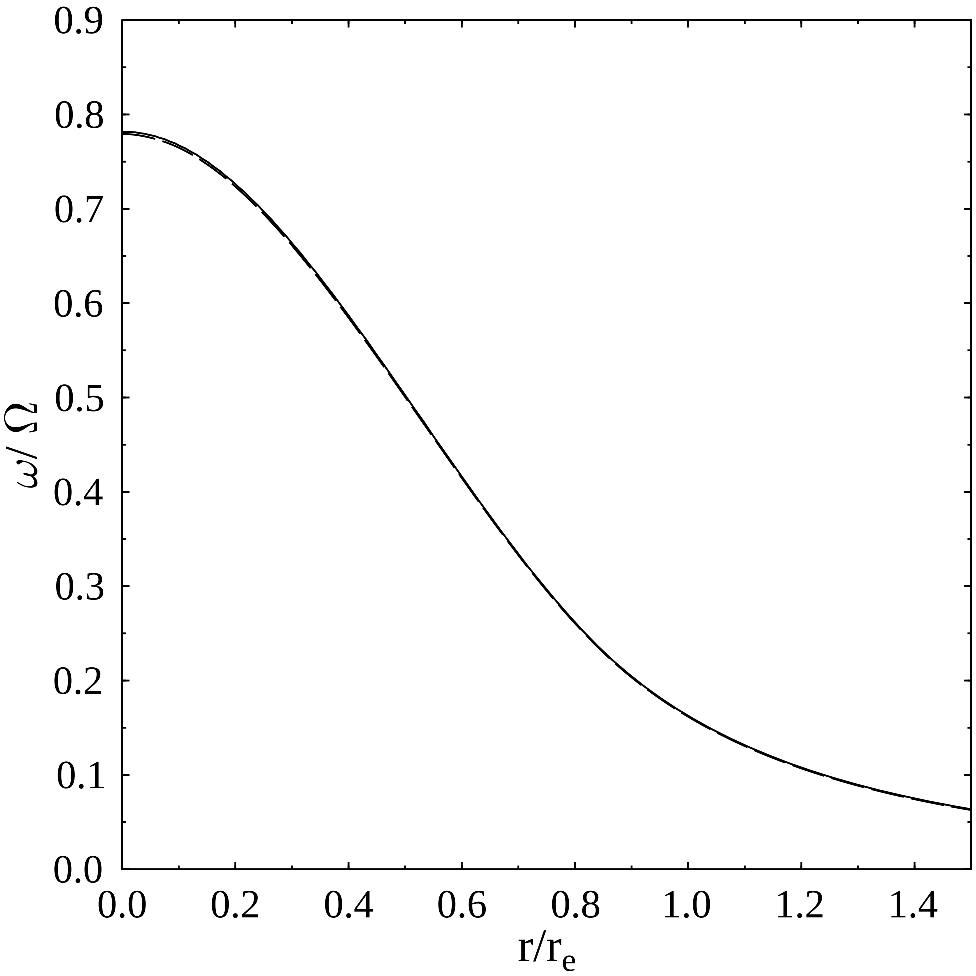

Figure 1: Comparison of the metric potential ω at the equatorial plane for the two rapidly rotating, EOS C models shown in Table 1. The horizontal axis shows the coordinate radius r, while the values of Ω and r_e of the model constructed with the KEH code were used to scale the two axes. The two curves almost coincide.

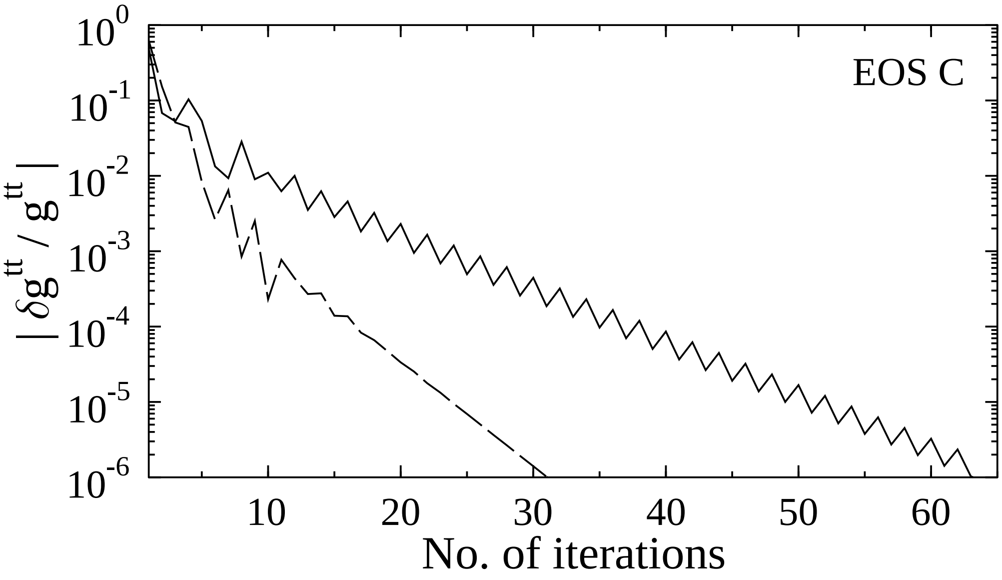

Figure 2: The fractional change in g^{tt} is plotted against the number of iterations for a high density, EOS C model. The solid line was obtained with the BI code and the dashed line with the KEH code.

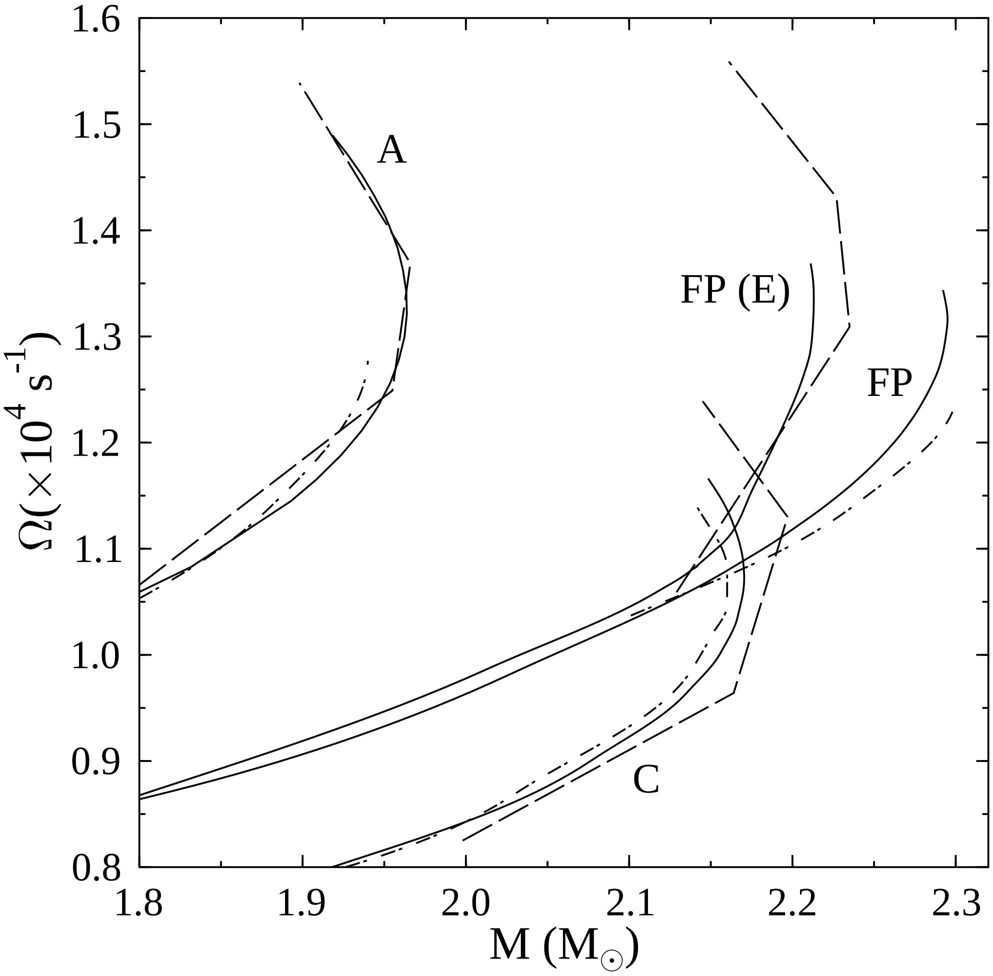

Figure 3: Angular velocity vs. mass plot depicting sequences of models at the mass-shed limit for EOSs C, A and FP. Solid lines are present results, long dashed lines are Eriguchi *et al.* [11] results and short dashed lines are FIP [3] results. FP (E) is the version of the FP EOS that Eriguchi *et al.* [11] used.

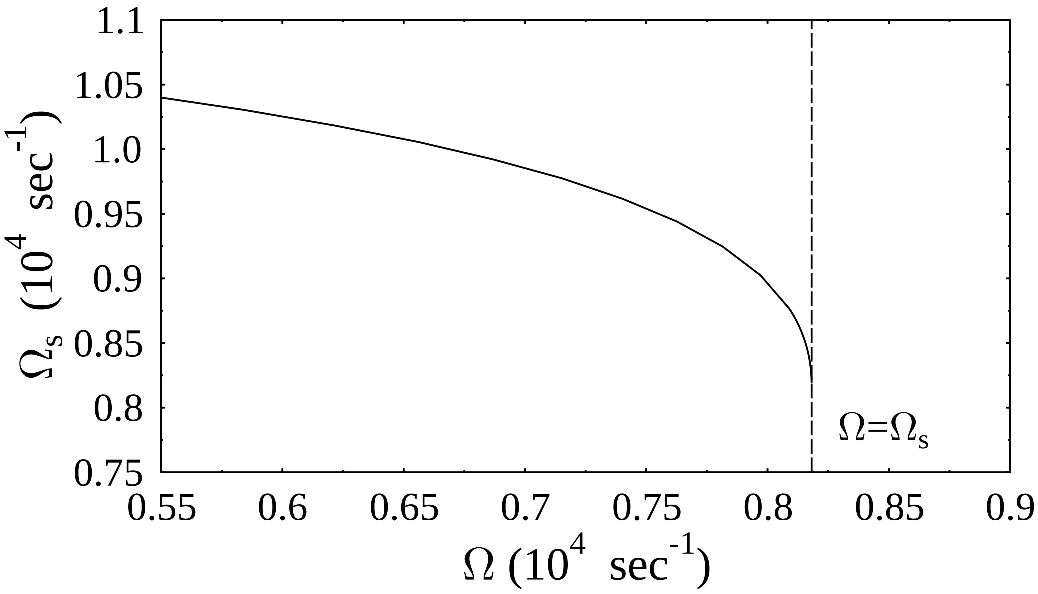

Figure 4: The frequency Ω_s of a satellite in circular orbit at the equator drops sharply as the star approaches the mass-shed limit. The above sequence of models was constructed with EOS L and with constant $\epsilon_c = 1.21 \times 10^{15}\mathrm{gr/cm}^3$.

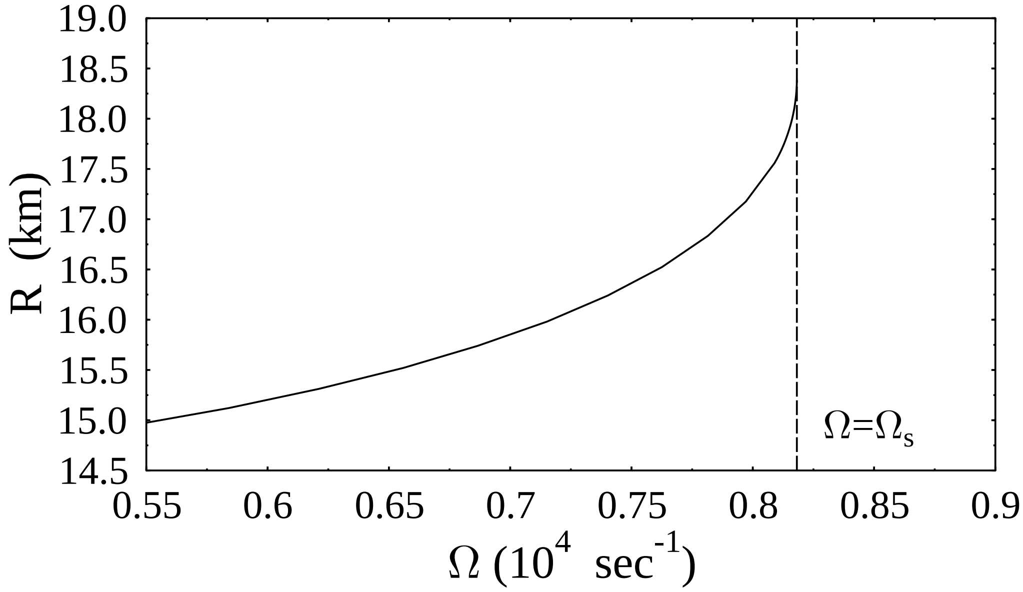

Figure 5: The radius R of a star increases sharply as the star approaches the mass-shed limit. The sequence of models is that of Fig. 4 .

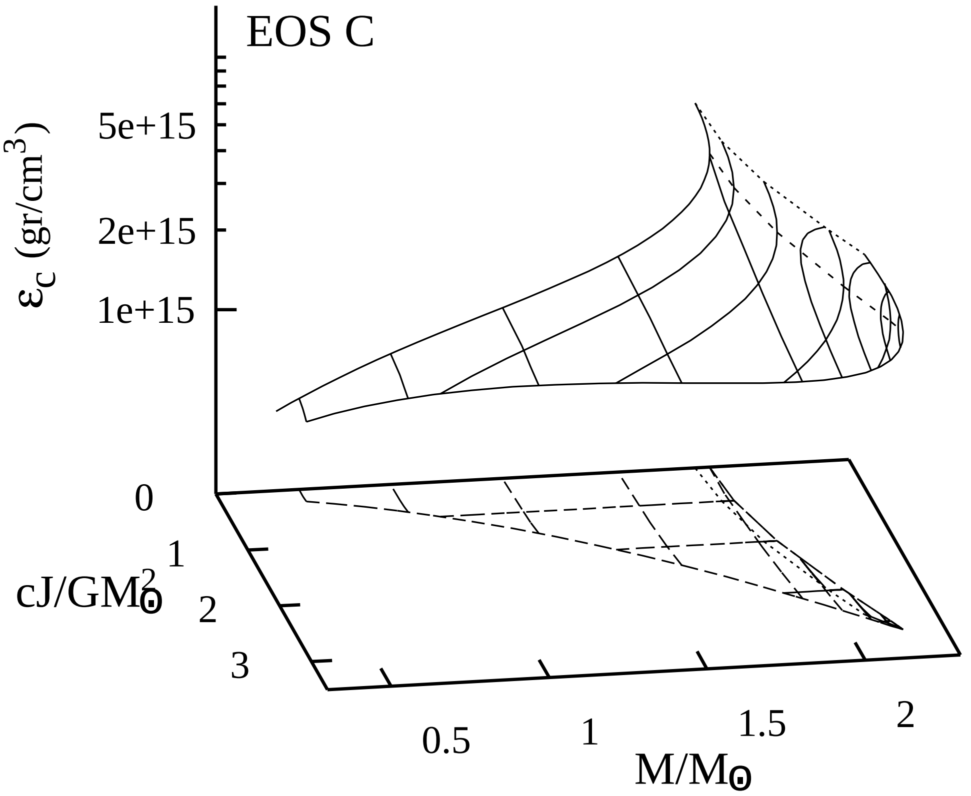

Figure 6: The 2-D surface of equilibrium models is embedded in the J-M-ϵ_c space. The surface is bounded by the spherical ($J = 0$) and Keplerian ($\Omega = \Omega_K$) limits and formed by constant J and constant M_0 sequences (solid lines). Also shown are the axisymmetric instability sequence (short-dashed line), the projections on the J-M plane (long-dashed lines) and the overlapping of the surface in the J-M plane (dotted lines).

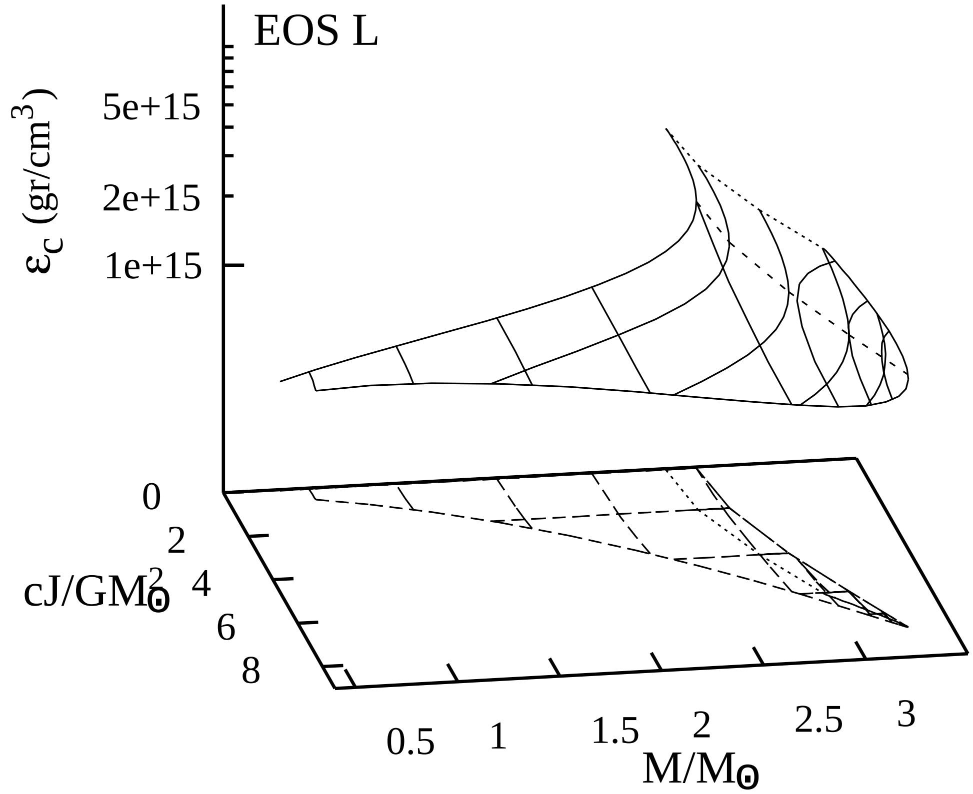

Figure 7: Surface of equilibrium models for EOS L.

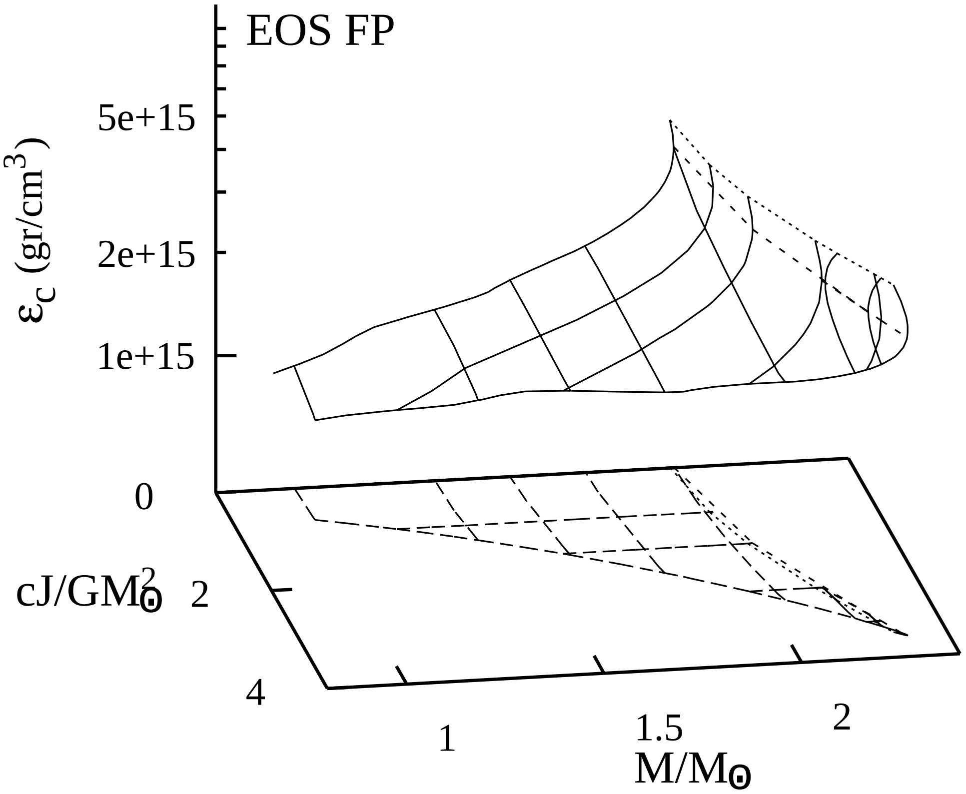

Figure 8: Surface of equilibrium models for EOS FP.

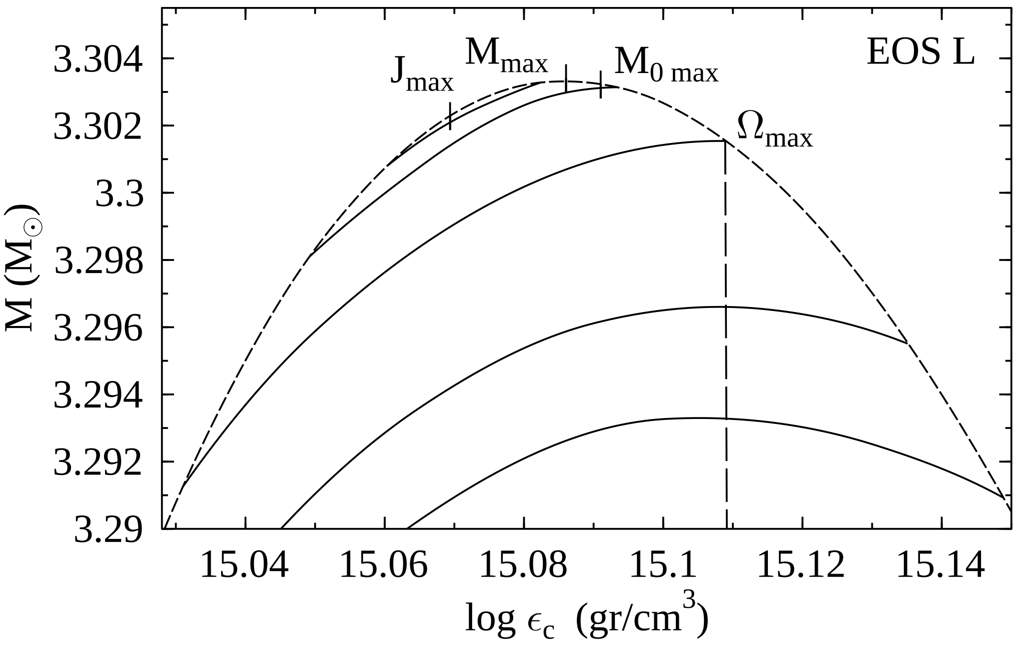

Figure 9: Detail near $M_{\max}$ of the mass vs. central density plot for EOS L. Four different stable models are associated with maximum values of M, M_0, J and Ω. Solid lines are constant J sequences, the short-dashed line is the mass-shed limit and the long-dashed line is the axisymmetric instability sequence. A 257×129 grid was used for high accuracy.

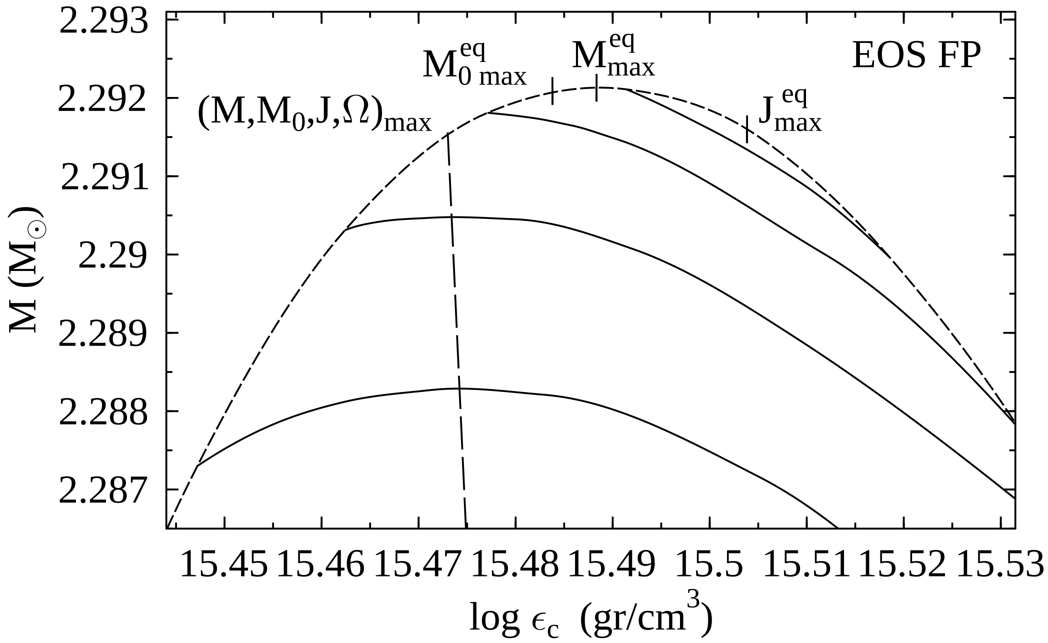

Figure 10: Same as Fig. 9, but for EOS FP. A single stable model has maximum values of M, M_0, J and Ω.

Chapter 2

The Causality-Set Upper Limit on the Rotation of Gravitationally Bound Stars

2.1 Introduction

The upper limit set by gravity on the rotation of neutron stars is sensitive to the equation of state above nuclear density, and the large present uncertainty in the equation of state implies a correspondingly large uncertainty in the maximum rotation. One can, however, find an upper limit on rotation that is independent of the equation of state (EOS). This limit is set by causality together with the requirement that the equation of state allows stars with masses as large as the largest observed neutron-star mass.

The first estimate of the causality-set limit on rotation is due to Glendenning [28]. He uses a flexible two-parameter, gamma-law ansatz for the EOS at high energy density; by varying the two parameters, he finds a class of EOSs which appear to minimize the period as a function of the maximum nonrotating mass M_{sph}^{max} allowed by the EOS. Our work improves upon his estimate in several ways. First, where Glendenning uses an approximate empirical formula to estimate the minimum period from a set of nonrotating models, we construct explicit models using an accurate code for rapidly rotating relativistic stars. Second, our numerical investigation singles out a simple analytic form for the equation of state that minimizes the period for a given maximum nonrotating mass. This limiting EOS has a natural physical interpretation, essentially providing the most centrally condensed star consistent with the requirement that the EOS support an object of mass M_{sph}^{max}. Specifically, we find that if $M_{\rm sph}^{\rm max} = 1.442$ $\rm M_\odot$ (which is currently the largest accurately measured mass of neutron stars [29]), then the minimum period allowed is 0.29 ms. The minimum period we obtain is about 10 % less than that previously estimated by Glendenning[28]. Finally, we find a nearly exact scaling giving the relation $P_{\rm min} \propto M_{\rm sph}^{\rm max}$. As we discuss, the scaling arises from the form of the limiting equation of state, and implies that the central energy densities, masses and radii of the maximum mass spherical (and maximum mass rotating) stars scale between different limiting EOS's .

The value of $P_{\rm min}$ is relatively insensitive to the EOS below nuclear density or to the density at which one matches the minimizing analytic EOS to the "known" low-density EOS. This insensitivity is in contrast to the dependence on matching density (see e.g. Hartle & Sabbadini [30]) of the corresponding limit that causality sets on the maximum mass of neutron stars, first computed (for a particular choice of matching density) by Rhoades and Ruffini [31]. The causality-set upper limit on the mass of rotating neutron stars was first computed by Friedman and Ipser [32]. It has not, however, been recomputed since the recent improvement in the accuracy of codes for rotating stars, and we do so here, using the FPS EOS [33] at low density, and finding $M_{\rm max} = 6.1 {\rm M}_\odot (\epsilon_m/2 \times 10^{14} {\rm gr/cm}^3)^{-1/2}$, where ϵ_m is the matching density.

2.2 Constraints on the Equation of State

For number densities $n \lesssim 0.1$ fm^{-3} (slightly less than nuclear saturation density) the FPS EOS [33] accurately represents ordinary matter. Above this density, however, a large number of proposed EOSs are compatible with current observations, but the minimum period (and maximum mass) predicted by each EOS can vary significantly. Based on the proposed EOSs, one can not firmly determine the minimum period and maximum mass of compact stars. To set an upper limit on the rotation of relativistic stars, independent of the high density equation of state, one must rely on a set of minimal constraints which are based on well established physical principles. Similarly to Glendenning [28], we impose the following minimal set of constraints on the equation of state:

(1) $\frac{dp}{d\epsilon} \leq 1$.

This assumption, that the phase velocity of sound is less than the speed of light, is required in order that a fluid description of matter is causal. Relativistic fluids are governed by hyperbolic equations with characteristics along the cone corresponding to $v_{\rm sound} = \sqrt{dp/d\epsilon}$ and their initial value formulation violates causality if $v_{\rm sound} > 1$ (see Geroch & Lindblom [34]).

(2) *The high density EOS matches to the known low density form.*

The FPS EOS is reliable up to number densities of about $n = 0.1$ fm^{-3} [35], which we adopt as a conservative value for the matching density n_m. The computed minimum period is relatively insensitive to this choice.

In addition, we only consider cold stars, which can be modeled as being at zero temperature. Then, the pressure is a function of energy density only, $p = p(\epsilon)$. The rotation is assumed to be uniform, since cold relativistic stars have a solid crust and rotate with virtually constant angular velocity.

2.3 Equation of State Yielding the Upper Limit on Rotation

A uniformly rotating, gravitationally bound star rotates with a period greater than or equal to its Kepler period, the period of a free particle in circular orbit at the star's equator. A soft EOS yields stellar models with denser central cores, larger binding energy, and thus smaller Kepler periods than models built from a stiff EOS. On the other hand, soft equations of state cannot support massive stars. This argument suggests that stellar models with the shortest periods of rotation arise from equations of state that are stiff at high density - allowing stiff cores to support the star against collapse; and soft at low density, allowing models as massive as the most massive observed neutron stars.

This expectation is consistent with the results of our numerical investigation, which strongly suggests a simple form for the EOS that yields a minimum period of rotation subject to the constraints listed in section 2.2. Above a density ϵ_C it is maximally stiff, with causality-limited value $dp/d\epsilon = 1$. Between the matching density to the low density EOS ϵ_m and ϵ_C the EOS is maximally soft, with $dp/d\epsilon = 0$. Explicitly,

$$p(\epsilon) = \begin{cases} p_{\mathrm{FPS}}(\epsilon) & \epsilon \leq \epsilon_m, \\ p_m & \epsilon_m \leq \epsilon \leq \epsilon_C, \\ p_m + \epsilon - \epsilon_C & \epsilon \geq \epsilon_C. \end{cases} \tag{11}$$

This 3-regime EOS is depicted in Fig. 11. The maximally soft, constant-pressure, regime would correspond to a first-order phase transition for a system described by a 1-parameter EOS of the form (11).

For a fixed low density EOS and matching energy density ϵ_m, the causal limit energy density ϵ_C parametrizes the class of minimum period EOSs. This single parameter ϵ_C is determined by the desired mass M_{sph}^{max} of the allowed maximum mass spherical star. Note that there also exists a one to one correspondence between ϵ_C and other characteristics of the minimum period EOS, such as the maximum mass for rotating stars. Figure 12 shows the minimum period EOS (11) for $\epsilon_C = 2.157 \times 10^{15}\mathrm{g/cm}^3$, corresponding to $M_{sph}^{max} = 1.442\ \mathrm{M}_\odot$. The low density EOS is the FPS EOS, and the matching number density is $n_m = 0.1\ \mathrm{fm}^{-3}$. The central energy density of the minimum period star is $5.274 \times 10^{15}\mathrm{g/cm}^3$. The numerical work leading to the form (11) is outlined in sections 2.4 and 2.5.

Fig. 13 shows the minimum period P_{min} of gravitationally bound stars as a function of the maximum allowed mass of nonrotating stars M_{sph}^{max}. For $M_{sph}^{max} = 1.442\,\mathrm{M}_\odot$ the minimum period is 0.29 ms. Note that the curve in Fig. 13 is almost linear. This has the following explanation. The matching number density $n_m = 0.1\ \mathrm{fm}^{-3}$ is low enough that the causal limit region of the EOS dominates the bulk properties of the star. As noted in section 2.6, if one neglects the low density region completely (by setting $n_m = 0$), the minimum period is lowered by less than 3 % for any M_{sph}^{max} (compared to $n_m = 0.1\ \mathrm{fm}^{-3}$). Thus, a minimum period star with a low matching density mimics a star *entirely* at the causal limit and having a nonzero surface energy density equal to ϵ_C. Such stars observe a scaling with respect to the surface energy density. Because the minimum period stars so closely mimic these nonzero surface energy density stars, the P_{min} vs. M_{sph}^{max} curve is nearly linear. Likewise, for the stars with a causal limit interior and nonzero surface energy density the following relations hold between EOS's of different surface energy density

$$\begin{aligned} R_{sph}^{max} &\propto M_{sph}^{max}, & (12)\\ \epsilon_{sph}^{max} &\propto \frac{1}{(M_{sph}^{max})^2}, & (13)\\ M_{rot}^{max} &\propto M_{sph}^{max}, & (14)\\ R_{rot}^{max} &\propto R_{sph}^{max}, & (15)\\ \epsilon_{rot}^{max} &\propto \epsilon_{sph}^{max}, & (16) \end{aligned}$$

where R is the equatorial circumferential radius. The exact scaling for the causal EOS follows from the fact that, in gravitational units ($G = c = 1$), the family of maximally rotating equilibria are characterized by one dimensionful parameter. All quantities scale in accordance with their dimensions: $[M] = [R]$, $[\epsilon] = [M^{-2}]$, etc. For the minimum period EOSs, the stars are not entirely at the causal limit but have a crust of normal matter. Thus the above relations hold approximately. In particular, the relation between P_{min} and M_{sph}^{max} has the form

$$\frac{P_{\rm min}}{\rm ms} = 0.295 + 0.203 \left(\frac{M_{sph}^{max}}{\rm M_\odot} - 1.442\right), \tag{17}$$

(for $n_m = 0.1$ fm^{-3}) and is linear to an accuracy of better than 0.5 %. This formula allows one to quickly calculate, without intensive numerical computations, the minimum period set by causality, if and when new observations revise the current $M_{sph}^{max} = 1.442{\rm M}_\odot$ limit. Taking into account the discussion in section 2.6, (17) yields the causality-set minimum period of gravitationally bound stars to an accuracy of better than 2 %, for the current uncertainty in the high density equation of state.

2.4 Ansatz for Searching the Space of Equations of State

To search the restricted space of EOSs which meet the constraints outlined in section 2.2, and to determine which class of EOSs yield the minimum period stars, we follow

Glendenning [28] and adopt a simple ansatz for the EOS. For low number density n, the energy density ϵ and pressure p are

$$\begin{aligned} \epsilon(n) &= \epsilon_{\mathrm{FPS}}, & (18) \\ p(n) &= p_{\mathrm{FPS}}, & (19) \end{aligned}$$

where ϵ_{FPS} and p_{FPS} correspond to the FPS EOS. Above some number density n_m, where the FPS EOS is suspect, the energy density and pressure are

$$\begin{aligned} \epsilon(n) &= p_m \left\{ \frac{\kappa}{\gamma - 1} \left[\left(\frac{n}{n_m} \right)^\gamma - \frac{n}{n_m} \right] + \frac{n}{n_m} \frac{\epsilon_m}{p_m} + \left(1 - \frac{n}{n_m} \right) (\kappa - 1) \right\}, & (20) \\ p(n) &= p_m \left\{ \kappa \left[\left(\frac{n}{n_m} \right)^\gamma \right] + 1 \right\}, & (21) \end{aligned}$$

where ϵ_m and p_m are the energy density and pressure at the matching number density n_m, which is typically 0.1 fm^{-3}. The two dimensionless parameters κ and γ parametrize the restricted EOS space. The constraints listed in section 2.2 require

$$\begin{aligned} \gamma > &\quad 1, & (22) \\ \kappa > &\quad 0, & (23) \\ \kappa\gamma \leq &\quad \tfrac{\epsilon_m}{p_m} + 1. & (24) \end{aligned}$$

Given κ and γ, we use the parametrized form (20) and (21) for densities greater than the matching density n_m, but only if the EOS remains causal. If above some density n_C the equation of state reaches the causal limit, so that $\frac{dp}{d\epsilon} \geq 1$, then for $n > n_C$ the parametrized EOS is matched to an EOS which is always at the causal limit. In this instance the energy density and pressure above n_C are

$$\begin{aligned} \epsilon(n) &= \epsilon_C - p_C + p(n), & (25) \\ p(n) &= \frac{1}{2} \left\{ p_C - \epsilon_C + (p_C + \epsilon_C) \left(\frac{n}{n_C} \right)^2 \right\}, & (26) \end{aligned}$$

where ϵ_C and p_C are the energy density (20) and pressure (21) evaluated at n_C. Note that the parametrization of pressure as a function of number density is arbitrary, since (25) assures that $\frac{dp}{d\epsilon} = 1$. If κ and γ are chosen so that the EOS remains causal then the parametrized form is used for all densities $n \geq n_m$. Combining the different expressions for the different ranges of number density the EOS is

$$\epsilon(n) = \begin{cases} \epsilon_{\mathrm{FPS}}(n) & n \leq n_m, \\ p_m \left\{ \frac{\kappa}{\gamma-1} \left[\left(\frac{n}{n_m} \right)^{\gamma} - \frac{n}{n_m} \right] + \frac{n}{n_m} \frac{\epsilon_m}{p_m} + \left(1 - \frac{n}{n_m} \right) (\kappa - 1) \right\} & n_m \leq n \leq n_C, \\ \epsilon_C - p_C + p(n) & n \geq n_C, \end{cases} \tag{27}$$

$$p(n) = \begin{cases} p_{\mathrm{FPS}}(n) & n \leq n_m, \\ p_m \left\{ \kappa \left[\left(\frac{n}{n_m} \right)^{\gamma} \right] + 1 \right\} & n_m \leq n \leq n_C, \\ \frac{1}{2} \left\{ p_C - \epsilon_C + (p_C + \epsilon_C) \left(\frac{n}{n_C} \right)^2 \right\} & n \geq n_C, \end{cases} \tag{28}$$

where the $n \geq n_C$ case applies only if n_C exists and is finite. Note that the EOS is continuous, although its first derivative may be discontinuous at n_m. We do not include a separate expression for the possibility of a $p =$ constant, *one-component first-order phase transition region*, since this is attained in the limit as $\kappa \to 0$. One may search the restricted EOS space using (27) and (28) by varying the parameters κ and γ.

The two-parameter EOS (27) and (28) does not span the entire restricted EOS space. Still, as Figure 14 shows, it is quite flexible, and spans a representative subspace which includes both soft and stiff EOSs. This two-parameter family of EOSs proved sufficient to identify the class of EOSs yielding the minimum period stars.

2.5 Searching for the Minimum Period Star

We used a fully relativistic, numerical code to compute rapidly rotating models of compact stars and find the maximum mass model for a given EOS. Stergioulas [36] wrote the code following the Cook, Shapiro & Teukolsky [10] implementation of the Komatsu, Eriguchi & Hachisu method [7]. Koranda made improvements that substantially increased the code's execution speed.

Using the flexible ansatz (27) and (28), we have searched for the class of EOSs which yield the minimum period stars. As mentioned in the introduction, we are interested in the minimum period as a function of M_{sph}^{max}, the mass of the maximum mass nonrotating (spherical) star. We first used (27) and (28) to search for EOSs yielding particular values of M_{sph}^{max}. Figure 15 shows our results. Having determined the κ and γ parameters, and hence the EOSs which allow maximum mass spherical stars with mass M_{sph}^{max}, we then searched amongst those EOSs for the one which yielded the rotating star with the minimum period. By computing the maximum mass rotating model at different points along the constant M_{sph}^{max} lines of Figure 15, we searched for the absolute minimum period P_{min}. Figure 16 shows the results of our search for $M_{sph}^{max} = 1.442\ \mathrm{M}_{\odot}$. Each point along the curve defines an EOS which yields a maximum mass spherical star of mass $M_{sph}^{max} = 1.442\ \mathrm{M}_{\odot}$. As one moves along the curve towards smaller and smaller values of κ, *the minimum period allowed by the EOS continues to decrease and tends asymptotically to a minimum as* $\kappa \to 0$.

That the period tends only asymptotically to a minimum as $\kappa \to 0$ can be understood by considering the EOSs sampled as one moves along the curve in Figure 16. Figure 17 shows the EOSs sampled as one moves along the curve in the $\kappa\gamma$ plane. As one moves to small κ the EOS is essentially unchanged, approaching an EOS with constant pressure from p_m to p_C. This behavior is the same for all values of M_{sph}^{max}.

2.6 Accuracy Check and Variation of Different Parameters

The numerical code used to construct rapidly rotating, fully relativistic compact star models was checked for accuracy in an extensive comparison to other codes [23]. The agreement of the codes for physical quantities of specific models was 0.1 % to 0.01 % or better, depending on the stiffness of the EOS. Determining the maximum mass model for a given EOS requires computing a large number of models until one computes a model within some tolerance of the true maximum mass and Kepler limit. Since the mass vs. central energy density curve is approximately flat near the maximum mass, we used a finely spaced grid and small tolerances (hence a large number of computed models) when constructing individual models to determine the maximum mass model for a given EOS.

Still, for a given EOS the maximum mass model is, in general, distinct from the minimum period model. The intersection of the Kepler limiting curve with the line of onset of axisymmetric instability in a mass vs. central energy density graph defines the minimum period model [10, 36]. This intersection may be at lower or higher central energy density than that of the maximum mass model. In general, however, the central energy density, mass, period and other characteristics of the minimum period and maximum mass models nearly coincide. We have checked and confirmed that this is also true for the class of minimum period EOSs. Searching for the maximum mass model, instead of the exact minimum period model, introduces an error not larger than $1-2$ % in the minimum period and saves a tremendous amount of computing time.

We studied small perturbations of the minimum period EOS by slightly changing the slope of the constant pressure region or of the region at the causal limit for a wide range of M_{sph}^{max}. In all cases, the period was larger than that obtained by the minimum period equation of state.

We varied the matching number density n_m in order to check for its effect on the minimum period. Setting $n_m = 0$ (ignoring the low density EOS) reduced the minimum period by less than 3 % for any M_{sph}^{max}, compared to $n_m = 0.1$ fm^{-3}. Increasing the matching density to $n_m = 0.19$ fm^{-3} (from $n_m = 0.1$ fm^{-3}) increased the minimum period by less than 2 % for any M_{sph}^{max}. When we increased the matching density from $n_m = 0.1$ fm^{-3} to $n_m = 0.25$ fm^{-3} (which is much larger than the density for which one can trust FPS) the minimum period increased by less than 5 % for any M_{sph}^{max}. Thus, our results are relatively insensitive to the choice of matching number density n_m. Moreover, the bulk properties of the minimum period stars are determined by the causality limited region of the limiting equation of state, because the matching density is low compared to the central densities of the minimum period stars.

2.7 Comparison to Earlier Work

Glendenning [28] first obtained an estimate of the causal limit on the rotation of gravitationally bound stars. Rather than numerically computing rapidly rotating models, he computed nonrotating models and estimated the minimum period for a given EOS using the empirical formula

$$\frac{P_{\min}}{\mathrm{ms}} = 10.1 \left(\frac{M_{sph}^{max}}{\mathrm{M}_{\odot}}\right)^{-\frac{1}{2}} \left(\frac{R_{sph}^{max}}{10\ \mathrm{km}}\right)^{\frac{3}{2}}. \qquad (29)$$

This empirical formula involves only the mass M_{sph}^{max} and radius R_{sph}^{max} of the maximum mass nonrotating star for the given EOS. Friedman *et al.* [4] constructed this formula using realistic EOSs; it has has an uncertainty of about 10 % (see [37] for an improved version of the empirical formula). For a 1.442 $\mathrm{M}_{\odot}$ maximum mass nonrotating star Glendenning estimated the absolute minimum period to be 0.32-0.33 ms, which is 10-14 % larger than our computed value of 0.29 ms. The difference is as large as the uncertainty of the empirical formula (29), which is not surprising since when constructing the formula Friedman *et al.* [4] did not consider the then unknown class of minimum period EOSs. Our numerical results yield an empirical formula for the class of minimum period EOSs which is weakly dependent on the matching number density n_m. For a matching density of $n_m = 0.1\mathrm{fm}^{-3}$ the empirical formula is

$$\frac{P_{\min}}{\mathrm{ms}} = 0.847 \left(\frac{M_{sph}^{max}}{\mathrm{M}_{\odot}}\right)^{-\frac{1}{2}} \left(\frac{R_{sph}^{max}}{10\ \mathrm{km}}\right)^{\frac{3}{2}}, \qquad (30)$$

with an approximate uncertainty of 0.3 %.

Rather than identifying a single class of minimum period EOSs, Glendenning gave specific examples of minimum period EOSs with and without a constant pressure region. As we have demonstrated, the minimum period EOSs do have a constant pressure region, and are the limiting case of EOSs without a constant pressure region. We believe that Glendenning missed this and proposed two classes of minimum period EOSs because he used a modified Levenberg-Marquardt method [38] to minimize the function $f(M, P) = w_1(M - M_{sph}^{max})^2 + w_2 P^2$, where w_1 and w_2 are weights. Our own trials with this method showed that it is difficult to simultaneously obtain high accuracy for both M_{sph}^{max} and P_{min}.

2.8 Upper Limit on the Mass of Uniformly Rotating Neutron Stars

Rhoades and Ruffini [31] have shown that the EOS satisfying the constraints of section 2.2 and yielding the maximum mass compact star has a simple and unique form, consisting of two parts. The first part for low densities is a known low density EOS (earlier authors use the BPS EOS [39]). The second part, for densities greater than some matching density ϵ_m, is the causal limit EOS. Rhoades and Ruffini [31] chose a particular ϵ_m and computed a maximum mass of 3.2 $M_\odot$. Although 3.2 $M_\odot$ continues to be quoted as the theoretical maximum mass for neutron stars, as Hartle and Sabbadini [30] pointed out, M_{max} is sensitive to the matching energy density ϵ_m and a more accurate statement of the causality-set upper limit on the mass of compact spherical stars is

$$M_{sph}^{max} \simeq 4.8 \left(\frac{2 \times 10^{14} \text{ gr/cm}^3}{\epsilon_m} \right)^{1/2} \quad \mathrm{M}_\odot, \tag{31}$$

(cf. Hartle [40]). This is in sharp contrast to the class of minimum period EOSs, where, due to the constant pressure region, the minimum period is insensitive to the matching density. So 3.2 $M_\odot$ corresponds to a specific choice of ϵ_m and is not the theoretical maximum mass of neutron stars, which one needs to compute whenever new certainty of the EOS allows one to increase the matching density.

Friedman & Ipser [32] assumed that the causality-limited EOS yields the maximum mass for rotating stars as it does for nonrotating models. They computed, using an independent code, the maximum mass for different matching densities, assuming the BPS EOS for low densities. We also computed the maximum mass of rotating compact stars using the FPS EOS and our numerical code, which is based on a different algorithm than the Friedman & Ipser [32] code . Our results are summarized as

$$M_{rot}^{max} \simeq 6.1 \left(\frac{2 \times 10^{14} \text{ gr/cm}^3}{\epsilon_m} \right)^{1/2} \quad \mathrm{M}_\odot, \tag{32}$$

which is 3 % larger than the Friedman and Ipser result [32], and is within the numerical accuracy of the code used by Friedman and Ipser. Using the FPS rather than the BPS EOS did not significantly affect the maximum mass. In (32), 2×10^{14} gr/cm^3 is roughly the energy density up to which we trust the FPS EOS. If future research establishes the accuracy of FPS for higher energy densities, then (32) can be used to give an updated, lower value for M_{rot}^{max}.

The upper limit, set by causality, on the rotation of gravitationally bound stars, was obtained in this chapter for cold relativistic stars. In chapter 3, we will consider a different constraint on the rotation of warm relativistic stars, set by the emission of gravitational radiation.

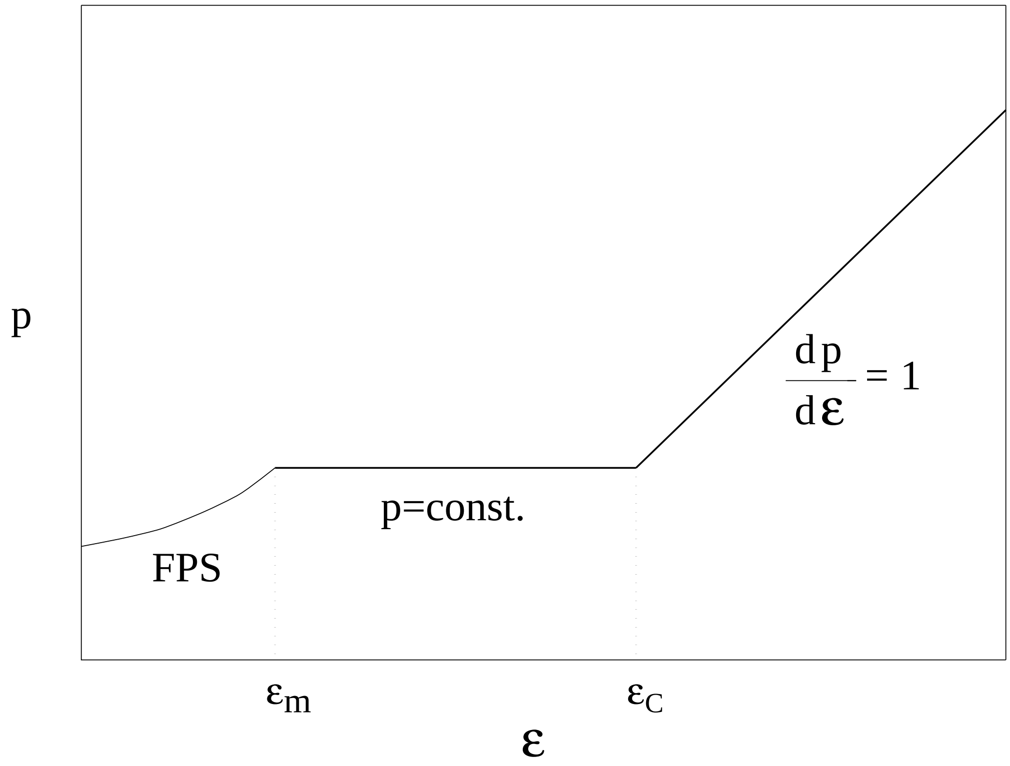

Figure 11: A schematic representation of the minimum period equation of state. The low density FPS equation of state is matched to a constant pressure region at an energy density ϵ_m. For $\epsilon > \epsilon_C$ the equation of state is at the causal limit $(dp/d\epsilon = 1)$. Note that in this graph both axes are linear.

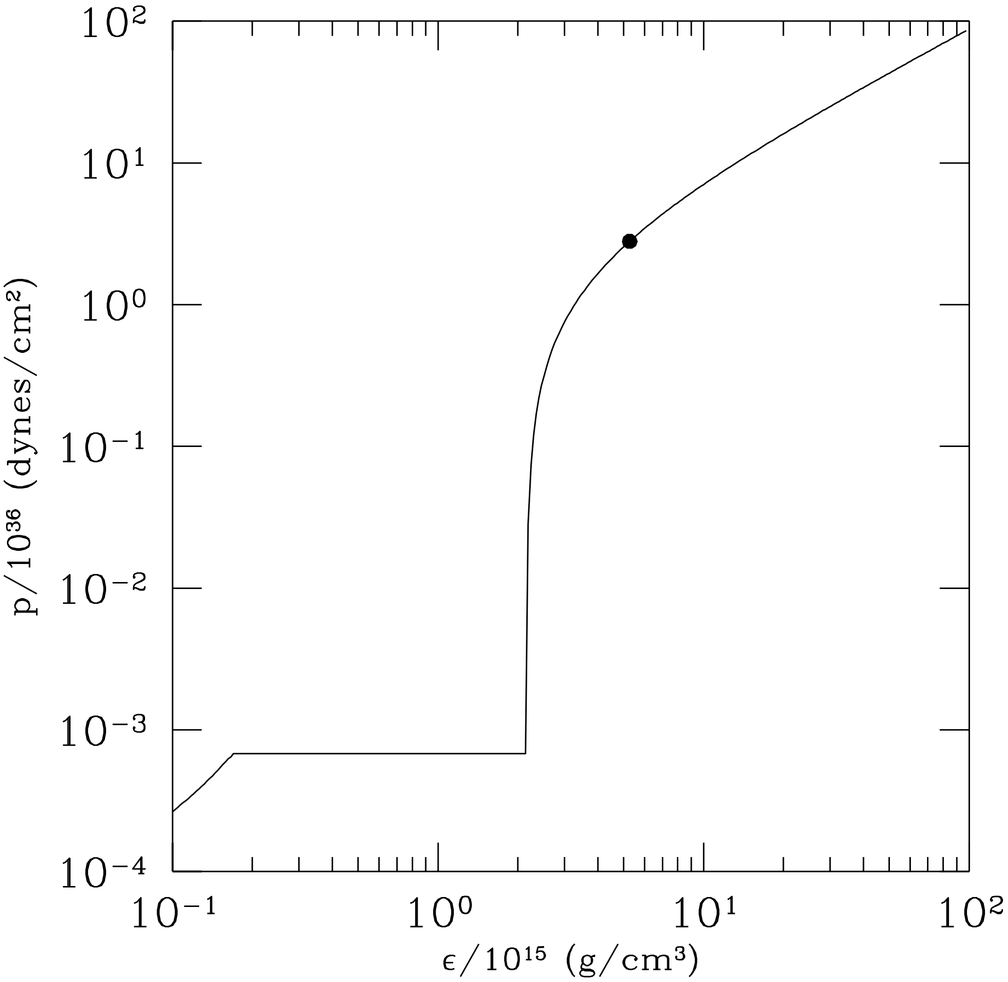

Figure 12: Equation of state yielding the minimum period $P_{min} = 0.29$ ms rotating star and a maximum mass nonrotating star of $M_s^{max} = 1.442\,\mathrm{M}_\odot$. The energy density at which the equation of state becomes causal is $\epsilon_C = 2.157 \times 10^{15}\mathrm{g/cm}^3$. The central energy density of the minimum period star is $5.274 \times 10^{15}\mathrm{g/cm}^3$ and is indicated by a filled circle on the equation of state curve. The matching number density is $n_m = 0.1\,\mathrm{fm}^{-3}$. Note that both axes are logarithmic.

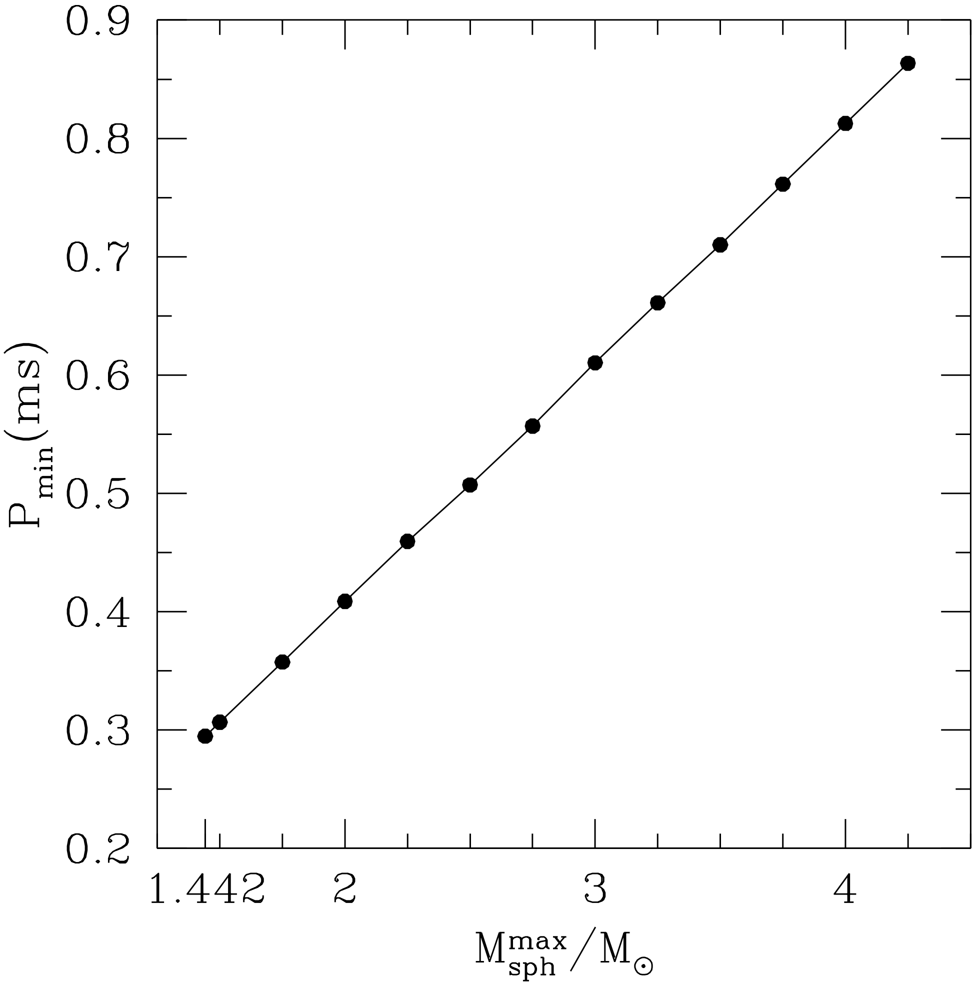

Figure 13: The minimum period P_{min} allowed for a rotating, relativistic star as a function of the mass M_{sph}^{max} of the maximum mass spherical star allowed by the equation of state of the stellar matter. The curve divides the mass-period plane into two regions. The region below the curve is not accessible to stars with equations of state that satisfy the constraints listed in section 2.2. The class of equations of state that yield the minimum period stars is given by (11).

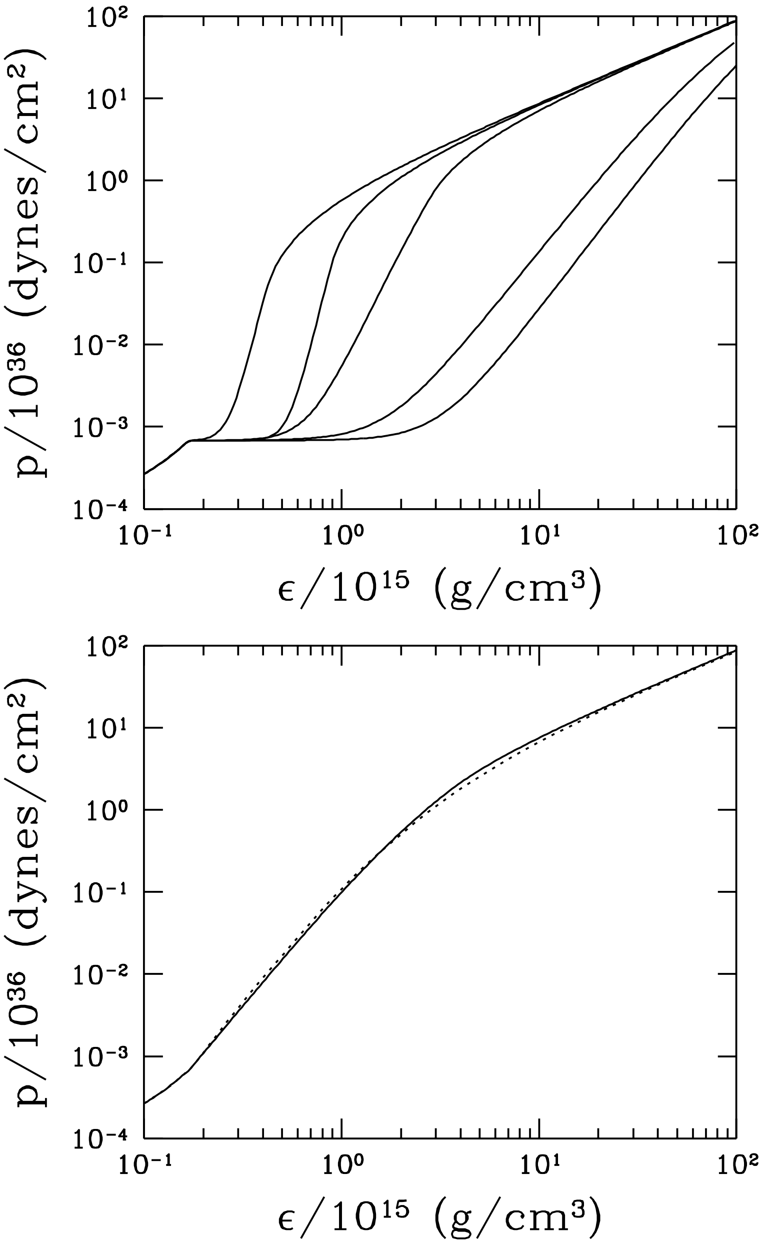

Figure 14: The top figure shows equations of state for different κ and γ using the parametrization (27) and (28). The $\kappa\gamma$ parametrized equation of state is very flexible and can produce both stiff and soft equations of state, as well as equations of state from the Arnett & Bowers catalog [41]. The dotted curve in the bottom figure shows equation of state C; the solid curve is a close approximation to EOS C using the $\kappa\gamma$ parametrization. Note that all axes are logarithmic.

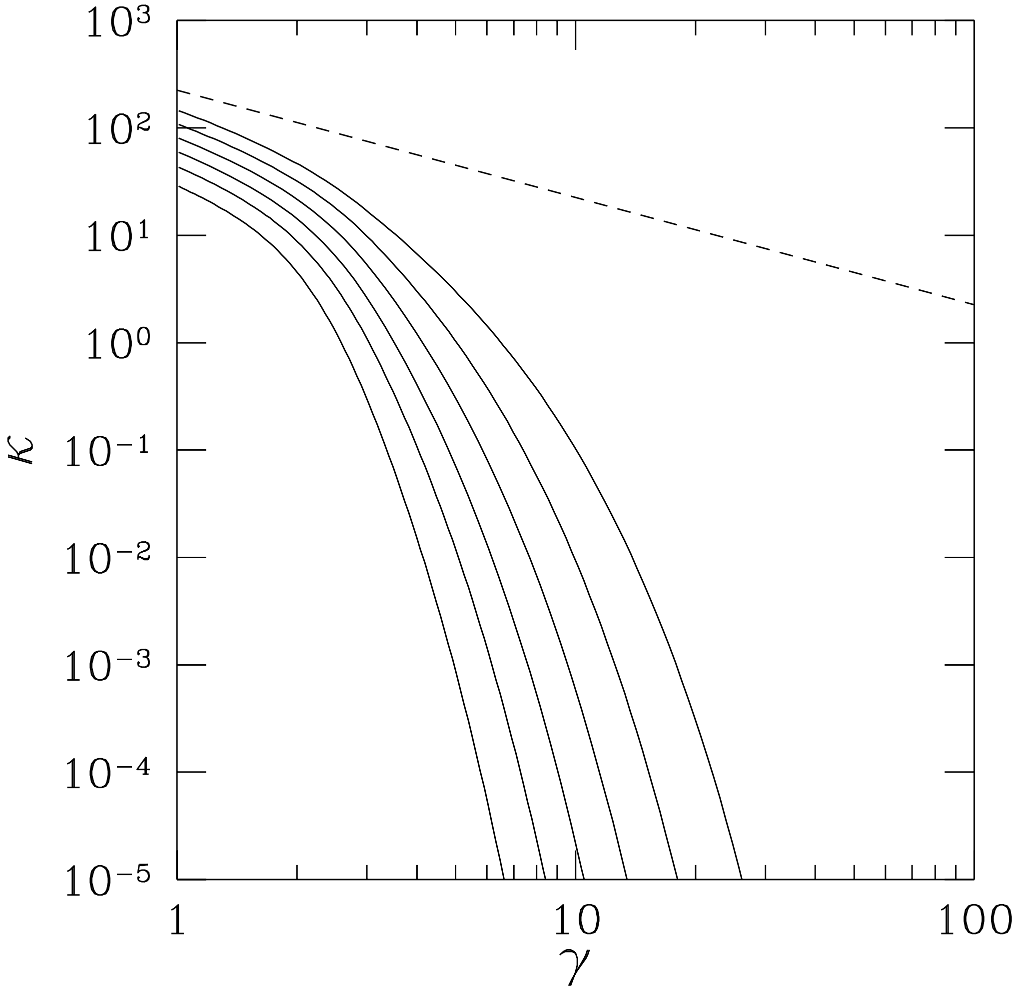

Figure 15: Lines of constant M_{sph}^{max} in the $\kappa\gamma$ plane. Each curve shows the possible combinations of κ and γ which, along with (27) and (28), define equations of state that yield a certain maximum mass M_{sph}^{max} for nonrotating relativistic stars. From left to right the curves correspond to $M_{sph}^{max}/\mathrm{M}_{\odot}$ = 1.442, 2.0, 2.5, 3.0, 3.5 and 4.5. The straight curve marks one edge of the boundary of the allowed region for κ and γ, which is defined by Eqs. (22-24).

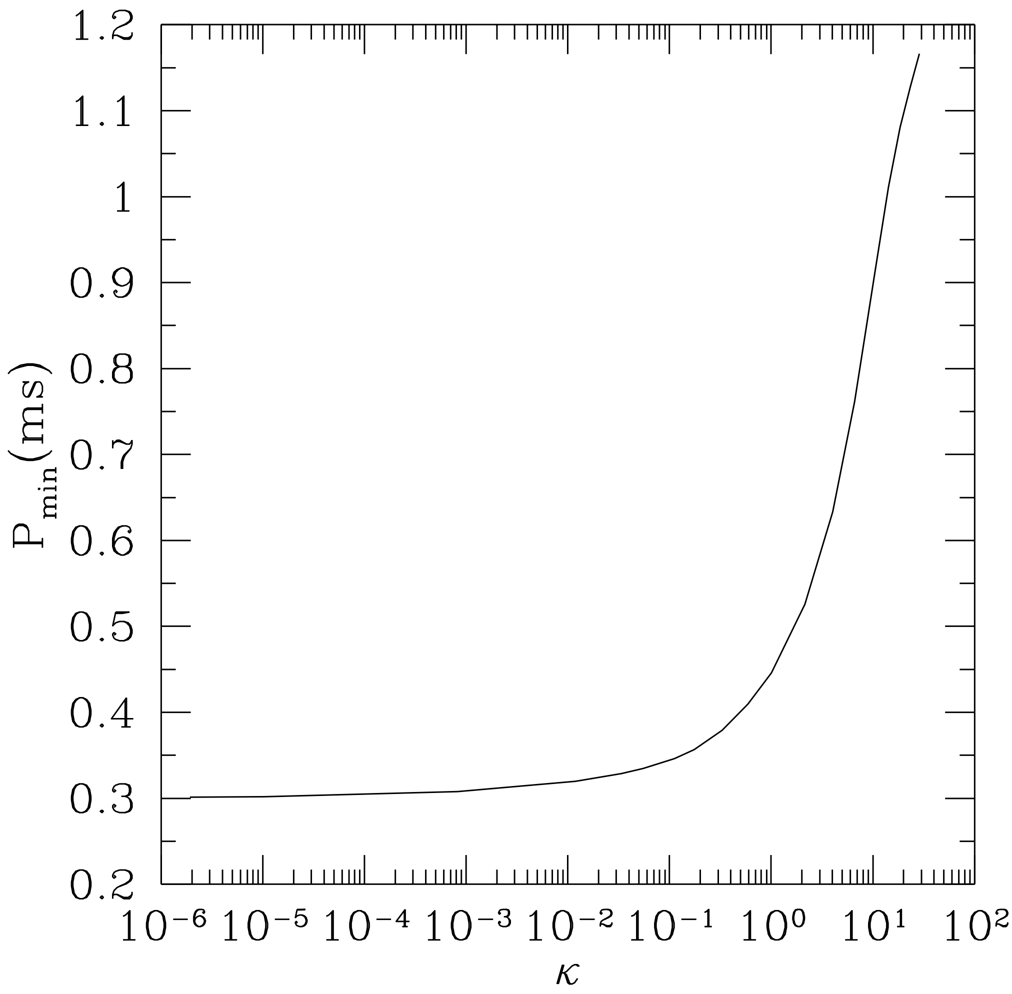

Figure 16: Minimum period allowed by equations of state given by (27) and (28) for different values of the parameter κ. All equations of state along the curve yield a maximum mass nonrotating star with $M_{sph}^{max} = 1.442\,\mathrm{M}_{\odot}$. Note that as $\kappa \to 0$ the period tends asymptotically to its minimum value.

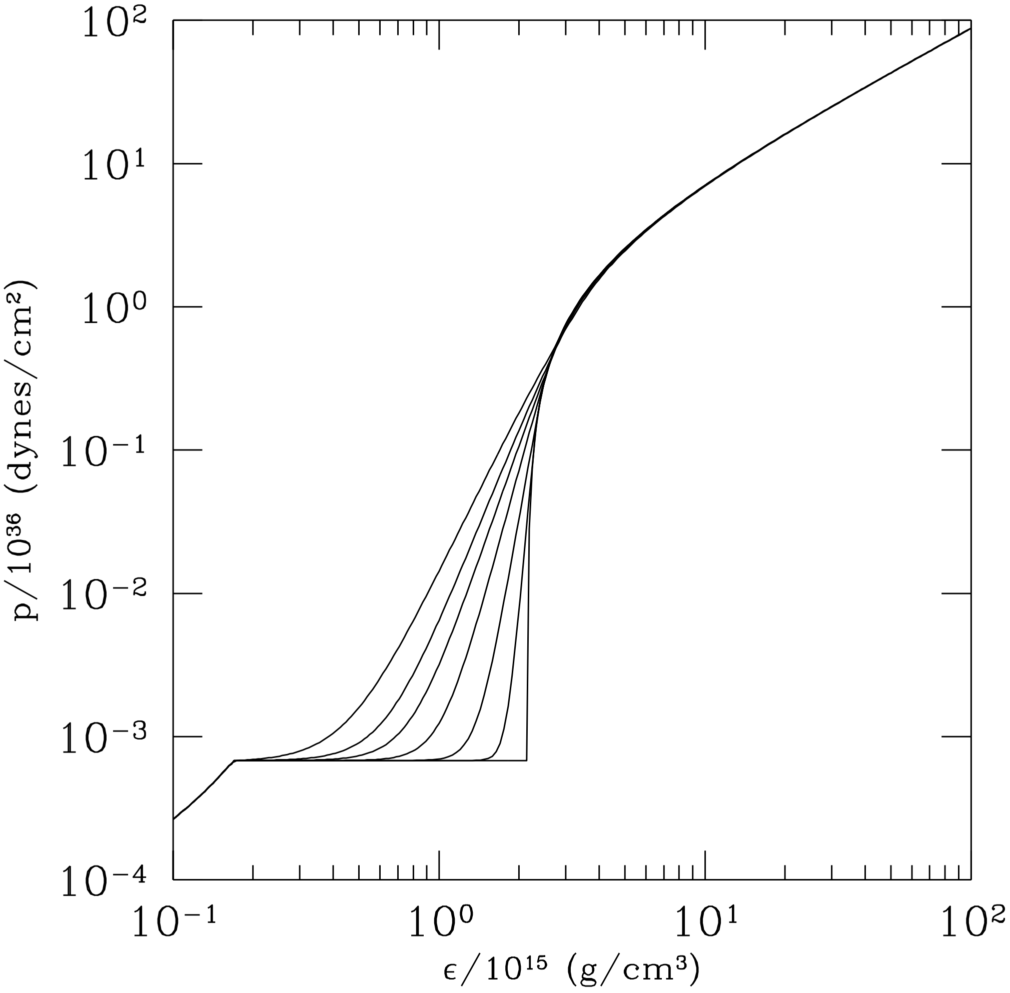

Figure 17: Different equations of state yielding the same $M_{sph}^{max} = 1.442\mathrm{M}_\odot$. As one moves along the leftmost curve in Figure 16 in the direction of decreasing κ, one samples the equations of state shown above in the direction of increasing energy density. As κ approaches zero, the equation of state manifests a nearly constant pressure region. In the limit when the pressure is constant, the equation of state yields the minimum period star. Note that both axes are logarithmic.

Chapter 3

Nonaxisymmetric Neutral Modes in Rotating Relativistic Stars

3.1 Introduction

Nonaxisymmetric instabilities driven by gravitational radiation may play a significant role in limiting the maximum angular velocity of neutron stars. Neutron stars that are formed by accretion-induced collapse of white dwarfs can spin very rapidly at birth because the white dwarf can spin-up to high angular velocities during the accretion (prior to collapse). If the spin of the newborn neutron star is close to the Kepler limit (the maximum allowed rotation, if a star is not to shed mass at it's equator), it will be subject to a nonaxisymmetric instability. This instability will allow nonaxisymmetric perturbations (left over from the violent collapse) to grow in time. The star will emit gravitational waves, thus losing angular momentum and spinning-down. When the star has cooled to lower temperatures, shear viscosity will finally damp the instability and the star will become nearly stationary with an angular velocity lower than at birth. The mathematical description of the nonaxisymmetric instability requires the solution of the equations governing perturbations of an equilibrium star. Because the unperturbed star is axisymmetric, one can expand a general perturbation in a sum of individual modes with angular dependence $e^{im\phi}$. Each mode corresponds, in the spherical limit, to one with angular behavior associated with the spherical harmonic Y_l^m. Thus, the study of nonaxisymmetric perturbations is simplified to studying individual nonaxisymmetric modes. Prior to the present work, the onset of the nonaxisymmetric instability had been computed only in the Newtonian limit and estimated in the first post-Newtonian approximation. The first fully relativistic computation is presented here.

That stars can be unstable to gravitational radiation was first found by Chandrasekhar [42], who considered the $m = 2$ modes for Maclaurin spheroids (uniform density rotating stars) in a Newtonian context. Friedman & Schutz [43, 44, 45, 46] show that this instability also appears in compressible stars and that all rotating "stars" (rotating self-gravitating perfect-fluid configurations) are generically unstable to the emission of gravitational radiation. Even for slowly rotating models there will always be a mode of high enough mode number m (equivalently, of short enough wavelength) that is unstable. However, short-wavelength unstable modes have extremely long growth times and for most stars, as noted below, viscosity damps out the instability. Friedman & Schutz [44] also discovered an important criterion for the onset of the nonaxisymmetric instability to gravitational radiation. A nonaxisymmetric mode becomes unstable when its frequency vanishes in the inertial frame, i.e with respect to an observer at infinity. This occurs when a star rotates fast enough that an inertial observer sees that a counterrotating mode becomes corotating with the star. The amplitude of the perturbation then grows with time, making the star unstable. Because of the way it sets in, the instability is also called rotational dragging instability. A zero-frequency mode is marginally unstable and is also called a *neutral mode*.

Realistic neutron stars are viscous and the presence of viscosity will shift the onset of instability. Work by Ipser & Lindblom [47, 48] and Yoshida & Eriguchi [49] in the Newtonian limit shows that viscosity will completely damp the instability for temperatures less than about 10^7 K and greater than about 10^{10} K, thus leaving a window of temperatures, where the instability will affect a sufficiently rapidly rotating neutron star as it cools down after its birth. In the Newtonian limit, only the $l = m \leq 5$ modes are not damped by viscosity and the $l = 4$ mode apparently sets the most stringent limit on the maximum angular velocity; the critical angular velocity is about 90 % to 95 % of the Kepler limit. Old neutron stars, spun-up by accretion, may be too cold to be subject to the gravitational radiation driven instability.

The onset of the nonaxisymmetric instability for several modes in rotating polytropes has been computed in the Newtonian limit by Imamura, Friedman & Durisen

[50] using a Langrangian variational principle and by Managan [51] and Ipser & Lindblom [52] using an Eulerian variational principle constructed by Ipser & Managan [53]. Cutler [54], Cutler & Lindblom [55] and Lindblom [56] estimate the correction to first post-Newtonian order. Since neutron stars are relativistic objects, relativity must have a significant effect on the onset of instability. The post-Newtonian analysis suggests that, for a given equation of state (EOS), and a given mode l, the ratio of the critical angular velocity where the mode becomes unstable to the maximum allowed angular velocity decreases as the neutron star becomes more relativistic. In realistic neutron stars thus, nonaxisymmetric instabilities set a more stringent limit on the maximum angular velocity than Newtonian theory suggests.

In this chapter, we compute the zero-frequency (neutral) modes of rotating polytropes of index $N = 1.0$, 1.5 and 2.0 in full general relativity. Attention is restricted to the fundamental (f) $l = m \leq 5$ modes, since these are the ones that are most likely to participate in limiting the maximum angular velocity in neutron stars. It is shown that the critical angular velocities of relativistic stars are considerably lower than the corresponding Newtonian estimates. As a result, the $m = 2$ bar mode can become unstable for much softer ($N < 1.3$) polytropes than in the Newtonian limit. This is expected to hold true for most realistic EOSs since they have an effective index $N < 1.0$. Thus, depending on the equation of state and the effect of viscosity, the $m = 2$ mode may participate in setting the upper limit on rotation for rapidly rotating neutron stars created by the accretion-induced collapse of white dwarfs.

In forthcoming work we plan to include the effect of viscosity on the critical angular velocities and extend our method to $N < 1.0$ polytropes and to realistic equations of state.

3.2 The Equilibrium Configurations

The spacetime of a rotating relativistic star in equilibrium can be described by the stationary, axisymmetric metric introduced in section 1.2

$$ds^2 = -e^{2\nu}dt^2 + e^{2\psi}(d\phi - \omega dt)^2 + e^{2\alpha}(dr^2 + r^2 d\theta^2), \tag{33}$$

(for a review see Friedman & Ipser [19]). In (33), as in the rest of the chapter, gravitational units ($c = 1$, $G = 1$) are employed. The metric involves four independent equilibrium metric potentials ν, ψ, α and ω which are functions of r and θ only. We assume uniform rotation, $\Omega =$ constant, where Ω is the angular velocity of the star. The matter is assumed to be a perfect fluid at zero temperature, described by a polytropic equation of state, for which the energy density ϵ, pressure P and number density n satisfy the relations

$$\begin{aligned} P &= Kn^{1+1/N}, && (34) \\ \epsilon &= nm_{\rm B} + NKn^{1+1/N}, && (35) \end{aligned}$$

where K is a constant, $m_{\rm B}$ is the rest mass per baryon and N is the polytropic index. The stress-energy tensor for a perfect fluid is

$$T^{ab} = (\epsilon + P)u^a u^b + Pg^{ab}, \tag{36}$$

where u^a is the 4-velocity of the fluid, given by

$$u^a = \frac{e^{-\nu}}{\sqrt{1-v^2}}(t^a + \Omega\phi^a), \tag{37}$$

with

$$v = (\Omega - \omega)e^{\psi-\nu}, \tag{38}$$

being the velocity of fluid elements with respect to a local zero-angular momentum observer. In (38), t^a and ϕ^a are the Killing vectors associated with the time and rotational symmetries of the metric. With respect to the coordinates x^i of (33), t^a and ϕ^a have components

$$\begin{aligned} t^i &= (1,0,0,0), && (39) \\ \phi^i &= (0,0,0,1). && (40) \end{aligned}$$

The stress-energy tensor is conserved, in the sense that

$$\nabla_a T^{ab} = 0, \tag{41}$$

where ∇_a is the covariant derivative compatible with the unperturbed metric g_{ab}. From (41) one obtains the Euler equation

$$q^c{}_b \nabla_a T^{ab} = 0 \tag{42}$$
$$\Longrightarrow \quad u^a \nabla_a u^b = -\frac{q^{bc}\nabla_c P}{\epsilon + P}, \tag{43}$$

and the equation of energy conservation

$$u_b \nabla_a T^{ab} = 0, \tag{44}$$
$$\Longrightarrow \quad u^a \nabla_a \epsilon = -(\epsilon + P)\nabla_a u^a. \tag{45}$$

In (43), $q^{ab} = g^{ab} + u^a u^b$ is the projection of the metric tensor orthogonal to the 4-velocity. The adiabatic index of the equilibrium fluid is

$$\Gamma_0 = \frac{d\ln P}{d\ln n} = \frac{\epsilon + P}{P}\frac{dP}{d\epsilon} = 1 + \frac{1}{N}. \tag{46}$$

An equilibrium model is constructed by solving the field equations

$$R_{ab} = 8\pi\Big(T_{ab} - \frac{1}{2}g_{ab}T\Big), \tag{47}$$

(where R_{ab} is the Ricci tensor and $T \equiv T_a{}^a$), using a numerical code (Stergioulas & Friedman [36]) that implements the Cook, Shapiro & Teukolsky [10] version of the KEH method (Komatsu, Eriguchi & Hachisu [7]). Our code has been shown to be accurate in an extensive comparison with other existing codes (Eriguchi *et al.* [23]). The field equations are solved on a 2-dimensional grid that is uniform in $\mu \equiv \cos\theta$ and in the radial coordinate

$$s = r/(r + r_e), \tag{48}$$

which compactifies the region $r = 0$ to $+\infty$ to the finite region $s = 0$ to 1 (r_e is the value of the coordinate r at the equator). This is important, since the gravitational potentials have a nonnegligible value even far from a relativistic star and it also simplifies the implementation of boundary conditions in the construction of both the equilibrium and the perturbed configurations. Note that the equator of the star is always at $s = 0.5$, so that (for a nonrotating star) half of the radial grid-points are inside the star and the other half are outside.

We define dimensionless quantities by setting $G = c = 1$ (gravitational units) and by fixing the length scale. If we define

$$\tilde{K} = \frac{K}{m_{\mathrm{B}}^{1+1/N}}, \tag{49}$$

then $\tilde{K}^{N/2}$ can be used as the fundamental length scale. Dimensionless quantities will be denoted as $\bar{\epsilon}$, $\bar{\Omega}$ etc. The dimensionless energy density and angular velocity are then

$$\bar{\epsilon} = \frac{\tilde{K}^N G}{c^4}\epsilon, \tag{50}$$

and

$$\bar{\Omega} = \frac{\tilde{K}^{N/2}}{c}\Omega. \tag{51}$$

In subsequent sections, numerical results will be reported using dimensionless quantities as defined above.

3.3 The Perturbed Configurations

Perturbations of an equilibrium star can be studied by way of two formalisms. In the Eulerian formalism, one compares a quantity Q in the unperturbed configuration to Q' in the perturbed configuration at the same point in space. In the Langrangian formalism, one defines a Lagrangian displacement vector ξ^a, which connects fluid elements in the equilibrium with corresponding ones in the perturbed configuration. The Lagrangian change ΔQ is defined as the change in Q with respect to a frame dragged by ξ^a. The Lagrangian change is related to the Eulerian change by

$$\Delta Q = \delta Q + \mathcal{L}_\xi Q, \tag{52}$$

where $\mathcal{L}_\xi$ is the Lie derivative along ξ^a (the above definition was introduced by Taub [57] and used in Friedman & Schutz [44, 45] - it agrees with that of Chandrasekhar & Lebovitz [58, 59] and of Lynden-Bell & Ostriker [60] only for scalars). The Lagrangian approach has been successfully implemented by Imamura, Friedman & Durisen [50] in computing the onset of the secular instability in the Newtonian limit. Bardeen *et al.* [61] note that in the Lagrangian formalism there exist trivial displacements ξ^a which do not correspond to a physical perturbation, so that one has to identify and exclude these displacements from the variational principle (see also [46]). The Eulerian approach is free of this difficulty.

The Eulerian perturbation in the metric tensor is commonly denoted by

$$\delta g_{ab} \equiv h_{ab}, \tag{53}$$

and can be determined by solving the perturbed field equations

$$\delta R_{ab} = 8\pi(\delta T_{ab} - \frac{1}{2} g_{ab}\delta T - \frac{1}{2} h_{ab} T), \tag{54}$$

in a suitably chosen gauge. The perturbation h_{ab} in the metric is assumed to be small with respect to the unperturbed metric g_{ab}. The perturbation in any other quantity is carried only to first order in h_{ab}. The change in the Ricci tensor is then (see e.g. Carter [62])

$$\delta R_{ab} = \nabla_c \nabla_{(a} h^c{}_{b)} - \frac{1}{2}\Big(\nabla_a \nabla_b h_c{}^c + \nabla^c \nabla_c h_{ab}\Big). \tag{55}$$

Priou [65] has explicitly computed the components of δR_{ab} for a stationary, axisymmetric background in its most general form (before any gauge is chosen). This allows us to directly use Priou's results with only the following modifications: i) since we are only interested in zero-frequency modes, we set the frequency of the mode and all time-derivatives equal to zero; ii) we rename Priou's functions m to M, l to L and Ω to y, in order to avoid confusion with the indices l, m that characterize a mode and with the angular velocity Ω of the equilibrium star; and iii) we choose a gauge as described in section 3.5. The components of δR_{ab} in our gauge are displayed in Appendix B.

The perturbation in the stress-energy tensor is

$$\delta T_{ab} = u_a u_b(\delta\epsilon + \delta P) + (\epsilon + P)(u_a \delta u_b + u_b \delta u_a) + g_{ab}\delta P + P h_{ab},, \tag{56}$$

while the perturbation in its contraction is

$$\delta T = 3\delta P - \delta\epsilon, \tag{57}$$

The change in the pressure and energy density can be expressed in terms of a single scalar function δU

$$\begin{aligned} \delta P &= (\epsilon + P)(\delta U + \frac{1}{2} u^a u^b h_{ab}), & (58) \\ \delta \epsilon &= \frac{(\epsilon + P)}{P \Gamma} \delta P, & (59) \end{aligned}$$

which in the Newtonian limit agree with the corresponding expressions in Managan [51] and Ipser & Managan [53]. The adiabatic index Γ of the perturbation is taken to be equal to the adiabatic index Γ_0 of the equilibrium configuration, defined in (46), by assuming that small perturbations will have a negligible effect on the equation of state of the fluid.

Ipser & Managan [53] discovered that the Newtonian perturbed Euler equations can be solved analytically for the perturbation $\delta \vec{v}$ in the velocity of the fluid. Then, Ipser & Lindblom [63] generalized this to the relativistic perturbed Euler equations

$$\delta(q^c{}_b \nabla_a T^{ab}) = 0, \tag{60}$$

which they solved analytically for the perturbation δu^a in the 4-velocity. This greatly simplifies the problem, since now the free variables are only h_{ab} and the single scalar function δU instead of h_{ab} and the components of δu^a. For zero-temperature stars, the perturbation in the 4-velocity is given by

$$\delta u^a = i\ Q^{ab} \Big[\nabla_b (\delta U + \frac{1}{2} u^c u^d h_{cd}) - \delta F_b \Big] + \frac{1}{2} u^a u^c u^d h_{cd}, \tag{61}$$

where

$$\delta F_a = q_a{}^b \left[-u^c \nabla_c (h_{bd} u^d) + u^c u^d \nabla_b h_{cd} + u^c u^d h_{cd} \frac{\nabla_b P}{\epsilon + P} \right], \tag{62}$$

and the tensor Q^{ab} involves only equilibrium quantities. Note that the sum $\delta U + \frac{1}{2} u^a u^b h_{ab}$ in (58) and (61) corresponds to δU in Ipser & Lindblom [63]. The covariant definition of Q^{ab} is

$$Q^{ab} = \frac{\Lambda}{\sigma^3 \gamma^3} \Big[\sigma^2 \gamma^2 q^{ab} - 2 \omega^a \Omega^b + i \sigma \gamma (2 \hat{\phi}^b \epsilon^{ac} \Omega_c - \hat{\phi}^a \epsilon^{bc} \omega_c) \Big], \tag{63}$$

where σ is the frequency of the mode in the rotating frame and γ is defined as

$$\gamma \equiv u_a t^a. \tag{64}$$

In (63), ω^a is the vorticity of the fluid

$$\omega^a = \epsilon^{abcd} u_b \nabla_c u_d, \tag{65}$$

and Ω^a is a generalization of the angular-velocity vector

$$\Omega^a = \frac{1}{2}\gamma \epsilon^{abcd} u_b (\nabla_c t_d + \Omega \nabla_c \phi_d), \tag{66}$$

where ϵ^{abcd} is the 4-volume element. The unit linear combination of the Killing fields that is orthogonal to u^a is

$$\hat{\phi}^a = \frac{q^{ab}\phi_b}{\bar{\omega}\gamma}, \tag{67}$$

with $\bar{\omega}^2 = -t^a t_a \phi^b \phi_b + (t^a \phi_a)^2$. The tensor ϵ^{ab} is the volume element on the 2-surfaces that are orthogonal to the Killing trajectories

$$\epsilon^{ab} = \epsilon^{abcd} \hat{\phi}_c u_d. \tag{68}$$

The scalar Λ in (63) is related to the determinant (defined with respect to the 3-volume element $\epsilon^{abc} = \epsilon^{abcd} u_d$)

$$\det(Q^{-1})^a{}_b = \sigma^3\gamma^3 - 2\sigma\gamma\Omega^a\omega_a \equiv \frac{\sigma^3\gamma^3}{\Lambda}, \tag{69}$$

where Q^{-1}_{ab} is defined through $Q^{ac}Q^{-1}_{cb} = q^a{}_b$. The tensor Q^{ab} exists (and the perturbed Euler equations can be inverted) as long as the determinant in (69) does not vanish.

The components of Q^{ab} for a stationary, axisymmetric background are

$$\begin{aligned}
Q^{tt} &= \frac{S^2\Lambda}{\sigma\gamma^3 e^{2(\psi+\nu)}} && (70)\\
Q^{tr} &= -i\,\frac{r\omega^\theta e^{\psi+\nu}}{\sigma S} Q^{tt} && (71)\\
Q^{rt} &= -Q^{tr} && (72)\\
Q^{t\theta} &= -\frac{\omega^r}{r^2\omega^\theta} Q^{tr} && (73)\\
Q^{\theta t} &= -Q^{t\theta} && (74)
\end{aligned}$$

$$
\begin{aligned}
Q^{t\phi} &= \frac{(1+\Omega S)}{S} Q^{tt} && (75)\\
Q^{\phi t} &= Q^{t\phi} && (76)\\
Q^{rr} &= \frac{\Lambda}{\sigma^3\gamma^3}\left[\sigma^2\gamma^2 e^{-2\alpha} - (\omega^r)^2\right] && (77)\\
Q^{r\theta} &= -\frac{\Lambda\omega^r\omega^\theta}{\sigma^3\gamma^3} && (78)\\
Q^{\theta r} &= -Q^{r\theta} && (79)\\
Q^{r\phi} &= \frac{(1+\Omega S)}{S} Q^{rt} && (80)\\
Q^{\phi r} &= -Q^{r\phi} && (81)\\
Q^{\theta\theta} &= \frac{\Lambda}{r^2\sigma^3\gamma^3}\left[\sigma^2\gamma^2 e^{-2\alpha} - r^2(\omega^\theta)^2\right] && (82)\\
Q^{\theta\phi} &= \frac{(1+\Omega S)}{S} Q^{\theta t} && (83)\\
Q^{\phi\theta} &= -Q^{\theta\phi} && (84)\\
Q^{\phi\phi} &= \frac{(1+\Omega S)}{S} Q^{\phi t} && (85)
\end{aligned}
$$

The scalar S is defined as

$$
S \equiv u^t u_\phi = \gamma^2(\Omega - \omega)e^{2\psi}, \tag{86}
$$

while

$$
\begin{aligned}
\gamma &\equiv u^t = \left[e^{2\nu} - (\Omega-\omega)^2 e^{2\psi}\right]^{-1/2} && (87)\\
\omega^r &= \frac{e^{-(2\alpha+\psi+\nu)}}{\gamma^2 r}\frac{\partial S}{\partial\theta} && (88)\\
\omega^\theta &= -\frac{e^{-(2\alpha+\psi+\nu)}}{\gamma^2 r}\frac{\partial S}{\partial r}, && (89)
\end{aligned}
$$

and (for a mode of zero frequency in the inertial frame)

$$
\sigma = m\Omega. \tag{90}
$$

The perturbed covariant 4-velocity is given by

$$
\delta u_a = \delta u^b g_{ab} + u^b h_{ab}. \tag{91}
$$

Through (58), (59), (61), (62) and (91) the perturbation in the stress-energy tensor δT_{ab} is expressed entirely in terms of the perturbation in the metric h_{ab} and the scalar function δU. Due to the lengthy substitutions involved, we used the algebraic program MAPLE to compute δu_a which was then substituted in δT_{ab}. The expressions for the components of δT_{ab} in the stationary, axisymmetric background are several pages long (for each component) and thus we do not display them here. These expressions, along with the components of δR_{ab}, are used to form the perturbed field equations (54). MAPLE is used to convert these expressions into numerical code for inclusion in an ANSI-C program.

The perturbed field equations determine h_{ab} for given δU. The scalar function δU is determined by an additional equation, the perturbed energy conservation equation

$$\delta(u_b \nabla_a T^{ab}) = 0. \tag{92}$$

which will be considered in section 3.8.

3.4 Expansion in Spherical Harmonics

The presence of an axisymmetric background allows all perturbed quantities to be expanded in terms of normal modes, i.e. as functions of r and θ multiplied by $e^{im\phi}$ (in the case of zero frequency). Following Regge & Wheeler [64], we expand the angular part of the components of h_{ab} in terms of scalar, vector and tensor harmonics. In the spherical limit, one can use gauge transformations to decouple general perturbations into two distint classes; even parity (polar) modes, which induce fluid pulsations, and odd-parity (axial modes), which induce small fluid pulsations only in the presence of anisotropic stresses. In the presence of rotation, the axial and polar modes couple: modes, that in the spherical limit can be written as purely polar modes, will have an axial part, if the background star is rotating, and vice versa.

Since scalars are of even parity, they are expanded in terms of the spherical harmonic Y_l^m. Vectors on the θ-ϕ 2-sphere are expanded in terms of $\Psi^m_{l\ \mu}$ (even parity) and $\Phi^m_{l\ \mu}$ (odd parity), where $\mu = \theta, \phi$. Tensors are expanded in terms of $\Phi^m_{l\ \mu\nu}$ and $\Psi^m_{l\ \mu\nu}$ (both are of even parity) and $\chi^m_{l\ \mu\nu}$ (odd parity), where $\mu, \nu = \theta, \phi$. The above mentioned functions are defined as follows:

$$\Psi^m_{l\ \theta} = \frac{\partial}{\partial\theta} Y^m_l \tag{93}$$
$$\Psi^m_{l\ \phi} = \frac{\partial}{\partial\phi} Y^m_l \tag{94}$$
$$\tag{95}$$
$$\Phi^m_{l\ \theta} = -\frac{1}{\sin\theta}\frac{\partial}{\partial\phi} Y^m_l \tag{96}$$
$$\Phi^m_{l\ \phi} = \sin\theta\frac{\partial}{\partial\theta} Y^m_l \tag{97}$$
$$\tag{98}$$
$$\Phi^m_{l\ \theta\theta} = Y^m_l \tag{99}$$
$$\Phi^m_{l\ \theta\phi} = 0 \tag{100}$$
$$\Phi^m_{l\ \phi\phi} = \sin^2\theta\ Y^m_l \tag{101}$$
$$\tag{102}$$
$$\Psi^m_{l\ \theta\theta} = \frac{\partial^2}{\partial\theta^2} Y^m_l \tag{103}$$
$$\Psi^m_{l\ \theta\phi} = \Big(\frac{\partial^2}{\partial\theta\partial\phi} - \cot\theta\frac{\partial}{\partial\phi}\Big) Y^m_l \tag{104}$$
$$\Psi^m_{l\ \phi\phi} = \Big(\frac{\partial^2}{\partial\phi^2} + \sin\theta\cos\theta\frac{\partial}{\partial\theta}\Big) Y^m_l \tag{105}$$
$$\tag{106}$$
$$\chi^m_{l\ \theta\theta} = \frac{1}{\sin\theta}\Big(\frac{\partial^2}{\partial\theta\partial\phi} - \cot\theta\frac{\partial}{\partial\phi}\Big) Y^m_l \tag{107}$$
$$\chi^m_{l\ \theta\phi} = \frac{1}{2}\Big(\frac{1}{\sin\theta}\frac{\partial^2}{\partial\phi^2} + \cos\theta\frac{\partial}{\partial\theta} - \sin\theta\frac{\partial^2}{\partial\theta^2}\Big) Y^m_l \tag{108}$$
$$\chi^m_{l\ \phi\phi} = -\sin\theta\Big(\frac{\partial^2}{\partial\theta\partial\phi} - \cot\theta\frac{\partial}{\partial\phi}\Big) Y^m_l \tag{109}$$

A most general tensor is thus expanded schematically as

$$h_{tt},\ h_{tr},\ h_{rr} \propto \sum_{l,m} a_{lm}\ Y^m_l \tag{110}$$
$$h_{t\mu},\ h_{r\mu} \propto \sum_{l,m}\Big(a_{lm}\ \Psi^m_{l\ \mu} + b_{lm}\ \Phi^m_{l\ \mu}\Big) \tag{111}$$
$$h_{\mu\nu} \propto \sum_{l,m}\Big(\ a_{lm}\ \Phi^m_{l\ \mu\nu} + b_{lm}\ \Psi^m_{l\ \mu\nu} + c_{lm}\ \chi^m_{l\ \mu\nu}\Big), \tag{112}$$

where the a_{lm}'s, b_{lm}'s and c_{lm}'s are complex coefficients, different for each component of h_{ab}.

We are interested not in the most general case, but in specific modes only. In particular, we are interested in those modes that, in the spherical limit, reduce to polar, $l = m$ fundamental modes. The presence of rotation introduces terms in the expansion of h_{ab} that are of higher l but of same m. The symmetries of the background require each component of h_{ab} to be either symmetric or antisymmetric under the transformation $\theta \to \pi - \theta$. Thus, a polar l-term will be coupled to an axial $l+1$-term. For zero-frequency solutions, h_{tr}, $h_{t\theta}$, $h_{r\phi}$, and $h_{\theta\phi}$ differ by a phase factor of $e^{i\pi/2}$ from the other perturbed potentials. Finally, we require our gauge to be such that the solution reduces in the spherical limit to a polar mode in the Regge-Wheeler gauge, in which only h_{tt}, h_{rr}, $h_{\theta\theta}$ and $h_{\phi\phi}$ are non-zero, with $h_{\phi\phi} = \sin^2\theta\ h_{\theta\theta}$ (in Schwarzschild coordinates).

Taking into account all of the above requirements, we find that the Eulerian perturbation in the metric of a polar, $l = m$, zero-frequency mode of a rotating star (polar in the sense that it reduces to a purely polar mode in the spherical limit) will have the following expansion:

$$h_{tt}, h_{rr} \propto \sum_{l'=0}^{\infty} a_{m+2l'}\ Y^m_{m+2l'} \tag{113}$$

$$h_{tr} \propto \sum_{l'=0}^{\infty} i\ a_{m+2l'+2}\ Y^m_{m+2l'+2} \tag{114}$$

$$h_{t\mu} \propto \sum_{l'=0}^{\infty}\Big(i\ a_{m+2l'+2}\ \Psi^m_{m+2l'+2\ \mu} + b_{m+2l'+1}\ \Phi^m_{m+2l'+1\ \mu}\Big) \tag{115}$$

$$h_{r\mu} \propto \sum_{l'=0}^{\infty}\Big(a_{m+2l'+2}\ \Psi^m_{m+2l'+2\ \mu} + i\ b_{m+2l'+1}\ \Phi^m_{m+2l'+1\ \mu}\Big) \tag{116}$$

$$h_{\mu\nu} \propto \sum_{l'=0}^{\infty}\Big(a_{m+2l'}\ \Phi^m_{m+2l'\ \mu\nu} + b_{m+2l'+2}\ \Psi^m_{m+2l'+2\ \mu\nu} + i\ c_{m+2l'+1}\ \chi^m_{m+2l'+1\ \mu\nu}\Big) \tag{117}$$

where the a's, b's, and c's are again different for each expansion, but real.

In Priou's [65] notation (and with our own redefinitions mentioned in section 3.3), the ten components of h_{ab} are expressed in terms of ten *perturbation functions* $h, p, k, w, q, a, b, L, M$, and y as

$$
\begin{aligned}
h_{tt} &= -2he^{2\nu} + (2y\omega + 2w\omega^2)e^{2\psi} && (118) \\
h_{tr} &= L + a\omega e^{2\psi} && (119) \\
h_{t\theta} &= M + b\omega e^{2\psi} && (120) \\
h_{t\phi} &= -e^{2\psi}(y + 2\omega w) && (121) \\
h_{rr} &= 2ke^{2\alpha} && (122) \\
h_{r\theta} &= q && (123) \\
h_{r\phi} &= -ae^{2\psi} && (124) \\
h_{\theta\theta} &= 2pr^2e^{2\alpha} && (125) \\
h_{\theta\phi} &= -be^{2\psi} && (126) \\
h_{\phi\phi} &= 2we^{2\psi}, && (127)
\end{aligned}
$$

i.e. the perturbed metric has the form

$$
\begin{aligned}
(g_{ab} + h_{ab})dx^a dx^b &= -e^{2\nu}(1+2h)dt^2 + e^{2\psi}(1+2w)\Big[d\phi - (\omega + y)dt \\
&\quad - adr - bd\theta\Big]^2 + e^{2\alpha}\Big[(1+2k)dr^2 + r^2(1+2p)d\theta^2\Big] \\
&\quad + 2qdrd\theta + 2Ldtdr + 2Mdtd\theta. && (128)
\end{aligned}
$$

We find that, if one defines new variables

$$
\begin{aligned}
\hat{L} &= -i\ L && (129) \\
\hat{M} &= -i\ M\sin\theta && (130) \\
\hat{q} &= q\sin\theta && (131) \\
\hat{y} &= y\sin^2\theta && (132) \\
\hat{a} &= -i\ a\sin^2\theta && (133) \\
\hat{b} &= -i\ b\sin^3\theta && (134) \\
\hat{p} &= p\sin^2\theta && (135) \\
\hat{w} &= w\sin^2\theta, && (136)
\end{aligned}
$$

then the metric perturbations of these modes can be expanded in terms of Legendre polynomials schematically as

$$h,\ k,\ \hat{L},\ \hat{y},\ \hat{a},\ \hat{p},\ \hat{w} \ \sim\ \sin^m\theta \sum_{l'=0}^{\infty} a_{2l'}(r)P_{2l'}(\cos\theta), \tag{137}$$

$$\hat{M},\ \hat{q},\ \hat{b} \ \sim\ \sin^m\theta \sum_{l'=0}^{\infty} a_{2l'+1}(r)P_{2l'+1}(\cos\theta), \tag{138}$$

where the $e^{im\phi}$ dependence is implied and will be dropped from now on, unless otherwise stated. It is obvious from (137) and (138), that the functions $\hat{M}, \hat{q}$ and $\hat{b}$ will be antisymmetric about the equatorial plane, while all other functions will be symmetric. Furthermore, with these definitions, *the time-independent perturbed field equations become a system of ten real equations for ten real unknowns.*

The corresponding expansions for axial $l = m$ modes, that reduce to axial modes in the Regge-Wheeler gauge in the spherical limit, can easily be written down in a similar fashion. We note that the reflection symmetry of the perturbation functions in the equatorial plane will be opposite for these axial modes than they are for the polar modes. This difference in reflection symmetry makes it easy to restrict a numerical investigation to either polar or axial $l = m$ modes by applying the corresponding boundary conditions in the equatorial plane.

3.5 Gauge Choice

Linear perturbations are invariant under gauge transformations, i.e. under an infinitesimal diffeomorphism generated by a vector field η^a. A perturbation of a star, described by the set of quantities ($\delta\epsilon$, δP, δu^a, h_{ab}) is physically equivalent to the gauge-related perturbation described by the set ($\delta\epsilon + \mathcal{L}_\eta\epsilon$, $\delta P + \mathcal{L}_\eta P$, $\delta u^a + \mathcal{L}_\eta u^a$, $h_{ab} + \mathcal{L}_\eta g_{ab}$).

The choice of gauge is important for the successful numerical solution of the perturbed field equations, since in some (if not most) gauges the system of coupled differential equations is difficult to solve numerically. After experimenting with a large number of possible gauges, we found that a numerical solution was more easily obtained in a gauge defined by the four conditions

$$h_{r\theta} \ = \ 0 \quad \Longrightarrow q = 0, \tag{139}$$

$$\begin{aligned}
h_{\theta\phi} &= 0 \quad \Longrightarrow b = 0, & (140)\\
h_{t\phi} &= -\omega h_{\phi\phi} \quad \Longrightarrow y = 0, & (141)\\
h_{\phi\phi} &= \frac{h_{\theta\theta}}{r^2} e^{2(\psi-\alpha)} \quad \Longrightarrow w = p. & (142)
\end{aligned}$$

Since the components of h_{ab} satisfy all imposed boundary conditions in this gauge, we did not have to construct a gauge vector, although, in principle, this is possible. In choosing our gauge, we required that it reduce to the Regge-Wheeler polar gauge in the non-rotating limit, in which only h_{tt}, h_{rr}, $h_{\theta\theta}$ and $h_{\phi\phi}$ are non-zero, with $h_{\theta\theta}$ and $h_{\phi\phi}$ satisfying the equivalent of (142) in a Schwarzschild metric (see previous section). This converts the (rr) equation into an elliptic equation. As a result of the gauge freedom, only six (out of originally ten) equations need to be solved. These correspond to the indices (tt), (rr), $(\theta\theta)$, (tr), $(t\theta)$ and $(r\phi)$ with unknown functions h, p, k, $\hat{L}$, $\hat{M}$ and $\hat{a}$. Note that in this gauge, condition (142) implies that the perturbation function p does not have to be redefined, as in (135), because it has the desired angular behavior

$$p \sim \sin^m \theta \sum_{l'=0}^{\infty} a_{2l'}(r) P_{2l'}(\cos\theta). \tag{143}$$

In Appendix B we list the necessary components of the perturbation in the Ricci tensor in this gauge.

3.6 Numerical Solution

The task of solving the coupled system of six differential equations is not trivial. In the gauge specified in section 3.5 the (tt) and $(\theta\theta)$ equations are elliptic for h and p respectively. The (rr) equation is parabolic for k (it is missing a $\partial^2 k/\partial r^2$ derivative). The (tr) and $(r\phi)$ equations are second order ordinary differential equations (ODEs) for L and a in the angular direction, while the $(t\theta)$ equation is a second order ODE for M in the radial direction. Each type of equation requires its own finite-difference scheme and boundary conditions. Still, we were able to solve all six equations simultaneously on a 2-dimensional finite grid.

In the radial direction, the grid coincides with that of the equilibrium configuration, i.e. it consists of a number of uniformly spaced grid-points in the coordinate

s, defined in (48), which range from $s = 0$ $(r = 0)$ to $s = 1$ $(r = \infty)$, the equator always being at $s = 0.5$. In the angular direction a different grid is used. Following Ipser & Lindblom (1990), the n angular grid-points are located at the angles $\mu_i = \cos\theta_i$ which correspond to the zero's of the Legendre Polynomial of order $2n-1$: $P_{2n-1}(\mu_i) = 0$. This has a number of advantages. Only a small number of angular grid-points is needed to describe the star, which allows one to solve a smaller linear system of equations. Also, the symmetry axis $(\theta = 0)$ is avoided, so one does not have to expand the equations in this limit. Since the perturbation functions are either symmetric or antisymmetric when reflected in the equatorial plane, one only needs to solve for $0 < \theta \leq \pi/2$, and the boundary conditions at $\theta = \pi/2$ are incorporated in the expressions for the angular derivatives. A drawback of this method is that stars with stiff equations of state $(N < 1.0)$ are less accurately described than stars with soft EOSs $(N > 1.0)$, because the former have discontinuous derivatives of energy density and metric functions across the surface and this results in the appearance of Gibbs phenomena in the angular derivatives.

The above choice of angular grid-points allows us to use high-order formulae for the angular derivatives. In all six equations, all first and second order angular derivatives are approximated as

$$\frac{\partial}{\partial\mu} f^{\pm}(s_i, \mu_j) = \sum_{k=1}^{n} D^{\pm}_{jk} f^{\pm}(s_i, \mu_k), \tag{144}$$

and

$$\frac{\partial^2}{\partial\mu^2} f^{\pm}(s_i, \mu_j) = \sum_{k=1}^{n} H^{\pm}_{jk} f^{\pm}(s_i, \mu_k), \tag{145}$$

where $f^{\pm}$ is a function which is either symmetric $(+)$ or antisymmetric $(-)$ under the transformation $\theta \to \pi - \theta$, i.e. $f^{\pm}(s, -\mu) = \pm f(s, \mu)$. The functions $D^{\pm}_{jk}$ and $H^{\pm}_{jk}$ are derived in Appendix C and are constructed specifically for functions that have the angular behavior

$$f^{+} = \sin^m\theta \sum_{l'=0}^{\infty} a_{2l'} P_{2l'}(\mu), \tag{146}$$

like $h, k, p, \hat{L}$ and $\hat{a}$, and

$$f^- = \sin^m\theta \sum_{l'=0}^{\infty} a_{2l'+1} P_{2l'+1}(\mu), \tag{147}$$

like $\hat{M}$.

In all equations, except for the parabolic equation (rr), the first and second order radial derivatives are approximated by the standard, second order accurate, central difference formulae

$$\frac{\partial}{\partial s} f_{i,j} = \frac{f_{i+1,j} - f_{i-1,j}}{2\Delta s}, \tag{148}$$

and

$$\frac{\partial^2}{\partial s^2} f_{i,j} = \frac{f_{i+1,j} - 2f_{i,j} + f_{i-1,j}}{\Delta s^2}, \tag{149}$$

where Δs is the distance between two radial grid-points. In the parabolic equation (rr), we use an implicit solution scheme; that is, we use a first order accurate, backwards, first radial derivative for k,

$$\frac{\partial}{\partial s} k_{ij} = \frac{f_{i,j} - f_{i-1,j}}{\Delta s}, \tag{150}$$

while for the first order derivatives of other functions involved in the (rr) equation we still use the second order accurate equation (148). Second order radial derivatives in the (rr) equation are not approximated by (149) but by a similar equation using twice the grid-spacing

$$\frac{\partial^2}{\partial s^2} f_{i,j} = \frac{f_{i+2,j} - 2f_{i,j} + f_{i-2,j}}{(2\Delta s)^2}. \tag{151}$$

If one tries to use (149), the solution for k oscillates. That using (151) instead of (149) can suppress such oscillations was discovered in the construction of equilibrium models, where a second order radial derivative appears in the source term of a non-elliptic equation, by Stergioulas & Friedman [36]. Mixed derivatives involved in some of the equations are approximated by

$$\frac{\partial^2}{\partial s \partial \mu} f^{\pm}_{i,j} = \frac{1}{\Delta s} \sum_{k=1}^{n} D^{\pm}_{jk} (f_{i,k} - f_{i-1,k}). \tag{152}$$

At the center and at infinity the appropriate boundary finite difference formulae are used in all equations.

For the two elliptic equations (rr) and $(\theta\theta)$ we require that the solution has vanishing first order angular derivative at $\theta = \pi/2$ and vanishes at infinity. The boundary condition at $\theta = \pi/2$ is built into the construction of the angular derivative formulae. No boundary conditions are needed at the center and on the symmetry axis for the elliptic equations, but the discretized like the exact equations force the solution to vanish there for any mode $m \neq 0$.

For the two second order angular ODE's, (tr) and $(r\phi)$, the boundary conditions at $\theta = \pi/2$ and on the symmetry axis are set by the angular derivative equations (144) and (145). For the second order radial ODE $(t\theta)$ we require that $\hat{M}$ vanishes at the center and at infinity. Finally, for the parabolic equation (rr), boundary conditions at $\theta = \pi/2$ and on the symmetry axis are set by the angular derivative equations (144) and (145), while in the radial direction we set $k = 0$ at the center only (at infinity the boundary is open).

Of the above equations, the most difficult to solve numerically are the (rr) and $(r\phi)$ equations. In the (rr) equation, the solution is propagated from the center to infinity via a first order radial derivative, so it is far more sensitive to local inaccuracies (like those produced by the finite grid-spacing at the surface) than the elliptic equations. In particular, the surface of the rotating star does not correspond to a constant value of the radial coordinate but falls in between grid points. For polytropes of index $N \geq 2$, the energy density goes smoothly enough to zero at the surface that this does not pose any problem even with a grid of only 200 radial points. For polytropes of index $1 \leq N < 2$, however, a small jump in the solution for k appears at the surface. Stiff polytropes of index $N < 1$ have, in addition, discontinuous second order derivatives of the equilibrium metric functions across the surface and a jump in the numerical solution for k is unavoidable when using our grid, since the angular derivative equations were designed only for smooth functions. The small jump appearing in the numerical solution for k does not affect any other perturbation function significantly, except for the function a. Another problem with the (rr) equation - of same origin - is that, for stiff equations of state, the solution oscillates in the vacuum region, unless one makes the approximation

$$\frac{\partial^2 h}{\partial s^2} + 2\frac{\partial^2 p}{\partial s^2} \simeq -\frac{\partial^2 h}{\partial s^2}. \tag{153}$$

The error introduced by making this approximation is negligible, since for all stars that we examined

$$h \simeq -p. \tag{154}$$

Thus, the significant benefit of making this approximation (suppression of all oscillations in the solution) outweighs its mild cost.

Finally, the $(r\phi)$ equation seems to be very sensitive to local inaccuracies, especially at the surface of the star and near its center. The inaccuracies near the center of the star occur, because the perturbation function a depends on the *differences* between other perturbation functions, which all have very small values (compared to their maximum value) near the center. However, the perturbation function a is of lesser importance compared to the other five functions, when computing the critical angular velocities. In fact, we determined that a only minimally affects the other five perturbation functions, so that setting it equal to zero, results in almost unchanged solutions for the other perturbation functions and unchanged critical angular velocities for even the most relativistic stars of the stiffest polytropic index ($N = 1.0$) we examined.

We also determined that the other two off-diagonal perturbation functions $\hat{L}$ and $\hat{M}$ are weakly coupled to the diagonal ones. This is expected, since in our gauge the perturbed metric reduces to a diagonal form in the non-rotating limit and $h_{t\phi}$ is the dominant off-diagonal perturbation ($g_{t\phi}$ is the only non-vanishing off-diagonal metric element for a rotating star). We emphasize that all the above statements hold for perturbations that reduce to polar perturbations in the non-rotating limit.

The finite-differencing of the system of perturbed field equations yields a large linear system. The unknowns are ordered in a way that casts the matrix of the linear system in a band-diagonal form. A direct solution method (LU-decomposition) is employed. Alternatively, we also use an iterative Bi-Conjugate Gradient method with an incomplete LU-decomposition as a preconditioner. The direct solution was faster but required a larger amount of random access memory.[1]

A representative solution of the coupled system of six perturbation equations, for a specific trial function δU, is shown in Figs. (18) - (20). The background star is a rapidly rotating, N=1.5 polytrope with dimensionless central energy density

[1]The subroutines for the solution of the linear system we used, are part of the Portable Extensible Toolkit for Scientific Computation (PETSc) package developed at Argonne National Laboratory [66].

$\bar{\epsilon}_c = 0.061$ and dimensionless angular velocity $\bar{\Omega} = 0.092$. The solution was obtained for the $l = m = 3$ mode using a trial function

$$\delta U = r^l P_l^m(\mu), \tag{155}$$

where $P_l^m(\mu)$ is the associated Legendre function. This trial function is the dominant term in the true eigenfunction of the $l = m$ modes (see section 3.8). All six equations were solved on the same 101×7 (radial $\times$ angular) grid. The perturbation functions h, p, k, $\hat{L}$, $\hat{M}$ and $\hat{a}$ are shown along all seven angular spokes and at the pole (where they vanish). With the exception of $\hat{M}$, the perturbation functions are symmetric under reflection in the equatorial plane and their maximum value occurs for $\theta = \pi/2$. The perturbation function $\hat{M}$ is antisymmetric under reflection, so it vanishes at $\theta = \pi/2$. Its maximum value occurs about half-way between the pole and the equator. The diagonal perturbation functions h, p and k have no nodes inside the star. This is a characteristic of h_{tt} for fundamental $l = m$ modes in the Newtonian limit. The perturbation function k (the solution to the parabolic (rr) equation) exhibits a small jump at the surface, as was explained earlier. In addition, near the surface, the solution can have a wave-like character. This is normal and arises because the solution is obtained for a trial function δU and *not* for the true eigenfunction (in which case this feature should be absent). The off-diagonal functions $\hat{L}$, $\hat{M}$ and $\hat{a}$ vanish much faster in the vacuum surrounding the star than the diagonal functions do; they become negligible almost immediately outside the surface of the star. The function $\hat{L}$ does not have any node inside the star, but $\hat{M}$ and $\hat{a}$ do. Although not necessary, it is reasonable to expect that, for the true eigenfunction δU, $\hat{M}$ and $\hat{a}$ will also not have any nodes inside the star, but their behavior will be similar to the other four perturbation functions. Finally, the solution for the function $\hat{a}$ exhibits some oscillations at the surface of the star, which are induced by the behavior of the function k there. Regarding other polytropic indices and modes, the perturbation functions remain similar to those in Figs. (18) - (20). For stiffer polytropes and for more relativistic stars, the solutions are peaked closer to the surface than for softer polytropes and less relativistic stars. For larger m, the solutions are more narrowly peaked about their maximum value because the dominant radial behavior of δU is r^l. For $N = 1.0$ polytropes the oscillations at the surface are larger than for $N = 1.5$ polytropes, while for $N = 2.0$ polytropes they are negligible. Otherwise, the solutions for the perturbation functions are very similar to those in Figs. (18) - (20).

3.7 A Truncated Gauge

In the Newtonian limit, the important component of the perturbation h_{ab} is h_{tt}, which reduces to $-2h$. In addition, the metric functions h, k, p and w satisfy the relation

$$h = -k = -p = -w. \tag{156}$$

For energy densities typical in neutron stars, the h_{tt} component still dominates h_{ab}. We determined numerically, that even for the most relativistic and rapidly rotating $N = 1.0$ polytrope, the relation (156) still holds approximately in our gauge. This led us to investigate whether by making certain approximations, one can still obtain accurate values for the critical angular velocities of neutral modes, while solving fewer than six equations. Indeed, we find that by making the approximations

$$\frac{h_{tt}}{g_{tt} + 2\omega g_{t\phi}} = \frac{h_{rr}}{g_{rr}} = \frac{h_{\theta\theta}}{g_{\theta\theta}} \qquad \Longrightarrow \qquad h = -k = -p, \tag{157}$$

and

$$h_{t\theta} = h_{r\phi} = 0 \qquad \Longrightarrow \qquad \hat{M} = \hat{a} = 0, \tag{158}$$

one can obtain very accurate critical angular velocities, while solving only two perturbed field equations. Equation (157) is motivated by (156) and (158) is used since $g_{t\theta} = g_{t\phi} = 0$ for the equilibrium configuration and because $h_{t\theta}$, $h_{r\phi}$ vanish in the spherical limit in the Regge-Wheeler polar gauge , i.e. they are proportional to the background metric function ω. In this *truncated gauge*, the perturbation in the metric tensor, can be written in the form

$$h_{ij} = \begin{pmatrix} -2h(e^{2\nu} - \omega^2 e^{2\psi}) & L & 0 & -2\omega h e^{2\psi} \\ & -2he^{2\alpha} & 0 & 0 \\ \text{sym.} & & -2hr^2e^{2\alpha} & 0 \\ & & & -2he^{2\psi} \end{pmatrix}. \tag{159}$$

Only two perturbation functions are nonzero, h and $\hat{L}$, which are determined by solving the (tt) and (tr) equations.

Table 2 shows a comparison of critical configurations obtained in the full and truncated gauges. The equilibrium star is a $N = 1.0$ polytrope with $\bar{\epsilon}_c = 0.3$, which is close to the central energy density of the maximum mass configuration. The critical configurations for the $l = m = 3$, 4 and 5 modes are computed in both gauges on the same 101×7 grid. We compare the dimensionless critical angular velocity and the critical ratio of rotational to gravitational binding energy $T/|W|_c$ in the two gauges. The critical values of $T/|W|$ differ by less than 1% and the critical angular velocities by less than 0.5% when computed in the truncated gauge compared to computing them in the full gauge. The advantage of using the truncated gauge is that far less memory is needed by the numerical code. While six equations can be solved in a reasonable time with a maximum 201×12 grid on a DEC Alpha with 256 MBytes of memory, two equations can be solved with a much finer grid of 801×12 or more points. The execution speed in not limited by the processor speed (the matrix inversion is very fast) but by the available random access memory. For very soft polytropes of index $N \geq 2.0$, a 201×12 grid gives sufficiently accurate critical angular velocities, so that one can use the full gauge for these models. But, for polytropes of $N \leq 1.0$ a 201×12 grid determines the critical angular velocity with an error that can exceed several percent or more. This was determined by comparing critical configurations for Newtonian polytropes, obtained with our code, to published results. Thus, for realistic neutron stars, it is necessary to obtain the critical angular velocities with a grid of at least 801×12 points and this could be achieved only in the truncated gauge. For this reason, all our results shown in this chapter were obtained in the truncated gauge with a grid of (801×12) points, unless otherwise stated.

3.8 The Perturbed Energy Conservation Equation

In preceding sections it was shown how a solution of the perturbed field equations is obtained for a given trial function δU. The complete description of the neutral modes requires the satisfaction of both the perturbed field equations (54) and the perturbed energy conservation equation (92) by the perturbation in the metric h_{ab}

and the scalar function δU. This system of equations (54) and (92) has a zero-frequency solution only for the stars for which a zero-frequency mode exists. For other stars, the system of (54) and (92) does not have a solution $(h_{ab}, \delta U)$ of zero frequency satisfying the imposed boundary conditions. One can, however, solve only the perturbed field equations (54) for trial functions δU and use the perturbed energy conservation equation (92) to construct a criterion for locating the marginally stable star (for a given mode) in a sequence of rotating stars.

The perturbed field equations (54) are implicitly linear in the function δU and so is the perturbed energy conservation equation (92). Hence (92) can be represented as a linear operator L acting on a function δU

$$L(\delta U) = 0. \tag{160}$$

Equation (160) represents an eigenvalue problem for the linear operator L with zero eigenvalue and eigenfunction δU.

In the Newtonian limit, it was shown that the eigenfunction δU of an $l = m$ neutral mode can be approximated accurately by expanding it in terms of a set of basis functions δU_i

$$\delta U = \sum_i a_i \delta U_i, \tag{161}$$

and an appropriate set for this problem [52, 67] is

$$\delta U_i = \delta U_i^{(jk)} = r^{l+2(j+k)} Y^m_{l+2k}(\cos\theta), \tag{162}$$

with $j, k = 0, 1, ...$ and with each set of indices (j, k) yielding a particular δU_i. In practice only a few of these basis functions are sufficient to represent the true eigenfunction δU with reasonable accuracy and the $(0, 0)$ term $r^l Y_l^m$ dominates the expansion (162). Substituting the expansion (161) in (160) yields

$$\sum_i a_i L(\delta U_i) = 0. \tag{163}$$

If we define the inner product[2]

[2]The motivation for defining the inner product as in (164) will become apparent in Appendix D.

$$< \delta U_j|L|\delta U_i >= \int i\frac{\delta U_j}{\sigma\gamma}L(\delta U_i)\sqrt{-g}d^3x, \qquad (164)$$

where g is the determinant of the equilibrium metric tensor, then taking the inner product of (163) with respect to δU_j yields

$$\sum_i a_i < \delta U_j|L|\delta U_i >= 0. \qquad (165)$$

Although the basis functions are not orthogonal to each other, non-zero $< \delta U_j|\delta U_i >$ terms do not appear on the r.h.s. of (165) because we require that the eigensystem has zero eigenvalue. The last equation is a linear, homogeneous system for the coefficients a_i. The system has a non-trivial solution only if its determinant vanishes. This yields a criterion for locating the zero-frequency modes

Criterion *A stationary, axisymmetric star has a nonaxisymmetric, zero-frequency mode with angular dependence $e^{im\phi}$, if*

$$\det < \delta U_j|L|\delta U_i >= 0. \qquad (166)$$

In practice, we start with a slowly rotating star and compute the matrix elements $< \delta U_j|L|\delta U_i >$. For slowly rotating stars the determinant in (166) always has a large value. Keeping the central energy density constant, we look at stars of increasing angular velocity, until the determinant goes through zero. The star for which (166) is satisfied is the one for which the particular $l = m$ mode has a zero-frequency solution and the nonaxisymmetric instability sets in through that mode. In this method, the accuracy in locating the neutral modes depends on how well the expansion (161) approximates the true eigenfunction δU.

In Appendix D, we obtain an expression for $< \delta U_j|L|\delta U_i >$ in terms of Eulerian quantities that is used in the numerical computations. In Appendix D, it is also shown that the above method of solving the perturbed energy conservation equation nearly coincides with a variational principle, because the matrix $< \delta U_j|L|\delta U_i >$ is nearly symmetric for central energy densities typical in neutron stars.

3.9 Critical configurations

Following the method developed in previous sections, we computed the neutral mode (critical) configurations for the fundamental $l = m = 2$, 3, 4 and 5 nonaxisymmetric modes. Three equations of state were examined, having polytropic indices $N = 1.0$, 1.5 and 2.0 polytropes. The $N = 1.0$ polytropes include models with mass and radius similar to those of realistic neutron stars. The other two equations of state were examined for completeness and for comparison with published results in the Newtonian limit. The critical configurations were computed in the truncated gauge with a fine grid of up to 801×12 (radial $\times$ angular) grid points. The trial function δU was expanded as in (162) using different number of terms. Eight basis functions, corresponding to the indices $j = 0, ..., 3$ and $k = 0, 1$ in (162) were sufficient to determine the critical configurations with good accuracy, especially for the $N =$ 1.5 and $N = 2.0$ polytropes, where the error consistently decreases with increasing number of basis functions and increasing number of grid points. This was not so for the $N = 1.0$ polytropes. Owing to the finite grid-size, the surface of the star is discontinuous, and this gives rise to Gibbs phenomena at the surface when using the expansions (144), (145) for the angular derivatives. As a result, increasing the number of grid-points did not monotonically decrease the error. This behavior is expected for our choice of coordinates and grid. It is the price one has to pay for being able to solve a smaller than otherwise linear system of equations. A similar behavior is reported in Bonazzola *et al.* [69], who use a similar angular grid in computing the neutral, viscous bar mode in relativistic stars. Still, by computing the $N = 1.0$ configurations with various grid sizes and various numbers of basis functions, we could obtain sufficiently accurate results.

Our code was checked in the Newtonian limit by comparing the critical configurations for the $l = m = 3$, 4 and 5 modes for $N = 1.0$, 1.5 and 2.0 polytropes to results published by Managan [51], Imamura, Friedman & Durisen [50] and Ipser & Lindblom [52]. As can be seen in Table 3 we are in very good agreement with all published Newtonian results, the exception being $T/|W|_c$ for the $m = 5$ mode in $N = 1.0$ polytropes, which differs by 2 % from the value published in Ipser & Lindblom [52], from which Imamura, Friedman & Durisen [50] differ by 3 % (in the opposite direction). This highlights the increased inaccuracy involved in computing neutral modes for $N \leq 1.0$ polytropes.

For relativistic polytropes we obtain the following results: Figure 23 shows the ratio of the critical angular velocity Ω_c to the *Keplerian angular velocity* Ω_K *at same central energy density* as a function of central energy density for the four modes examined. The lowest central energy density in the figure corresponds to a mildly relativistic star. The highest central energy density shown is the central energy density of the most massive (and thus most relativistic) star allowed by the particular equation of state. The filled circles on the left vertical axes represent the values of Ω_c/Ω_K in the Newtonian limit. As the central energy density increases and the star becomes more relativistic, Ω_c/Ω_K decreases and it decreases at a faster rate as it approaches the most relativistic configuration. Contrary to the Newtonian limit, where $N = 1.0$ polytropes do not have an unstable $m = 2$ mode, we find that in relativistic $N = 1.0$ polytropes the $m = 2$ mode becomes unstable when the central energy density exceeds roughly one 10th the central energy density of the most massive star. At the most relativistic configuration, the $m = 2$ mode becomes unstable for $T/|W|_c$=0.065 or $\Omega_c/\Omega_K = 0.91$. Table 5 compares the most relativistic critical configurations to their counterparts in the Newtonian limit. The value of Ω_c/Ω_K decreases by roughly 15% for the $m = 3$, 4 and 5 modes. Figure (22) shows the critical ratio $T/|W|_c$ for the same $N = 1.0$ polytropes. This ratio decreases faster and by a larger percentage than Ω_c/Ω_K, owing to the fact that the Keplerian value $T/|W|_K$ also decreases as one samples more relativistic stars. In Table 4 it is shown that for the most relativistic $N = 1.0$ polytrope the critical ratio $T/|W|_c$ is about 40 % smaller, for the $m = 3$, 4 and 5 modes, than the corresponding ratio in the Newtonian limit. When the decrease in the Keplerian value $T/|W|_K$ is taken into account and one looks at the ratio $(T/|W|_c)/(T/|W|_K)$ the most relativistic values are still $25 - 30\%$ lower than the Newtonian values.

Figures (23) and (24) and Table 5 display the critical configurations for $N = 1.5$ polytropes. These polytropes are softer than the ones with index $N = 1.0$. Consequently, they have a smaller maximum mass and are less relativistic. For this reason, relativity has a smaller effect on the onset of the nonaxisymmetric instability. The $m = 2$ mode does not become unstable even for the most relativistic $N = 1.5$ polytropes. For the $m = 3$, 4 and 5 modes, the value of Ω_c/Ω_K decreases by $7 - 10\%$ for the most relativistic models compared to the Newtonian limit. The corresponding decrease for $T/|W|_c$ is $30-35\%$ and for $(T/|W|_c)/(T/|W|_K)$ it is $13-19\%$.

Plots of Ω_c/Ω_K and $T/|W|_c$ for the $N = 2.0$ polytropes are shown in figures (25) and (26). These are extremely soft models and their maximum mass occurs at nearly Newtonian central energy densities. Again, the $m = 2$ mode does not become unstable. As seen in table 6, for the $m = 3$, 4 and 5 modes the values of Ω_c/Ω_K, $T/|W|_c$ and $(T/|W|_c)/(T/|W|_K)$ are only a few percent less than in the Newtonian limit, for the largest central energy density. Polytropes constructed with $N = 2.0$ do not resemble realistic neutron stars, but are included here for completeness.

Regarding the accuracy of our results, we estimate that the determined critical angular velocities and critical $T/|W|_c$ are accurate to better than 2 % for $N = 1.0$, 1-2 % for $N = 1.5$ and 1 % for $N = 2.0$ polytropes.

3.10 Discussion

We have treated nonaxisymmetric neutral modes in the context of general relativity. We have found a gauge in which six coupled perturbed field equations can be solved simultaneously with good accuracy. Furthermore, we found an approximate gauge, in which the critical configurations for $N \geq 1.0$ polytropes are located with sufficient accuracy, while solving only two independent perturbed field equations. We showed that general relativity has a large effect on the location of nonaxisymmetric neutral modes and forces the nonaxisymmetric instability to set in for smaller rotation rates than Newtonian theory suggests.

The large effect of relativity on the onset of the nonaxisymmetric instability is most striking in the case of the $m = 2$ modes. In the Newtonian context it was shown that uniformly or nearly uniformly rotating neutron stars cannot become unstable to the $m = 2$ mode unless the equation of state is excessively stiff (see e.g. Skinner & Lindblom [67]). For polytropes, the classical result by James [68] restricts the onset of the m=2 instability to polytropes having an adiabatic index larger than $\Gamma_{\rm crit} = 2.237$ (which corresponds to a polytropic index $N_{\rm crit} = 0.808$). We find that, in the context of general relativity, this critical value becomes $\Gamma_{\rm crit} = 1.77$ (polytropic index $N_{\rm crit} = 1.3$).

In the Newtonian limit, the $m = 2$ mode driven by gravitational radiation coincides with the m=2 mode driven by viscosity even for compressible fluids, as was shown by Ipser & Managan [53]. It is interesting that work by Bonazzola *et al.* [69] suggests that in general relativity, the $m = 2$ viscosity-driven mode has a critical adiabatic index only *slightly higher* than James's result. Thus, in general relativity, the viscosity driven and the gravitational radiation driven $m = 2$ modes no longer coincide and the effect of relativity seems to be very different on each of them.

In forthcoming work, we plan to study realistic equations of state and include the effect of viscosity on the onset of the nonaxisymmetric instability.

Table 2: Comparison of critical configurations in the full and truncated gauges

$N = 1.0$ $\bar{\epsilon}_c = 0.3$ 7×101	$T/\|W\|_c$	$\bar{\Omega}_c$
m=3		
Full gauge	4.63e-2	2.82e-1
Truncated gauge	4.59e-2	2.81e-1
m=4		
Full gauge	3.46e-2	2.48e-1
Truncated gauge	3.47e-2	2.48e-1
m=5		
Full gauge	2.83e-2	2.26e-1
Truncated gauge	2.83e-2	2.26e-1

Table 3: Comparison of critical $T/|W|$ in Newtonian limit with other authors

	m=3	m=4	m=5
N=1.0			
Present	7.92e-2	5.79e-2	4.62e-2
Managan [51]	7.94e-2	5.81e-2	—
Imamura *et al.* [50]	8.0e-2	5.8e-2	4.4e-2
Ipser & Lindblom [52]	8.00e-2	5.84e-2	4.53e-2
N=1.5			
Present	5.61e-2	4.33e-2	3.36e-2
Managan [51]	5.6e-2	4.3e-2	—
Imamura *et al.* [50]	5.7e-2	4.3e-2	—
N=2.0			
Present	3.35e-2	2.81e-2	2.28e-2
Managan [51]	3.3e-2	2.8e-2	—

Table 4: Critical configurations for N=1.0 polytropes

	$\bar{\epsilon}_c$	$T/\|W\|_c$	$(T/\|W\|_c)/$ $(T/\|W\|_K)$	$\bar{\Omega}_c$	Ω_c/Ω_K
			m=2		
Relativistic	3.4e-1	6.49e-2	0.777	3.44e-1	0.911
			m=3		
Newtonian	1.0e-8	7.92e-2	0.769	6.69e-5	0.921
Relativistic	3.4e-1	4.55e-2	0.544	2.96e-1	0.783
			m=4		
Newtonian	1.0e-8	5.79e-2	0.562	5.94e-5	0.818
Relativistic	3.4e-1	3.53e-2	0.422	2.64e-1	0.699
			m=5		
Newtonian	1.0e-8	4.62e-2	0.449	5.41e-5	0.745
Relativistic	3.4e-1	2.87e-2	0.343	2.40e-1	0.635

Table 5: Critical configurations for N=1.5 polytropes

	$\bar{\epsilon}_c$	$T/\|W\|_c$	$(T/\|W\|_c)/$ $(T/\|W\|_K)$	$\bar{\Omega}_c$	Ω_c/Ω_K
m=3					
Newtonian	1.0e-7	5.61e-2	0.943	1.62e-4	0.980
Relativistic	6.1e-2	3.82e-2	0.804	1.02e-1	0.917
m=4					
Newtonian	1.0e-7	4.33e-2	0.728	1.47e-4	0.886
Relativistic	6.1e-2	2.79e-2	0.587	8.87e-2	0.800
m=5					
Newtonian	1.0e-7	3.36e-2	0.565	1.32e-4	0.796
Relativistic	6.1e-2	2.34e-2	0.492	8.18e-2	0.738

Table 6: Critical configurations for N=2.0 polytropes

	$\bar{\epsilon}_c$	$T/\lvert W\rvert_c$	$(T/\lvert W\rvert_c)/$ $(T/\lvert W\rvert_K)$	$\bar{\Omega}_c$	Ω_c/Ω_K
			m=3		
Newtonian	1.0e-8	3.35e-2	0.991	3.67e-5	0.997
Relativistic	5.1e-3	2.59e-2	0.951	2.22e-2	0.979
			m=4		
Newtonian	1.0e-8	2.81e-2	0.832	3.42e-5	0.928
Relativistic	5.1e-3	2.10e-2	0.771	2.02e-2	0.895
			m=5		
Newtonian	1.0e-8	2.28e-2	0.676	3.12e-5	0.848
Relativistic	5.1e-3	1.70e-2	0.624	1.84e-2	0.814

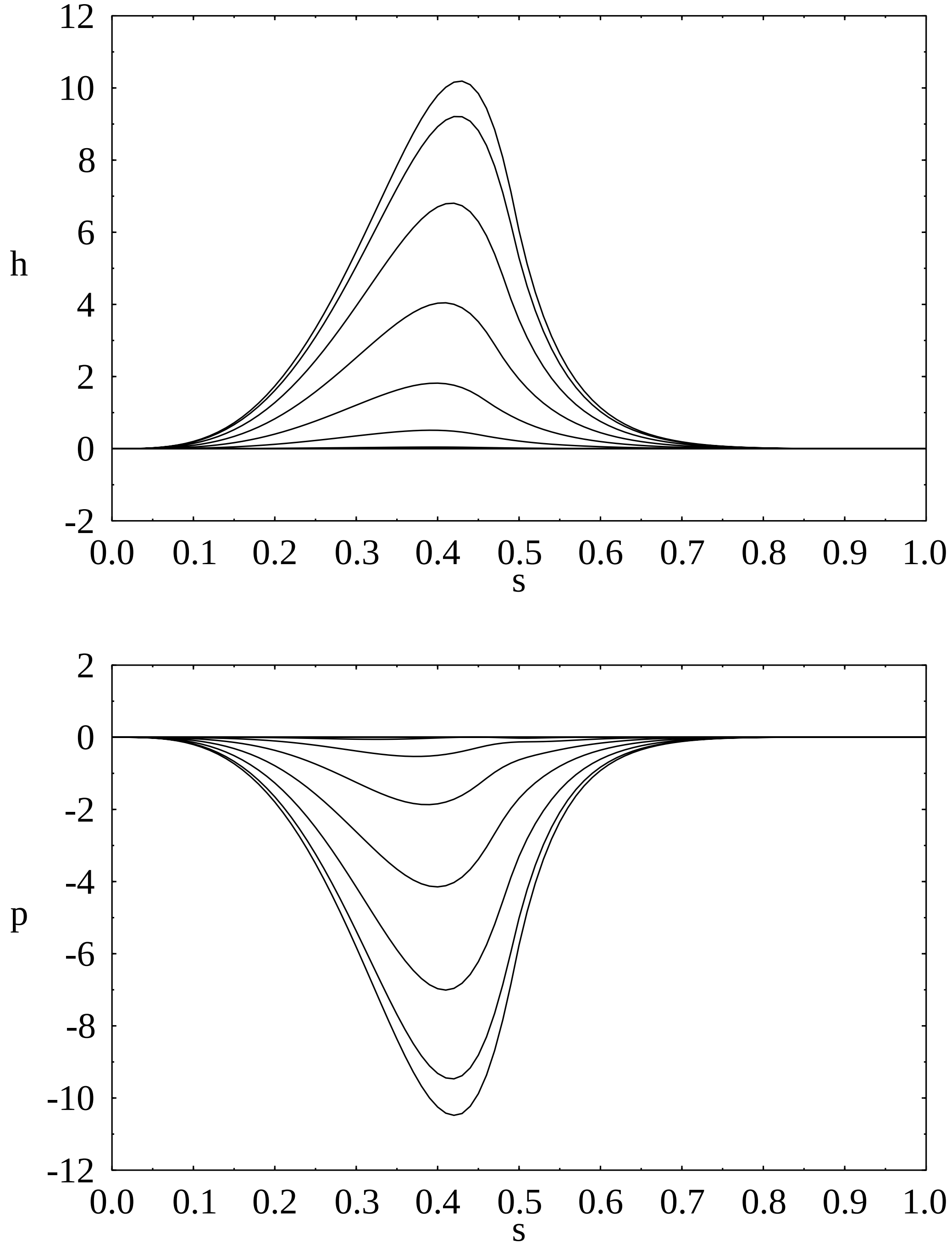

Figure 18: Representative solution for the perturbation functions h and p. Notice that $p \simeq -h$ even for this very relativistic configuration. The scaling of the vertical axis is determined by the trial function δU. The equator of the star is at $s = 0.5$, while $s = 1.0$ corresponds to infinity. The solution in each figure is shown at $\mu \equiv \cos\theta = 0$, 0.23, 0.45, 0.64, 0.80, 0.92, 0.98 and 1.0. The maximum is at $\mu = 0$.

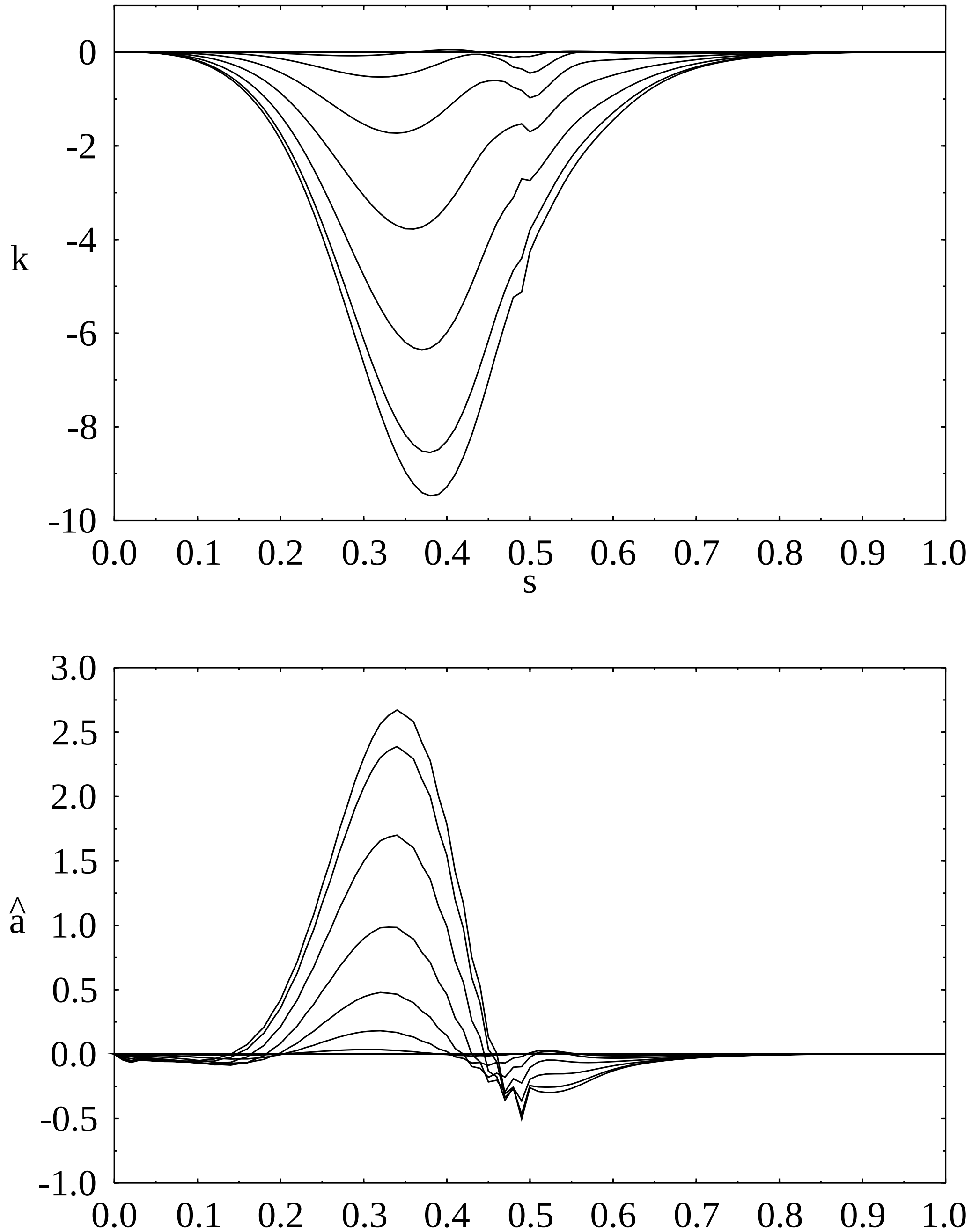

Figure 19: Representative solution for the perturbation functions k and $\hat{a}$. Notice that $k \simeq -h$. The scaling of the vertical axis is determined by the trial function δU. The equator of the star is at $s = 0.5$, while $s = 1.0$ corresponds to infinity. The solution in each figure is shown at $\mu \equiv \cos\theta = 0$, 0.23, 0.45, 0.64, 0.80, 0.92, 0.98 and 1.0. The maximum is at $\mu = 0$.

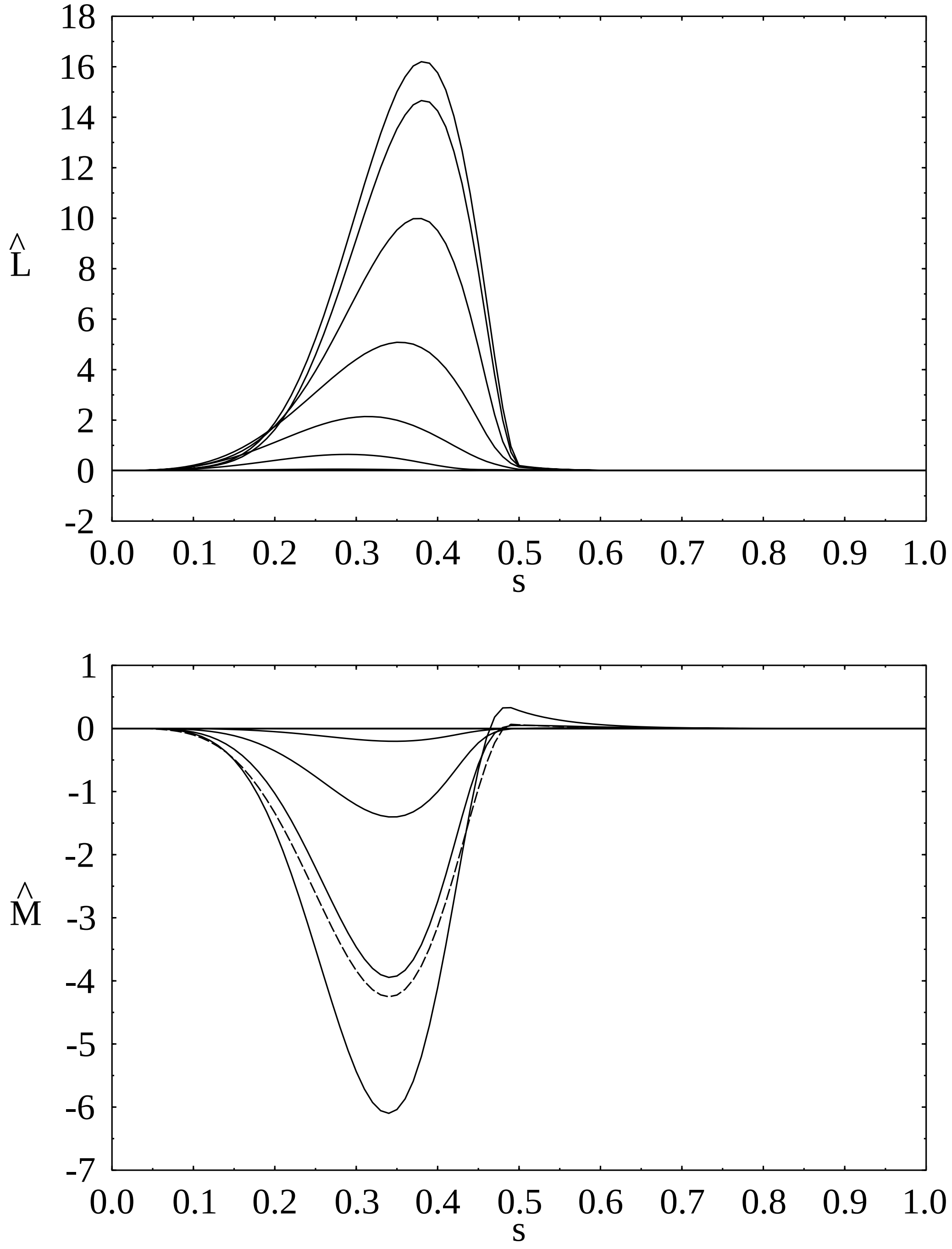

Figure 20: Representative solution for the perturbation functions $\hat{L}$ and $\hat{M}$. The scaling of the vertical axis is determined by the trial function δU. The equator of the star is at $s = 0.5$, while $s = 1.0$ corresponds to infinity. The solution in each figure is shown at $\mu \equiv \cos\theta = 0$, 0.23, 0.45, 0.64, 0.80, 0.92, 0.98 and 1.0. For $\hat{L}$ the maximum is at $\mu = 0$. For $\hat{M}$ the dashed line is at $\mu = 0.23$ and the maximum is at $\mu = 0.45$.

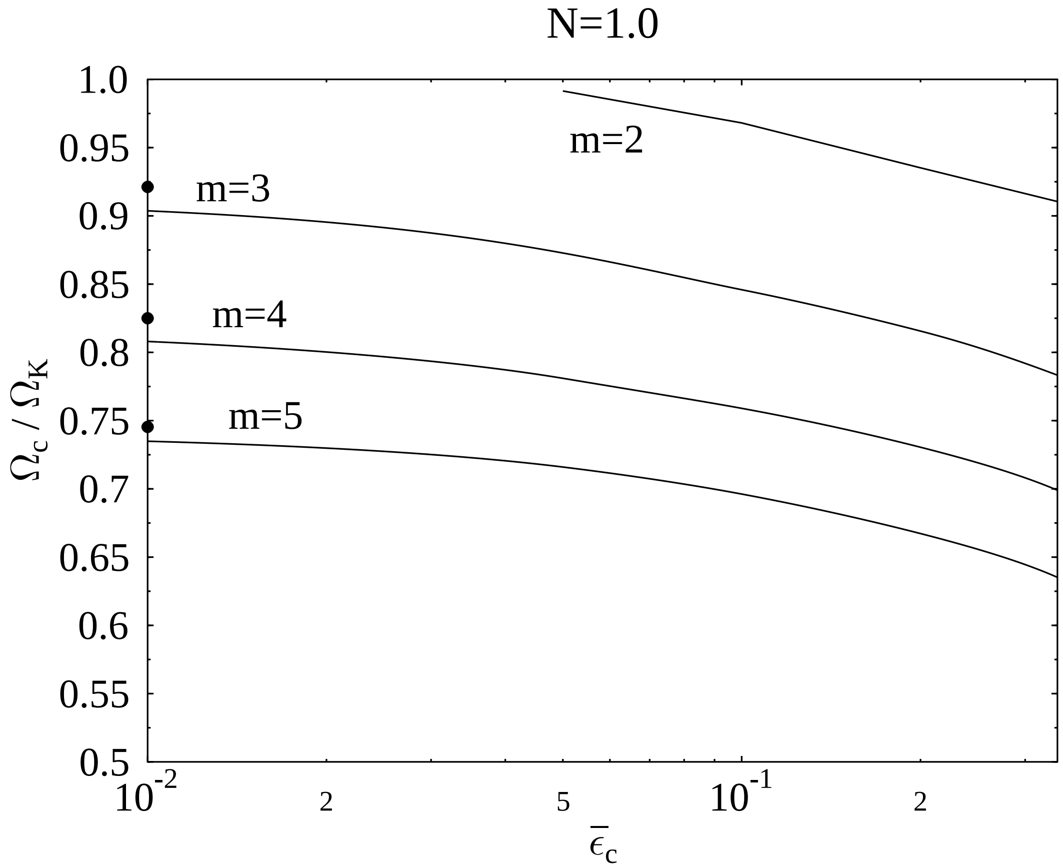

Figure 21: Critical angular velocity over Keplerian angular velocity at same central energy density vs. the dimensionless central energy density $\bar{\epsilon}_c$ for the $m = 2$, 3, 4 and 5 neutral modes of $N = 1.0$ polytropes. The largest value of $\bar{\epsilon}_c$ shown corresponds to the most relativistic stable configurations, while the lowest $\bar{\epsilon}_c$ corresponds to less relativistic configurations. The filled circles on the vertical axis represent the Newtonian limit.

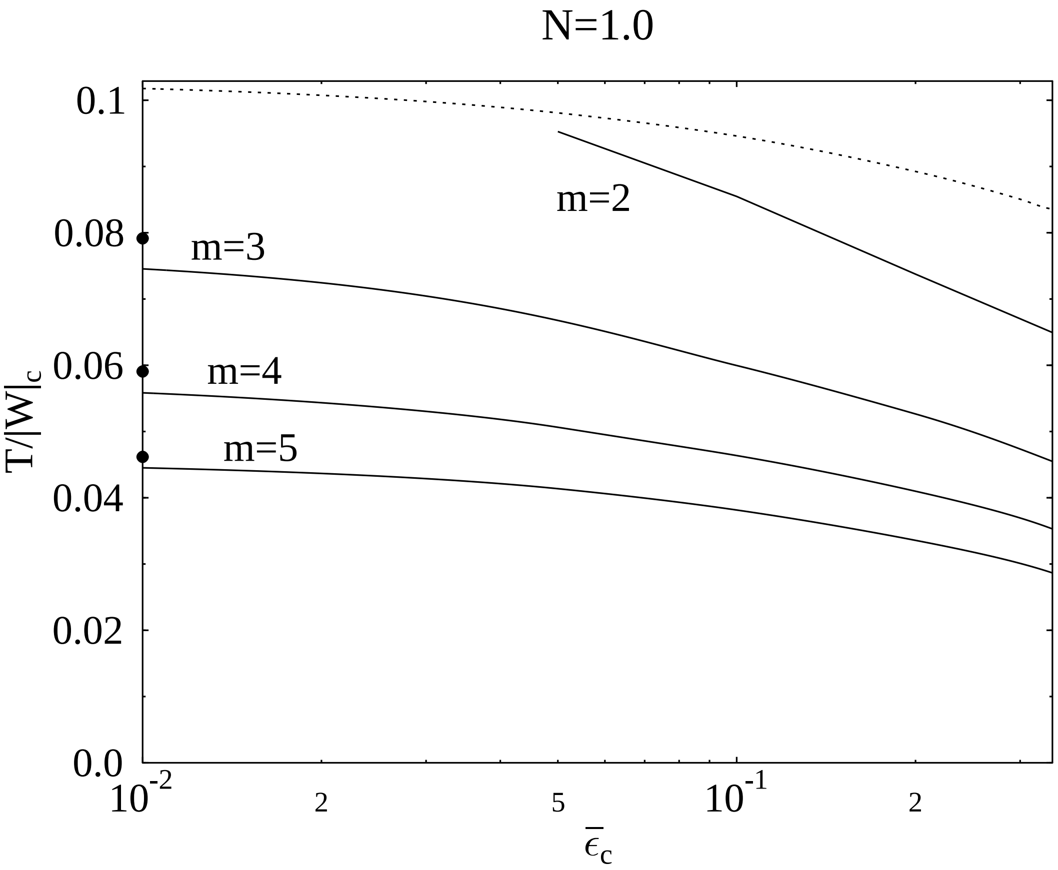

Figure 22: Critical ratio of rotational to gravitational binding energy vs. the dimensionless central energy density $\bar{\epsilon}_c$ for the $m = 2$, 3, 4 and 5 neutral modes of $N = 1.0$ polytropes. The largest value of $\bar{\epsilon}_c$ shown corresponds to the most relativistic stable configurations, while the lowest $\bar{\epsilon}_c$ corresponds to less relativistic configurations. The filled circles on the vertical axis represent the Newtonian limit while the dotted line is the Kepler limit.

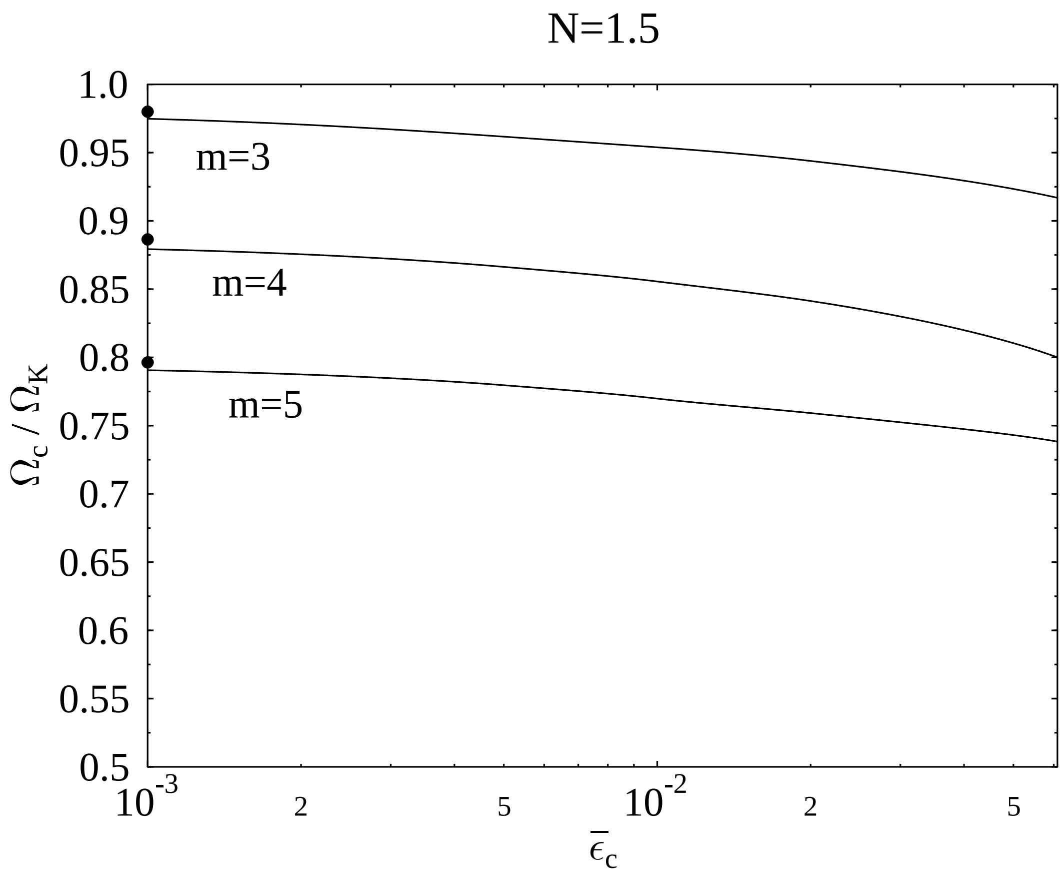

Figure 23: Critical angular velocity over Keplerian angular velocity at same central energy density vs. the dimensionless central energy density $\bar{\epsilon}_c$ for the $m = 3$, 4 and 5 neutral modes of $N = 1.5$ polytropes. The largest value of $\bar{\epsilon}_c$ shown corresponds to the most relativistic stable configurations, while the lowest $\bar{\epsilon}_c$ corresponds to less relativistic configurations. The filled circles on the vertical axis represent the Newtonian limit.

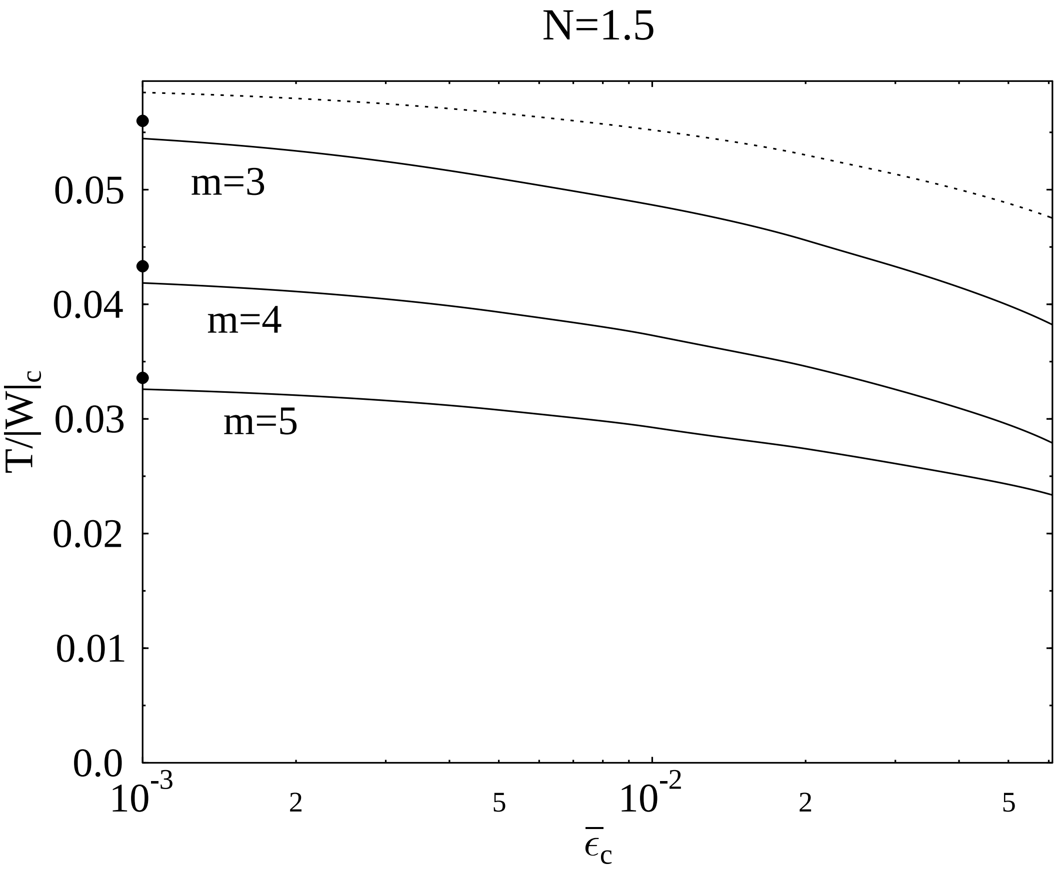

Figure 24: Critical ratio of rotational to gravitational binding energy vs. the dimensionless central energy density $\bar{\epsilon}_c$ for the $m = 3$, 4 and 5 neutral modes of $N = 1.5$ polytropes. The largest value of $\bar{\epsilon}_c$ shown corresponds to the most relativistic stable configurations, while the lowest $\bar{\epsilon}_c$ corresponds to less relativistic configurations. The filled circles on the vertical axis represent the Newtonian limit while the dotted line is the Kepler limit.

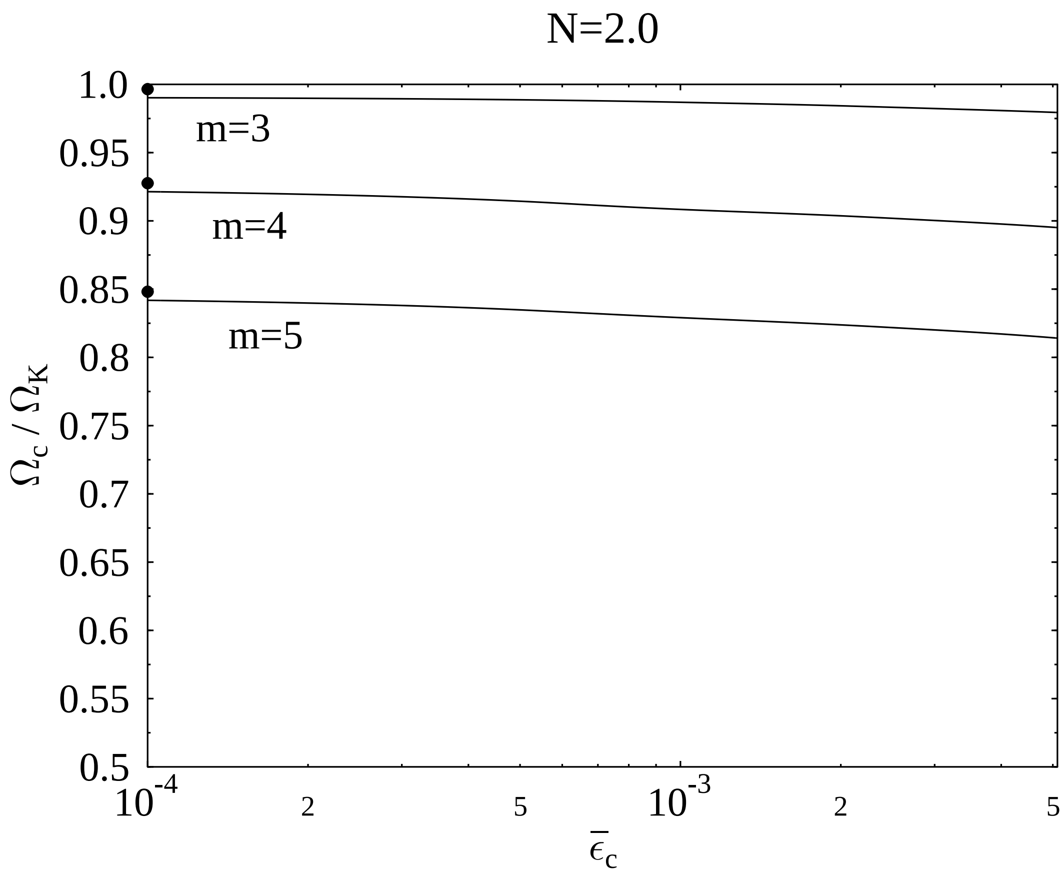

Figure 25: Critical angular velocity over Keplerian angular velocity at same central energy density vs. the dimensionless central energy density $\bar{\epsilon}_c$ for the $m = 3$, 4 and 5 neutral modes of $N = 2.0$ polytropes. The largest value of $\bar{\epsilon}_c$ shown corresponds to the most relativistic stable configurations, while the lowest $\bar{\epsilon}_c$ corresponds to less relativistic configurations. The filled circles on the vertical axis represent the Newtonian limit.

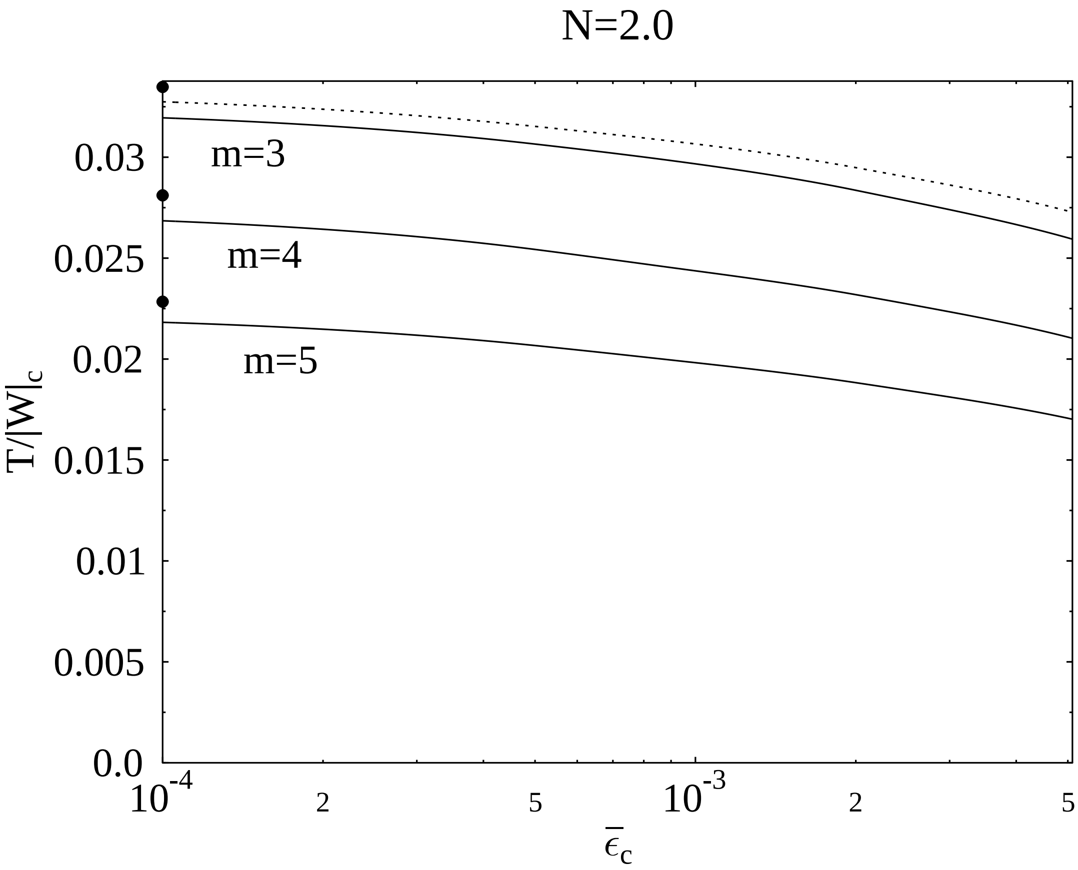

Figure 26: Critical ratio of rotational to gravitational binding energy vs. the dimensionless central energy density $\bar{\epsilon}_c$ for the $m = 3$, 4 and 5 neutral modes of $N = 2.0$ polytropes. The largest value of $\bar{\epsilon}_c$ shown corresponds to the most relativistic stable configurations, while the lowest $\bar{\epsilon}_c$ corresponds to less relativistic configurations. The filled circles on the vertical axis represent the Newtonian limit while the dotted line is the Kepler limit.

Appendix A

Documentation for the Public Domain Code

A.1 Introduction

RNS is a code that constructs models of *rapidly rotating, relativistic stars* using tabulated equations of state which are supplied by the user. The code is written after the KEH method (Komatsu, Eriguchi & Hachisu [7]) and modifications introduced by Cook, Shapiro & Teukolsky [10]. It computes individual models as well as sequences of fixed mass, baryon mass, angular velocity or angular momentum. All models assume uniform rotation. The code was introduced in Stergioulas & Friedman [36].

A.2 Compiling the Code

RNS is written in the ANSI C programming language. Machine specific commands were avoided, so that the C program should compile on any platform using an ANSI C compiler. The source code comes with a Unix `Makefile`. Before running the `Makefile` for the first time, one should check to see if it uses the correct compiler (the default is `cc`) and the correct flags for choosing the ANSI C option (the default is `-std1`), and optimization (default is `-O`) - if not, the `Makefile` should be edited. Once the `Makefile` is correct, run `make` to obtain the executable `rns`. If significant changes to the `Makefile` are needed in order to compile it, they can be sent to the author, in order to be included in future versions.

A.3 Supplying the Equation of State

RNS needs a tabulated, zero-temperature equation of state (EOS), as an input, in order to run. The EOS file is required to have the following format: The first line in the EOS file should contain the number of tabulated points. The remaining lines should consist of four columns - energy density (in gr/cm^3), pressure (in dynes/cm^2), enthalpy (in cm^2/s^2), and baryon number density (in cm^{-3}). The *enthalpy* is defined as

$$H(P) = \int_0^P \frac{c^2 dP}{(\epsilon + P)}, \tag{167}$$

where ϵ is the energy density, P is the pressure and c is the speed of light.

The number of tabulated points should be limited to 200. Example files (e.g. `eosC`) are supplied with the source code. The EOS file needs to be specified using the following flag:

`rns -f` *filename*

A.4 Specifying Model Parameters and Other Options

RNS has several options to specify model parameters and choose from different output formats. A model is defined uniquely by specifying two parameters - one will always be the central energy density and the other can be one of the following: mass, baryon mass, angular velocity, angular momentum, or the ratio of the polar coordinate radius to the coordinate equatorial radius (which is usually called the *axes ratio*, see definition of coordinates in (168)).

The parameters are specified using the following flags:

`-e` *central energy density* in gr/cm^3

`-r` *axes ratio*

`-m` *mass* in $M_\odot$

`-z` *baryon mass* in $M_\odot$

`-o` *angular velocity* in $10^4 s^{-1}$

`-j` *angular momentum* in $GM_\odot^2/c$

The code is written so as to directly construct a model when the axes ratio is specified (which is therefore the fastest option). If one specifies a different parameter e.g. mass, the code constructs several (usually more than ten) models by varying the axes ratio, until it finds a model, for which the chosen parameter is within some allowed tolerance of the specified value. The default tolerance is 10^{-4} (relative error) and can be changed by using the flag

`-b` *tolerance*

A smaller tolerance means more models will be constructed.

A model is constructed by iteratively solving the field equations and the hydrostatic equilibrium equation, until the coordinate equatorial radius changes by less than a specified relative accuracy. The default accuracy is 10^{-5} and this can be changed by using the flag

`-a` *accuracy*

Convergence is monitored by printing out the relative difference in the coordinate equatorial radius from one iteration to the next. This print-out can be suppressed by using the flag

`-d` 0

In rare cases, such as for unstable models of very stiff equations of state, the iteration may not, at first, converge. Such cases can easily be fixed by using a relaxation factor in the iteration. A factor of 0.8 usually makes the iteration convergent (the default is 1.0, which amounts to no relaxation). It can be specified using

`-c` *relaxation factor*

Specifying the above parameters is not sufficient to get the code running. One also needs to select the task that is to be performed.

A.5 Tasks

RNS can perform eight different tasks, which are listed below, along with the required options for each task:

`-t model` Computes a model with fixed central energy density ϵ_c and *axes ratio*. Requires `-e` and `-r`

`-t gmass` Computes a model with fixed ϵ_c and *gravitational mass*. Requires `-e` and `-m`

`-t rmass` Computes a model with fixed ϵ_c and *baryon mass*. Requires `-e` and `-z`

`-t omega` Computes a model with fixed ϵ_c and *angular velocity*. Requires `-e` and `-o`

`-t jmoment` Computes a model with fixed ϵ_c and *angular momentum*. Requires `-e` and `-j`

`-t static` Computes the nonrotating model for a given ϵ_c. Requires `-e`.

`-t kepler` Computes the model with Keplerian angular velocity for a given ϵ_c. The default relative accuracy is 10^{-4} and can be changed with `-b` *tolerance*. Requires `-e`.

`-t test` Computes the test model.

To find out if the source code compiled correctly, you can run the test model

```
rns -f eosC -t test
```

and compare the output to the file `test.out`. For specific examples of the above tasks and their output, see the file `examples.test`.

A.6 Sequences

You can obtain a sequence of models with the same two parameters fixed (instead of just one model) by specifying a range of central energy densities and the number of models desired. For example

```
-e 1e15 -l 3e15 -n 10
```

will give a sequence of ten models between the central energy densities of 10^{15}gr/cm^3 and 3×10^{15} gr/cm^3. The models will be equally spaced in $\log \epsilon_c$. This can be done with any of the tasks described in the previous section. However, one needs to make sure that the requested models actually exist. For example, if one wants to compute a sequence of constant baryon mass, one should first compute and examine the nonrotating and Keplerian sequences for a wide range of energy densities and then select a sub-range of ϵ_c for which stars of the given baryon mass exist.

A.7 Output

RNS prints out 17 physical quantities upon successful computation of a model. These are:

ϵ_c *central energy density*

M *gravitational mass*

M_0 *baryon mass*

R_e *circumferential radius at the equator ($2\pi R_e$ is the proper circumference)*

Ω *angular velocity*

Ω_p *angular velocity of a particle in circular orbit at the equator*

$T/|W|$ *rotational/gravitational binding energy*

$cJ/GM_\odot^2$ *dimensionless angular momentum*

I *moment of inertia (except for nonrotating model)*

h_+ *height from surface of last stable co-rotating circular orbit in equatorial plane - if none, then all such orbits are stable*

h_- *height from surface of last stable counter-rotating circular orbit in equatorial plane - if none, then all such orbits are stable*

Z_p *polar redshift*

Z_b *backward equatorial redshift*

Z_f *forward equatorial redshift*

ω_c/Ω *ratio of central value of potential* ω *to* Ω

r_e *coordinate equatorial radius*

r_p/r_e *axes ratio (polar to equatorial)*

The following values for the physical constants are used: $c = 2.9979 \times 10^{10}\mathrm{cm/s}^{-1}$, $G = 6.6732 \times 10^{-8}\mathrm{g}^{-1}\mathrm{cm}^3\mathrm{s}^2$, $m_B = 1.66 \times 10^{-24}\mathrm{gr}$, and $M_\odot = 1.987 \times 10^{33}\mathrm{gr}$. The coordinates of the stationary, axisymmetric spacetime used to model the rotating relativistic star are defined through the metric

$$ds^2 = -e^{\gamma+\rho}\, dt^2 + e^{\gamma-\rho} r^2 \sin^2\theta (d\phi - \omega dt)^2 + e^{2\alpha}(dr^2 + r^2 d\theta^2). \tag{168}$$

where the potentials γ, ρ, α and ω are functions of r and θ only. The matter inside the neutron star is approximated by a perfect fluid.

There are two different printing formats:

`-p 1` is a detailed vertical list of the above quantities (default)

`-p 2` is a compact horizontal print-out of the same quantities, which is useful when computing sequences.

In addition to the above quantities, one can print out the values of the four metric potentials and the pressure at every grid point with

```
-p 3
```

This is a very long print out and should be directed to a file rather than to the screen. The format is:

$s = r/(r + r_e)$ $\quad \cos\theta$ $\quad \rho$ $\quad \gamma$ $\quad \alpha$ $\quad \omega(10^4\mathrm{s}^{-1})$ $\quad$ P $(dynes/cm^2)$

A.8 Numerical Grid

RNS uses a uniform 2-D grid in the variables $s = r/(r+r_e)$ and $\mu = \cos\theta$. The center is at $s = 0$, the equator at $s = 0.5$ and infinity at $s = 1$. In the radial direction, the grid extends from $s = 0$ to $s = 0.9999$. The equatorial plane is at $\mu = 0$ while the pole is at $\mu = 1$. If one uses $SDIV$ points in the s-direction and $MDIV$ points in the μ-direction, then the (s, μ) coordinates of the (i, j) grid point are given by

$$s[i] = 0.9999\Big(\frac{1-i}{SDIV-1}\Big), \tag{169}$$

$$\mu[j] = \Big(\frac{1-j}{MDIV-1}\Big). \tag{170}$$

The default grid size is $SDIV \times MDIV = 129 \times 65$. One can change this by editing the `Makefile`. If one specifies too large a grid size, it is possible to run into a memory segmentation fault. This can be fixed by issuing the command

```
limit stacksize unlimited
```

in a UNIX environment.

A.9 Availability

RNS is available as a public domain program and can be downloaded by anonymous ftp from `alpha2.csd.uwm.edu`, directory `/pub/rns`. The filename is either `rns.`*version*`.tar.Z` or `rns.`*version*`.tar.gz`. A relevant paper (Stergioulas & Friedman [36]) can be found in `/pub/niksterg/papers/paper1.tar.Z`. A WWW page is planned. Suggestions, comments or questions should be sent to

Nikolaos Stergioulas
Department of Physics
University of Wisconsin-Milwaukee
PO Box 413, Milwaukee, WI 53201
E-mail: niksterg@pauli.phys.uwm.edu

Appendix B

Perturbed Ricci Tensor

We list the perturbation in the six components of the Ricci tensor that are used in the perturbed field equations, in the gauge of section 3.5. We follow the notation introduced in section 3.4. In the r.h.s. of each equation, subscripts denote partial derivatives, e.g. $h_{\phi\phi} = \partial^2 h/\partial\phi^2$.

$$
\begin{aligned}
\delta R_{tt} \;=\; & -\omega^2(h_{\phi\phi} + p_{\phi\phi}) + e^{2(\nu-\psi)}h_{\phi\phi} + e^{2(\psi-\nu)}\omega^4 p_{\phi\phi} + e^{2(\nu-\alpha)}\Big\{2\nu_{rr}(h-k) \\
& + 2\nu_r(h_r - k_r) + 2\Big(\nu_r + \frac{1}{r}\Big)\nu_r(h-k) + \frac{2}{r^2}\Big[\nu_{\theta\theta}(h-p) + \nu_\theta(h_\theta - p_\theta) \\
& + \nu_\theta^2(h-p)\Big] + \nu_r\Big[a_\phi + 2\psi_r(h-k) + k_r + 2p_r\Big] + \frac{\nu_\theta}{r^2}\Big[2\psi_\theta(h-p) \\
& + k_\theta + 2p_\theta\Big] + h_{rr} + \frac{h_{\theta\theta}}{r^2} + \Big(\psi_r + \frac{1}{r}\Big)h_r + \frac{\psi_\theta}{r^2}h_\theta\Big\} \\
& + e^{2(\psi-\alpha)}\Big\{-\omega^2\Big(p_{rr} + \frac{p_{\theta\theta}}{r^2}\Big) + \omega\psi_r\Big[2\omega\psi_r(p-k) + \omega a_\phi - \omega(h_r + k_r \\
& + p_r)\Big] - \frac{\omega^2}{r^2}\psi_\theta(h_\theta + k_\theta + p_\theta) + \omega\Big[2\omega_r\psi_r(k-p) + 2\omega\psi_{rr}(k-p) \\
& + 2\omega\psi_r(k_r - p_r)\Big] + 2\omega^2\Big(\nu_r + \frac{1}{r} + 2\psi_r\Big)\psi_r(k-p) - \omega^2\nu_r(2a_\phi + p_r) \\
& - \frac{\omega^2}{r^2}\nu_\theta p_\theta - \frac{\omega^2}{r}p_r\Big\} - \omega^2 e^{2(\psi-\alpha-\nu)}\Big[\psi_r\omega L_\phi + \frac{\psi_\theta}{r^2}\omega M_\phi\Big] \\
& + e^{-2\alpha}\Big\{L_\phi\Big[\omega_r + \omega(2\psi_r - \nu_r)\Big] + \frac{M_\phi}{r^2}\Big[\omega_\theta + \omega(2\psi_\theta - \nu_\theta)\Big]\Big\} \\
& + e^{4\psi-2(\alpha+\nu)}\Big[\omega^3\omega_r a_\phi + \omega^2\omega_r^2(h+k-2p) + \frac{1}{r^2}\omega^2\omega_\theta^2(h-p)\Big]
\end{aligned}
$$

$$
\begin{aligned}
&+ e^{2(\psi-\alpha)}\Big\{(k-p)\Big[\omega_r^2+\omega\omega_r\Big(4\psi_r-2\nu_r+\frac{2}{r}\Big)+2\omega\omega_{rr}\Big]\\
&+\omega_r\omega(h_r+k_r-4p_r)+\frac{\omega_\theta}{r^2}\omega(h_\theta-2p_\theta-k_\theta)\Big\} \qquad (171)
\end{aligned}
$$

$$
\begin{aligned}
\delta R_{rr} \;=\;& \Big(-e^{2(\alpha-\psi)}+\omega^2e^{2(\alpha-\nu)}\Big)k_{\phi\phi}-\frac{k_{\theta\theta}}{r^2}-h_{rr}-2p_{rr}-a_{r\phi}-\frac{k_\theta}{r^2}(\nu_\theta+\psi_\theta)\\
&+k_r\Big(\nu_r+\frac{1}{r}+\psi_r\Big)+\frac{2}{r^2}\Big[\alpha_{\theta\theta}(p-k)+\alpha_\theta(p_\theta-k_\theta)\\
&+\alpha_\theta(\nu_\theta+\psi_\theta)(p-k)\Big]-\frac{\alpha_\theta}{r^2}(h_\theta+2p_\theta-k_\theta)+\alpha_r(h_r+k_r+a_\phi)\\
&-2\psi_r(p_r+a_\phi)-2\nu_rh_r-\frac{2}{r}p_r+\omega e^{-2\nu}\Big(-\frac{\alpha_\theta}{r^2}M_\phi+\alpha_rL_\phi-L_{r\phi}\Big)\\
&+\omega_re^{2(\psi-\nu)}\Big[-\omega a_\phi+\omega_r(p-h)\Big] \qquad (172)
\end{aligned}
$$

$$
\begin{aligned}
\delta R_{\theta\theta} \;=\;& \Big(-e^{2(\alpha-\psi)}+\omega^2e^{2(\alpha-\nu)}\Big)r^2p_{\phi\phi}-r^2p_{rr}-h_{\theta\theta}-k_{\theta\theta}-p_{\theta\theta}-r^2p_r\Big(\nu_r+\frac{1}{r}\\
&+\psi_r\Big)+p_\theta(\nu_\theta+\psi_\theta)+4r(\alpha_r+\frac{1}{r})(k-p)+2r^2\Big(\alpha_{rr}-\frac{1}{r^2}\Big)(k-p)\\
&+2r^2\Big(\alpha_r+\frac{1}{r}\Big)(k_r-p_r)+2\Big(\nu_r-\frac{1}{r}+\psi_r\Big)r^2\Big(\alpha_r+\frac{1}{r}\Big)(k-p)\\
&-r^2\Big(\alpha_r+\frac{1}{r}\Big)(h_r+k_r+a_\phi)+\alpha_\theta(h_\theta+2p_\theta-k_\theta)-2\psi_\theta p_\theta-2\nu_\theta h_\theta\\
&+\omega e^{-2\nu}\Big[-r^2(\alpha_r+\frac{1}{r})L_\phi+\alpha_\theta M_\phi-M_{\theta\phi}\Big]+\omega_\theta^2e^{2(\psi-\nu)}(p-h) \qquad (173)
\end{aligned}
$$

$$
\begin{aligned}
\delta R_{tr} \;=\;& -\frac{\omega}{2}a_{\phi\phi}+\omega(h_{r\phi}-p_{r\phi})+\omega(2p_\phi+h_\phi-k_\phi)(\nu_r-\psi_r)+\frac{\omega^3}{2}e^{2(\psi-\nu)}a_{\phi\phi}\\
&+\frac{1}{2}e^{2(\psi-\alpha)}\Big\{-2a\omega\psi_r(\nu_r+\frac{1}{r}+\psi_r)+\frac{\omega}{r^2}\psi_\theta(-3a_\theta-2a\psi_\theta-2a\nu_\theta)\\
&+\frac{\omega}{r^2}(2\alpha_\theta-\nu_\theta)a_\theta-\frac{\omega}{r^2}a_{\theta\theta}-2a\omega\Big(\omega_{rr}+\frac{\omega_{\theta\theta}}{r^2}\Big)\Big\}+\frac{1}{2}(-e^{-2\psi}+\omega^2e^{-2\nu})L_{\phi\phi}\\
&+\frac{\omega_r}{2}(k_\phi-h_\phi-2p_\phi)-\frac{1}{2}a\omega e^{4\psi-2(\alpha+\nu)}\Big(\omega_r^2+\frac{\omega_\theta^2}{r^2}\Big)+\frac{\omega^2}{2}\omega_re^{2(\psi-\nu)}(h_\phi+k_\phi\\
&-4p_\phi)+\frac{1}{2}e^{2(\psi-\alpha)}\Big\{a\omega_r\Big(\nu_r-3\psi_r-\frac{1}{r}\Big)+\frac{a}{r^2}\omega_\theta(\nu_\theta-3\psi_\theta)-a\Big(\omega_{rr}+\frac{\omega_{\theta\theta}}{r^2}\Big)\\
&-\frac{\omega_\theta}{r^2}a_\theta\Big\}+\frac{1}{2}e^{2(\psi-\alpha-\nu)}\Big\{\omega\omega_r\Big[L\Big(3\psi_r-\nu_r+\frac{1}{r}\Big)+\frac{M}{r^2}(3\psi_\theta-2\alpha_\theta-\nu_\theta)
\end{aligned}
$$

$$
\begin{aligned}
&+\frac{M_\theta}{r^2}\Big]+\frac{\omega}{r^2}\omega_\theta(2L\alpha_\theta-L_\theta)+\frac{\omega_r}{r^2}\omega_\theta M+\omega_r^2 L+\frac{1}{r^2}\omega\omega_{r\theta}M+\omega\omega_{rr}L\Big\}\\
&+e^{-2\alpha}\Big\{-L\Big(\frac{2}{r^2}\alpha_\theta\nu_\theta+\frac{1}{r}\nu_r+\nu_r^2+\nu_r\psi_r+\nu_{rr}\Big)+\frac{M}{r^2}(2\alpha_\theta\nu_r-\nu_r\nu_\theta\\
&-\nu_r\psi_\theta-\nu_{r\theta})+\frac{M_r}{r^2}\Big(\frac{\psi_\theta}{2}+\frac{\nu_\theta}{2}-\alpha_\theta\Big)+\frac{L_\theta}{r^2}\Big(-\frac{\psi_\theta}{2}+\frac{\nu_\theta}{2}+\alpha_\theta\Big)-\frac{\nu_r}{r^2}M_\theta\\
&-\frac{L_{\theta\theta}}{2r^2}+\frac{M_{r\theta}}{2r^2}\Big\} \qquad (174)
\end{aligned}
$$

$$
\begin{aligned}
\delta R_{t\theta} \;=\;& \omega(h_{\theta\phi}-p_{\theta\phi})+(\nu_\theta-\psi_\theta)\omega(k_\phi+h_\phi)+\frac{1}{2}e^{2(\psi-\alpha)}\Big[3\omega\psi_r a_\theta-\omega\Big(2\alpha_r+\frac{1}{r}\\
&-\nu_r\Big)a_\theta+\omega a_{r\theta}\Big]+\frac{1}{2}\Big(-e^{-2\psi}+\omega^2e^{-2\nu}\Big)M_{\phi\phi}-\frac{\omega_\theta}{2}(h_\phi+k_\phi)\\
&+\frac{\omega^2}{2}\omega_\theta e^{2(\psi-\nu)}(h_\phi-2p_\phi-k_\phi)+\frac{1}{2}e^{2(\psi-\alpha)}\omega_r a_\theta\\
&+\frac{1}{2}e^{2(\psi-\alpha-\nu)}\Big\{\omega\omega_\theta\Big[L(3\psi_r-2\alpha_r-\nu_r-\frac{1}{r})+\frac{M}{r^2}(3\psi_\theta-\nu_\theta)+L_r\Big]\\
&+\omega\omega_r\Big[2M\Big(\alpha_r+\frac{1}{r}\Big)-M_r\Big]+L\omega_r\omega_\theta+L\omega\omega_{r\theta}+\frac{M}{r^2}(\omega_\theta^2+\omega\omega_{\theta\theta})\Big\}\\
&+e^{-2\alpha}\Big\{-\frac{M}{r^2}\Big[2r^2\nu_r\Big(\alpha_r+\frac{1}{r}\Big)+\nu_\theta^2+\nu_\theta\psi_\theta+\nu_{\theta\theta}\Big]+L\Big[\Big(2\alpha_r+\frac{1}{r}\Big)\nu_\theta\\
&-\nu_r\nu_\theta-\nu_\theta\psi_r-\nu_{r\theta}\Big]+\Big(\frac{\psi_r}{2}+\frac{\nu_r}{2}-\alpha_r+\frac{1}{2r}\Big)(L_\theta-M_r)-L_r\nu_\theta\\
&+\frac{L_{r\theta}}{2}-\frac{M_{rr}}{2}\Big\} \qquad (175)
\end{aligned}
$$

$$
\begin{aligned}
\delta R_{r\phi} \;=\;& -h_{r\phi}-p_{r\phi}+\psi_r(h_\phi+p_\phi)+\nu_r(k_\phi-h_\phi)+\Big(\alpha_r+\frac{1}{r}\Big)(k_\phi-p_\phi)\\
&-\frac{1}{2}e^{2(\psi-\nu)}\omega^2a_{\phi\phi}+e^{2(\psi-\alpha)}\Big\{\frac{1}{2r^2}\Big[2a_\theta\psi_\theta+2a\psi_{\theta\theta}+a_{\theta\theta}+\nu_\theta(2a\psi_\theta+a_\theta)\Big]\\
&+a\psi_{rr}-\frac{\alpha_\theta}{r^2}a_\theta+a\psi_r\Big(\nu_r+\frac{1}{r}+\psi_r\Big)+\frac{\psi_\theta}{2r^2}(2a\psi_\theta+a_\theta)\Big\}-\frac{\omega}{2}e^{-2\nu}L_{\phi\phi}\\
&+\frac{a}{2}e^{4\psi-2(\alpha+\nu)}\Big(\omega_r^2+\frac{\omega_\theta^2}{r^2}\Big)+\frac{\omega}{2}\omega_r e^{2(\psi-\nu)}(4p_\phi-k_\phi-h_\phi)\\
&+\frac{1}{2}e^{2(\psi-\alpha-\nu)}\Big\{\frac{\omega_r}{2}(2\alpha_\theta+\nu_\theta-3\psi_\theta)M-\frac{2}{r^2}\omega_\theta\alpha_\theta L+L\omega_r\Big(\nu_r-3\psi_r-\frac{1}{r}\Big)\\
&+\frac{1}{r^2}(L_\theta\omega_\theta-M_\theta\omega_r)-L\omega_{rr}-\frac{\omega_{r\theta}}{r^2}M\Big\} \qquad (176)
\end{aligned}
$$

Appendix C

Angular Derivative Formulae

In this appendix we derive high-order, finite-difference formulae that approximate the angular derivatives of functions that are known at the discrete set of angles $\mu_i = \cos\theta_i$ (with $i = 1...n$), which correspond to the zero's of the Legendre polynomial $P_{2n-1}(\mu_i) = 0$. A function $f(r,\mu)e^{im\phi}$ can be expanded in terms of associated Legendre polynomials as

$$f(r,\mu) = \sum_{k=0}^{\infty} f_k(r) P^m_{k+|m|}(\mu), \tag{177}$$

Since $P^m_{k+|m|}$ is a polynomial of order k multiplied by $(1-\mu^2)^{|m|/2}$, expansion (177) is equivalent to

$$f(r,\mu) = (1-\mu^2)^{|m|/2} \sum_{k=0}^{\infty} f_k^\dagger(r) P_k(\mu), \tag{178}$$

where $P_k(\mu)$ is the Legendre polynomial of order k. By orthogonality of the Legendre polynomials, the coefficients $f_k^\dagger(r)$ in the expansion (178) are determined as

$$f_k^\dagger(r) = \left(k + \frac{1}{2}\right) \int_{-1}^{1} f(r,\mu)(1-\mu^2)^{-|m|/2} P_k(\mu) d\mu. \tag{179}$$

The integral in (179) can be computed with high accuracy using Gaussian quadrature

$$\int_{-1}^{1} g^+(r,\mu) d\mu \simeq \sum_{i=1}^{n} w_i g^+(r,\mu_i), \tag{180}$$

where $g^+(r,\mu)$ is a function symmetric in μ and w_i are weights that are tabulated in e.g. Abramowitz & Stegun [70]. For a function $g^-(r,\mu)$, antisymmetric in μ, the integral in (180) vanishes.

We are interested in functions $f(r,\mu)$ that have definite reflection symmetry, i.e. that are of the form $f^{\pm}(r,\mu) = \pm f^{\pm}(r,-\mu)$. For $f^{+}(r,\mu)$, the nonvanishing coefficients in (179) become

$$f_{2k}^{\dagger} = \sum_{i=1}^{n} \frac{1}{2}(4k+1) w_i (1-\mu_i^2)^{-|m|/2} P_{2k}(\mu_i) f^{+}(r,\mu_i), \tag{181}$$

while for $f^{-}(r,\mu)$, (179) yields

$$f_{2k+1}^{\dagger} = \sum_{i=1}^{n} \frac{1}{2}(4k+3) w_i (1-\mu_i^2)^{-|m|/2} P_{2k+1}(\mu_i) f^{-}(r,\mu_i). \tag{182}$$

Differentiating (178) with respect to μ one obtains

$$\begin{aligned} \frac{\partial}{\partial\mu} f^{+}(r,\mu_i) &= -\frac{|m|\mu_i}{(1-\mu_i^2)} f^{+}(r,\mu_i) \\ &\quad + (1-\mu_i^2)^{|m|/2} \sum_{k=0}^{\infty} f_{2k}^{\dagger}(r) \frac{\partial}{\partial\mu} P_{2k}(\mu), \end{aligned} \tag{183}$$

and substituting (181) into (183) yields

$$\frac{\partial}{\partial\mu} f^{+}(r,\mu_i) = \sum_{j=1}^{n} D_{ij}^{+} f^{+}(r,\mu_j), \tag{184}$$

where

$$\begin{aligned} D_{ij}^{+} &= -\frac{|m|\mu_i}{(1-\mu_i^2)} \delta_{ij} + (1-\mu_i^2)^{|m|/2} \\ &\quad \sum_{k=0}^{n-1} \frac{1}{2}(4k+1) w_j (1-\mu_j^2)^{-|m|/2} P_{2k}(\mu_j) \frac{\partial}{\partial\mu} P_{2k}(\mu_i), \end{aligned} \tag{185}$$

and δ_{ij} is the Kronecker delta. Next, we use the recurrence relation

$$\frac{\partial}{\partial\mu} P_{2k}(\mu_i) = \frac{2k}{(1-\mu_i^2)} \Big[-\mu_i P_{2k}(\mu_i) + P_{2k-1}(\mu_i) \Big], \tag{186}$$

in (185) and define

$$S_{ij}^{+} = \sum_{k=1}^{n-1} k(4k+1) P_{2k}(\mu_j) \Big[-\mu_i P_{2k}(\mu_i) + P_{2k-1}(\mu_i) \Big]. \tag{187}$$

In (185) we truncated the expansion to include Legendre polynomials up to order $P_{2n-2}(\mu)$. If we repeat this for $f^{-}(r,\mu)$ and define

$$S_{ij}^{-} = \sum_{k=0}^{n-2} \frac{(2k+1)}{2}(4k+3)P_{2k+1}(\mu_j)\Big[-\mu_i P_{2k+1}(\mu_i) + P_{2k}(\mu_i)\Big], \tag{188}$$

then $D_{ij}^{\pm}$ is given by

$$D_{ij}^{\pm} = \frac{1}{(1-\mu_i^2)}\left\{-|m|\mu_i\delta_{ij} + \left[\frac{1-\mu_i^2}{1-\mu_j^2}\right]^{|m|/2} w_j S_{ij}^{\pm}\right\}, \tag{189}$$

and the first-order angular derivative formula becomes

$$\frac{\partial}{\partial\mu} f^{\pm}(r,\mu_i) = \sum_{j=1}^{n} D_{ij}^{\pm} f^{\pm}(r,\mu_j). \tag{190}$$

In order to obtain the second-order angular derivatives, we differentiate (184) with respect to μ

$$\begin{aligned} \frac{\partial^2}{\partial\mu^2} f^{+}(r,\mu_i) &= -\left[\frac{|m|(1+\mu_i^2)+m^2\mu_i^2}{(1-\mu_i^2)^2}\right] f^{+}(r,\mu_i) - \frac{2|m|\mu_i}{1-\mu_i^2}\frac{\partial}{\partial\mu} f^{+}(r,\mu_i) \\ &+ (1-\mu_i)^{|m|/2}\sum_{k=0}^{\infty} f_{2k}^{\dagger}(r)\frac{\partial^2}{\partial\mu^2}P_{2k}(\mu_i). \end{aligned} \tag{191}$$

Differentiating the recurrence relation (186) with respect to μ we obtain

$$\begin{aligned} \frac{\partial^2}{\partial\mu^2} P_{2k}(\mu_i) = \frac{2k}{(1-\mu_i^2)^2} \Big\{ & -\Big[1+(1-2k)\mu_i^2\Big] P_{2k}(\mu_i) \\ & + (3-4k)\mu_i P_{2k-1}(\mu_i) + (2k-1)P_{2k-2}(\mu_i) \Big\}. \end{aligned} \tag{192}$$

Continuing in the same fashion as for the first-order derivatives, we define

$$\begin{aligned} H_{ij}^{\pm} = \frac{1}{(1-\mu_i^2)^2} \Big\{ & -\Big[1+(1+|m|)\mu_i^2\Big]|m|\delta_{ij} \\ & -2|m|\mu_i(1-\mu_i^2)D_{ij}^{\pm} + \left[\frac{1-\mu_i^2}{1-\mu_j^2}\right]^{|m|/2} w_j G_{ij}^{\pm} \Big\}, \end{aligned} \tag{193}$$

where

$$G_{ij}^{+} = \sum_{k=1}^{n-1} k(4k+1)P_{2k}(\mu_j) \quad \Big\{ \quad -\Big[1+(1-2k)\mu_i^2\Big]P_{2k}(\mu_i) \\ + (3-4k)\mu_i P_{2k-1}(\mu_i) + (2k-1)P_{2k-2}(\mu_i) \;\Big\}, \tag{194}$$

and

$$G_{ij}^{-} = \sum_{k=0}^{n-2} \frac{(2k+1)}{2}(4k+3)P_{2k+1}(\mu_j) \quad \Big\{ \quad -\Big(1-2k\mu_i^2\Big)P_{2k+1}(\mu_i) \\ + (1-4k)\mu_i P_{2k}(\mu_i) + 2kP_{2k-1} \;\Big\}. \tag{195}$$

Then, the second-order angular derivatives for the functions $f^{\pm}(r,\mu)$ are

$$\frac{\partial^2}{\partial \mu^2} f^{\pm}(r,\mu_i) = \sum_{j=1}^{n} H_{ij}^{\pm} f^{\pm}(r,\mu_j). \tag{196}$$

Appendix D

Perturbed Energy Conservation Equation

In this Appendix, we construct a variational principle for the perturbed energy conservation equation (based on Friedman & Ipser [19]) and show its relation to the method presented in section 3.8. In addition, we derive an explicit expression for the inner product $< \delta U_j | L | \delta U_i >$ defined in section 3.8.

D.1 A Variational Principle

In the Lagrangian formalism, perturbations are described by the Lagrangian displacement vector ξ^a. The complete description of a perturbation requires the solution of the perturbed field, Euler and energy conservation equations for the metric perturbation h_{ab} and the displacement vector ξ^a. If one can solve all but one of the above equations, using for example a trial vector ξ^a, then the remaining equation will not be satisfied. One then has to construct a criterion, which will be used to identify the equilibrium star for which the remaining equation is satisfied.

For perturbations (ξ^a, h_{ab}) that satisfy the perturbed energy conservation equation

$$\delta\Big(u_b \nabla_a T^{ab}\Big) = 0, \tag{197}$$

the perturbed field equations form a symmetric system (Friedman & Schutz [44]). That is, two pairs (ξ^a, h_{ab}) and $(\hat{\xi}^a, \hat{h}_{ab})$ satisfying (197) obey the symmetry relation

$$\hat{\xi}_b\ \delta\Big(\nabla_c T^{bc}\Big) + \frac{1}{16\pi}\hat{h}_{bc}\ \delta\Big(G^{bc} - 8\pi T^{bc}\Big) = -\mathcal{L}\Big(\hat{\xi}^a, \hat{h}_{ab}; \xi^a, h_{ab}\Big) + \nabla_b \tilde{R}^b, \tag{198}$$

where $G^{ab} = R^{ab} - \frac{1}{2}g^{ab}R_c{}^c$ and $\nabla_b \tilde{R}^b$ is a divergence constructed from ξ^a, $\hat{\xi}^a$, h_{ab} and $\hat{h}_{ab}$. In (198), $\mathcal{L}\Big(\hat{\xi}^a, \hat{h}_{ab}; \xi^a, h_{ab}\Big)$ is a function symmetric under the interchange of the trial solutions (ξ^a, h_{ab}) and $(\hat{\xi}^a, \hat{h}_{ab})$; hence the r.h.s. in (198) is symmetric up to a divergence.

In the Eulerian approach to solving the perturbation equations, the perturbed Euler equation

$$\delta\Big(q^a{}_b \nabla_a T^{bc}\Big) = 0, \tag{199}$$

is solved analytically and six components of the perturbed field equation are solved for h_{ab} given a trial function δU. The symmetry in (198) can be exploited in order to construct a variational principle for the remaining unsolved equations. The solved perturbed Euler equation can be eliminated from (198) by decomposing the Lagrangian displacement vector ξ^a into vectors normal and parallel to the 4-velocity

$$\xi^a = \xi^a_\perp - (\xi_c u^c) u^a, \tag{200}$$

where $\xi^a_\perp = q^a{}_b \xi^b$. Equation (199) then implies

$$\hat{\xi}_b\ \delta\Big(\nabla_a T^{ab}\Big) = -(\xi_c u^c)\ \delta\Big(u_b \nabla_a T^{ab}\Big). \tag{201}$$

For trial solutions the perturbed energy conservation equation is not satisfied

$$\delta\Big(u_b \nabla_a T^{ab}\Big) \equiv L(\delta U) \neq 0, \tag{202}$$

where L is a linear operator acting on the function δU.

The Lagrangian displacement ξ^a has a gauge freedom in its component along u^a: Adding a vector field $f u^a$ (where f is some arbitrary scalar function) to ξ^a leaves the Eulerian perturbations unchanged. As was shown by Friedman & Ipser [19], if (197) is not satisfied, the perturbation equations can still be cast in a symmetric form as in (198) (but with a redefined divergence term $\nabla_b \tilde{R}^b$) if the component of ξ^a along u^a is chosen as

$$\xi_a u^a = (u\nabla)^{-1}\delta U$$
$$= \frac{1}{i\sigma\gamma}\delta U. \qquad (203)$$

With this definition,

$$\hat{\xi}_b\ \delta\Big(\nabla_a T^{ab}\Big) = \frac{i\delta\hat{U}}{\sigma\gamma}L(\delta U). \qquad (204)$$

Next, we define

$$\mathcal{F}(\delta\hat{U};\delta U) \equiv \frac{1}{16\pi}\hat{h}_{bc}\ \delta\Big(G^{bc} - 8\pi T^{bc}\Big)$$
$$= \frac{1}{16\pi}(\hat{h}^{bc} - \frac{1}{2}g^{bc}\hat{h}_d{}^d)\ \delta\Big[R_{bc} - 8\pi(T_{bc} - \frac{1}{2}g_{bc}T_d{}^d)\Big], \qquad (205)$$

which is implicitly bilinear in $\delta\hat{U}$ and δU. The gauge freedom in h_{ab} leaves only six (out of ten) components of the perturbed field equations independent. Thus, if a trial solution satisfies six components of the perturbed field equations in (205), the other four components of the perturbed field equations will be an implicit functional of the perturbed energy conservation equation, the only remaining equation that needs to be satisfied. Schematically, one can write

$$\mathcal{F}(\delta\hat{U};\delta U) \equiv \delta\hat{U}\mathbf{F}\Big[L(\delta U)\Big], \qquad (206)$$

where $\mathbf{F}$ is a functional of $L(\delta U)$. We have used the linearity of $\mathcal{F}(\delta\hat{U};\delta U)$ to factor out $\delta\hat{U}$. The symmetry relation (198) becomes

$$-\mathcal{L}\Big(\hat{\xi}^a,\hat{h}_{ab};\xi^a,h_{ab}\Big) = \frac{i\delta\hat{U}}{\sigma\gamma}L(\delta U) + \delta\hat{U}\mathbf{F}\Big[L(\delta U)\Big] - \nabla_b\tilde{R}^b$$
$$= \delta\hat{U}\Big[\frac{i}{\sigma\gamma} + \mathbf{F}\Big]L(\delta U) - \nabla_b\tilde{R}^b$$
$$\equiv -\mathcal{L}(\delta\hat{U};\delta U) \qquad (207)$$

A variational principle for the perturbed energy conservation equation is constructed, by requiring that the following integral (which is implicitly quadratic in δU) vanishes

$$I = \int -\mathcal{L}(\delta U; \delta U)\sqrt{-g}d^3x = 0. \tag{208}$$

Because the integral of the divergence vanishes, this yields

$$I = \int \delta U\left[\frac{i}{\sigma\gamma} + \mathbf{F}\right]L(\delta U)\sqrt{-g}d^3x = 0. \tag{209}$$

The integral in (209) is stationary with respect to first order variations in δU

$$\frac{\delta I}{\delta(\delta U)} = 0, \tag{210}$$

$$\Longrightarrow \qquad \left[\frac{i}{\sigma\gamma} + \mathbf{F}\right]L(\delta U) = 0, \tag{211}$$

$$\Longrightarrow \qquad L(\delta U) = 0, \tag{212}$$

provided that $\frac{i}{\sigma\gamma}L(\delta U) \neq -\mathbf{F}\Big[L(\delta U)\Big]$. Thus, $I = 0$ is a variational principle for the perturbed energy conservation equation $L(\delta U) = 0$.

In practice, one can expand the trial function δU in terms of a set of basis functions δU_i

$$\delta U = \sum_i a_i \delta U_i. \tag{213}$$

Substituting (213) into (209) yields

$$\begin{aligned} &\sum_i \sum_j a_i a_j \int \delta U_j \Big[\frac{i}{\sigma\gamma} + \mathbf{F}\Big] L(\delta U_i)\sqrt{-g}d^3x = 0 \\ \Longrightarrow \qquad &\sum_i \sum_j a_i a_j A_{(ij)} = 0, \end{aligned} \tag{214}$$

where we defined the symmetric matrix A with elements

$$A_{ij} = \int \delta U_j \Big[\frac{i}{\sigma\gamma} + \mathbf{F}\Big] L(\delta U_i)\sqrt{-g}d^3x. \tag{215}$$

Equation (210) implies that the integral I will be stationary to the variation of any of the coefficients a_i in the expansion (213). Thus,

$$\frac{\delta I}{\delta a_i} = 0 \quad \Longrightarrow \quad \sum_i a_j A_{(ij)} = 0. \tag{216}$$

The last equation is a homogeneous linear system for the coefficients a_j which has a nontrivial solution only when

$$\det A_{(ij)} = 0. \tag{217}$$

Since we can find an explicit form for A_{ij} in terms of known quantities, we could have used (217) as a criterion for locating neutral modes. However, the term $\mathbf{F}[L(\delta U_i)]$ involves many second order angular and radial derivatives and it is not certain how accurate its evaluation on our finite grid would be. Since the method described in section 3.8 gives a substantially simpler criterion which does not involve $\mathbf{F}[L(\delta U_i)]$, we chose to use that for locating the neutral modes. It is interesting to note that the matrix elements

$$< \delta U_j | L | \delta U_i >= \int \frac{i\delta U_j}{\sigma\gamma} L(\delta U_i)\sqrt{-g}d^3x \tag{218}$$

used in section 3.8 are *nearly* symmetric under the interchange of δU_i and δU_j, for all configurations considered. This indicates that the method described in section 3.8 nearly coincides with a variational principle.

D.2 An Expression for the Inner Product

Since for the equilibrium star $u_b \nabla_a T^{ab} = 0$,

$$\begin{aligned} L(\delta U) &= \delta\Big(u_b \nabla_a T^{ab}\Big) \\ &= \Delta\Big(u_b \nabla_a T^{ab}\Big) \\ &= -\Delta\Big[(\epsilon + P)\nabla_b u^b + u^b \nabla_b \epsilon\Big] \\ &= -u^c \nabla_c \Big[\Delta\epsilon + \frac{1}{2}(\epsilon + P) q^{ab} \Delta g_{ab}\Big] \\ &= -i\sigma\gamma\Big[\Delta\epsilon + \frac{1}{2}(\epsilon + P) q^{ab}\Delta g_{ab}\Big], \end{aligned} \tag{219}$$

(cf. Friedman & Ipser, 1992). Then,

$$L(\delta U) = -i\sigma\gamma\Big\{\delta\epsilon + \xi^a_\perp \nabla_a \epsilon + \frac{1}{2}(\epsilon + P)\Big[h_c{}^c + u^a u^b h_{ab} + 2\nabla_a \xi^a + 2u^a u^b \nabla_a \xi_b\Big]\Big\}, \tag{220}$$

where we used $\Delta g_{ab} = h_{ab} + \nabla_a \xi_b + \nabla_b \xi_a$. Using the decomposition (200) of ξ^a, one obtains

$$\nabla_a \xi^a = \nabla_a \xi^a_\perp - \delta U, \tag{221}$$

and

$$u^a u^b \nabla_a \xi_b = \delta U - \xi^b_\perp u^a \nabla_a u_b. \tag{222}$$

The Euler equations for the equilibrium configuration yield

$$u^b \nabla_b u_c = -\frac{q_c{}^b \nabla_b P}{\epsilon + P}. \tag{223}$$

Then (219) becomes

$$L(\delta U) = -i\sigma\gamma\Big\{\delta\epsilon + \xi^a_\perp \nabla_a(\epsilon + P) + \frac{1}{2}(\epsilon + P)\Big[h_c{}^c + u^a u^b h_{ab} + 2\nabla_a \xi^a_\perp\Big]\Big\}. \tag{224}$$

The perturbed energy density is

$$\delta\epsilon = \frac{(\epsilon + P)^2}{P\Gamma}\Big(\delta U + \frac{1}{2}u^a u^b h_{ab}\Big), \tag{225}$$

so that

$$L(\delta U) = -i\sigma\gamma\Big\{(\epsilon + P)\Big[\frac{(\epsilon + P)}{P\Gamma}\delta U + \frac{1}{2}\Big(1 + \frac{\epsilon + P}{P\Gamma}\Big)u^a u^b h_{ab} + \frac{h_c{}^c}{2}\Big] + \nabla_a\Big[\xi^a_\perp(\epsilon + P)\Big]\Big\}. \tag{226}$$

The matrix elements defined in section 3.8 now take the form

$$\begin{aligned} < \delta U_j | L | \delta U_i > &= \int \frac{i\delta U_j}{\sigma\gamma} L(\delta U_i)\sqrt{-g}d^3x \\ &= \int (\epsilon + P)\Big\{\delta U_j\Big[\frac{(\epsilon + P)}{P\Gamma}\delta U_i + \frac{1}{2}\Big(1 + \frac{\epsilon + P}{P\Gamma}\Big)u^a u^b h_{ab} + \frac{h_c{}^c}{2}\Big] \\ &\qquad - \xi^a_\perp \nabla_a \delta U_j\Big\}\sqrt{-g}d^3x, \end{aligned} \tag{227}$$

where we have used the time-independence of ξ^a to eliminate the term $\int \nabla_a[\xi^a_\perp(\epsilon + P)\delta U]\sqrt{-g}d^3x$ as an integral of a spatial divergence.

Finally, the component of ξ^a normal to the 4-velocity u^a is related to the component of δu^a normal to u^a by

$$\xi^a_\perp = \frac{\delta u^a_\perp}{i\sigma\gamma} = \frac{\delta u^a - \frac{1}{2}u^b u^c h_{bc} u^a}{i\sigma\gamma}, \tag{228}$$

(cf. Ipser & Lindblom [63]) and the expression for $< \delta U_j|L|\delta U_i >$ used in our numerical computations becomes

$$\begin{aligned} < \delta U_j|L|\delta U_i > \;=\; & \int (\epsilon + P)\Bigg\{\delta U_j \left[\frac{(\epsilon+P)}{P\Gamma}\delta U_i + \frac{1}{2}\left(1 + \frac{\epsilon+P}{P\Gamma}\right)u^a u^b h_{ab} + \frac{h_c{}^c}{2}\right] \\ & - \frac{(\delta u^a - \frac{1}{2}u^b u^c h_{bc} u^a)}{i\sigma\gamma}\nabla_a \delta U_j\Bigg\}\sqrt{-g}\,d^3x, \end{aligned} \tag{229}$$

where h_{ab} and δu^a are computed with δU_i.

Bibliography

[1] Friedman, J. L., in *Proceedings of the 1994 Aspen Conference on Millisecond Pulsars*, edited by A. S. Fruchter *et al.* (Astronomical Society of the Pacific Conference Series vol. 72, 1995), p. 177

[2] Butterworth, E. M., & Ipser, J. R. 1976, Astrophysical J., 204, 200

[3] Friedman, J. L., Ipser, J. R., & Parker, L. 1986, Astrophysical J., **304**, 115, Erratum, Astrophysical J., **351**, 705

[4] Friedman, J. L., Ipser, J. R., & Parker, L. 1989, Phys. Rev Lett., **62**, 3015

[5] Lattimer, L. M., Prakash M., Masak D., & Yahil A., 1990, Astrophysical J., **355**, 241

[6] Komatsu, H., Eriguchi, Y., & Hachisu, 1989, MNRAS, **237**, 355

[7] Komatsu, H., Eriguchi, Y., & Hachisu, 1989, MNRAS, **239**, 153

[8] Cook, G. B., Shapiro, S. L., & Teukolsky, S. A. 1992, Astrophysical J., **398**, 203

[9] Cook, G. B., Shapiro, S. L., & Teukolsky, S. A. 1994, Astrophysical J., **422**, 227

[10] Cook, G. B., Shapiro, S. L., & Teukolsky, S. A. 1994, Astrophysical J., **424**, 823

[11] Eriguchi, Y., Hachisu & Nomoto, K. 1994, MNRAS, **266**, 179

[12] Nishida, S., Eriguchi, Y., & Lanza, A. 1992, Astrophysical J., **401**, 618

[13] Nishida, S., Eriguchi, Y. 1994, Astrophysical J., **427**, 429

[14] Hashimoto, M., Oyamatsu, K., & Eriguchi, Y. 1994, Astrophysical J. **436**, 257

[15] Neugebauer, G., & Herlt, E. 1984, Class. Quant. Grav., **1**, 695

[16] Wu, X., Müther, H., Soffel, M., Herold, H., & Ruder, H. 1991, Astron. & Astrophys., **246**, 411

[17] Neugebauer, G., & Herold, H. 1992, in *Proc. of the Bad Honnef Meeting on Relativity and Gravitational Physics*, ed. Schäfer (Berlin:Springer)

[18] Salgado, M., Bonazzola, S., Gourgoulhon, E. & Haensel, P. 1994, Astron. & Astrophys. Suppl., **108**, 455

[19] Friedman, J. L., & Ipser, J. R. 1992, Phil. Trans. R. Soc. Lond., **A340**, 391

[20] Bardeen, J. M., & Wagoner, R. V. 1971, Astrophysical J., **167**, 359

[21] Nakamura, S., *Applied Numerical Methods in C* (Englewood Cliffs,Prentice Hall,1993)

[22] Eriguchi, Y., personal communication

[23] Y. Eriguchi, J. L. Friedman, E. Gourgoulhon, T. Nozawa, N. Stergioulas, (names in temporary order, in preparation).

[24] Arnett, W. D., & Bowers, R. L. 1977, Astrophysical J.. Sup., **33**, 415

[25] Salgado, M., Bonazzola, S., Gourgoulhon, E. & Haensel, P. 1994, Astron. & Astrophys. **291**, 155

[26] Friedman, B., & Pandharipande, V. R. 1981, Nucl. Phys., **A361**, 502

[27] Friedman, J. L., Ipser, J. R., & Sorkin, R. D. 1988, Astrophysical J., **325**, 722

[28] Glendenning, N. K. 1992, Phys. Rev. D **46**, 4161

[29] Taylor, J. H. & Weisberg, J. M. 1989, Astrophys. J. **345**, 434

[30] Hartle, J. B. & Sabbadini, A. G. 1977, Astrophys. J. **213**, 831

[31] Rhoades Jr., C. E. & Ruffini, R. 1974, Phys. Rev. Lett. **32**, 324

[32] Friedman, J. L. & Ipser, J. R. 1987 Astrophys. J. **314**, 594

[33] Pandharipande, V. R. & Ravenhall, D. G., in *Proceedings of the NATO Advanced Research Workshop on Nuclear Matter and Heavy Ion Collisions, Les Houches, 1989*, edited by M. Soyeur *et al.* (plenum, New York, 1989), p.103.

[34] Geroch R. & Lindblom L. 1991, Ann. Phys., **207**, 394

[35] Ravenhall, D. G., 1995, personal communication

[36] Stergioulas, N. & Friedman, J. L. 1995, Astrophys. J. **444**, 306

[37] Haensel, P. & Zdunik, J. L. 1989, Nature **340**, 617

[38] Press, W. H. *et al*, *Numerical Recipes in C*, 2nd edition (University of Cambridge, Cambridge, 1992).

[39] Baym, G., Pethick, C. & Sutherland, P. 1971, Astrophys. J. **170**, 229

[40] Hartle, J. B. 1978, Phys. Repts, **46**, 201

[41] Arnett, W. D. & Bowers, R. L. 1977, Astrophys. J. Suppl. **33**, 415

[42] Chandrasekhar, S. 1970, Phys. Rev. Lett., **24**, 611

[43] Friedman, J. L. & Schutz, B. F. 1975, Astrophysical J. Lett., **199**, L157

[44] Friedman, J. L. & Schutz, B. F. 1995, Astrophysical J., **200**, 204

[45] Friedman, J. L & Schutz, B. F. 1978, Astrophysical J., **221**, 937

[46] Friedman, J. L. & Schutz, B. F. 1978, Astrophysical J., **222**, 281

[47] Ipser, J. R. & Lindblom, L. 1991, Astrophysical J., **373**, 213

[48] Ipser, J. R. & Lindblom, L. 1991, Astrophysical J., **379**, 285

[49] Yoshida, S. & Eriguchi, Y. 1995, Astrophysical J., **438**, 830

[50] Imamura, J. N., Friedman, J. L. & Durisen, R. H. 1985, Astrophysical J., **294**, 474

[51] Managan, R. A. 1985, Astrophysical J., **294**, 463

[52] Ipser, J. R. & Lindblom, L. 1990, Astrophysical J., **355**, 226

[53] Ipser, J. R. & Managan, R. A. 1985, Astrophysical J., **292**, 517

[54] Cutler, C. 1991, Astrophysical J., **374**, 248

[55] Cutler, C. & Lindblom, L. 1992, Astrophysical J., **385**, 630

[56] Lindblom, L. 1995, Astrophysical J., **438**, 265

[57] Taub, A. H. 1967, Commun. Math. Phys., **6**, 248

[58] Chadrasekhar, S. & Lebovitz, N. 1968, Astrophysical J., **152**, 267

[59] Chadrasekhar, S. & Lebovitz, N. 1973, Astrophysical J., **185**, 19

[60] Lynden-Bell, D. & Ostriker, J. P. 1967, MNRAS, **136**, 293

[61] Bardeen, J. M., Friedman, J. L., Schutz, B. F. & Sorkin, R. 1977, Astrophysical J. Lett., **217**, L49

[62] Carter, B. 1973, Commun. Math. Phys., **30**, 261

[63] Ipser, J. R. & Lindblom, L. 1992, Astrophysical J., **389**, 392

[64] Regge, T. & Wheeler, J. A. 1957, Phys. Rev. **108**, 1063

[65] Priou, D. 1992, MNRAS, **254**, 435

[66] Gropp, W. & Smith, B., in *Proceedings of the Scalable Parallel Libraries Conference* (IEEE,1994) pg. 60

[67] Skinner, D. & Lindblom, L. 1996, preprint, Montana State University

[68] James, R.A. 1964, Astrophysical J., **140**, 552

[69] Bonazzola, S., Frieben, J. & Gourgoulhon, E. 1996, Astrophysical J., **460**, 379

[70] Abramowitz, M. & Stegun, I. A., *Handbook of Mathematical Functions*, (New York,Dover,1964)

VITA

Title of Dissertation

The Structure and Stability of Rotating Relativistic Stars

Full Name

Nikolaos Stergioulas

Place and Date of Birth

Gütersloh, Germany	March 21, 1967

Colleges and Universities,	Years attended and degrees	
Aristotle University of Thessaloniki	1986 to 1991,	B.S.
University of Wisconsin - Milwaukee	1991 to 1993,	M.S.
University of Wisconsin - Milwaukee	1993 to 1996,	Ph.D.

Publications

1. Stergioulas, N. & Friedman, J. L., *Comparing Models of Rapidly Rotating Stars Constructed by Two Numerical Methods*, 1995, Astrophysical J., **444**, 306

2. Koranda, S., Stergioulas, N. & Friedman, J. L., *The Causality-Set Upper Limit on the Rotation of Gravitationally Bound Stars*, to be submitted to Phys. Rev. D.

3. Stergioulas, N. & Friedman, J. L., *Nonaxisymmetric Neutral Modes in Rotating Relativistic Stars*, to be submitted to Astrophys. J.

Major Department

Physics

Professor John L. Friedman Date